

**Lanthanide Ions Doping Effects on Structural,
Electrophysical and Functional Properties of
Sol-gel Fabricated PbTiO₃ Thin Films**

Dissertation

Zur Erlangung des akademischen Grades
Doktor der Ingenieurwissenschaften
(Dr.-Ing.)
der Technischen Fakultät
der Christian-Albrechts-Universität zu Kiel

Sergey Yakovlev

Kiel 2004

Supervisor: Prof. Dr. F. Faupel

Co-supervisor: Prof. Dr. M. Es-Souni

Contents

	Acknowledgements	5
	Abstract	7
	Introduction	9
I	Basics of Ferroelectric Materials	12
	I.1. What is ferroelectricity?	12
	I.2. Phase transitions in ferroelectric materials	18
	I.3. Properties of some well known ferroelectric materials	20
II	Methods for ferroelectric thin films processing	22
	II.1. Electron beam evaporation	22
	II.2. Pulsed laser deposition (PLD)	22
	II.3. Multi-ion-beam reactive sputter deposition (MIBRSD)	23
	II.4. Organometallic chemical vapour deposition (OMCVD)	23
	II.5. Sol-gel processing of thin films	24
III	Applications of ferroelectric thin films	27
	III.1. Non-volatile and Dynamic Random Access Memories	27
	III.2. Microelectromechanical systems	28
	III.3. IR detectors	30
IV	Characterization of ferroelectric materials	35
	IV.1. X-ray diffractometry	35
	IV.2. Raman spectroscopy	37
	IV.3. X-ray photoelectron spectroscopy	38
	IV.4. Scanning electron microscopy	39
	IV.5. Atomic force microscopy	40
	IV.6. Ellipsometry	41
	IV.7. Ferroelectric hysteresis characterization	44
	IV.8. Dielectric properties measurements	45
	IV.9. Leakage current measurements	46
	IV.10. Determination of pyroelectric coefficient of ferroelectric materials	47
	IV.11. Measurements of piezoelectric characteristics of ferroelectric materials	48
V	Overview of the properties of lead-based perovskite-type ferroelectric thin films: microstructural and compositional aspects	51
	V.1. Optical properties	51
	V.2. Microstructure and crystallization kinetics	53
	V.3. Raman scattering	55
	V.4. Dielectric properties	57
	V.5. Ferroelectric properties	61
	V.6. Curie phase transition temperature	64
	V.7. Doping effects	66
	V.8. Leakage currents	69
	V.9. Pyroelectric and piezoelectric properties of ferroelectric thin films	73

VI	Aims of this work	75
VII	Preparation and characterization of lanthanide ions doped PbTiO₃ thin films: experimental details	77
VII.1.	Sol-gel fabrication of pure and rare-earth substituted PbTiO ₃ thin films and optimisation of deposition parameters	77
VII.2.	Experimental details on structural and electrophysical properties characterization	84
VIII	Experimental results	90
VIII.1.	Structural properties of rare-earth substituted PbTiO ₃ thin films	90
VIII.2.	Raman scattering from pure and rare-earth substituted PbTiO ₃ thin films	99
VIII.3.	Refractive indices and extinction coefficients of lanthanide ions doped lead titanate thin films	100
VIII.4.	Room temperature dielectric properties of pure and doped lead titanate thin films	103
VIII.5.	Effect of lanthanide ions doping on the ferroelectric-paraelectric phase transition temperature	104
VIII.6.	Ferroelectric properties of PbTiO ₃ thin films doped with lanthanide ions	107
VIII.7.	Thickness effects and contribution of interfacial bottom electrode-thin film layer into small signal dielectric properties of doped lead titanate thin films	108
VIII.8.	Field-dependent dielectric properties of pure and doped lead titanate thin films	109
VIII.9.	Voltage-, temperature- and thickness-dependent leakage currents in pure and doped lead titanate thin films	111
IX	Discussions	116
IX.1.	Structural properties, phase content and preferred orientation of PbTiO ₃ thin films doped with the elements of lanthanide series	116
IX.2.	Raman scattering from pure and lanthanide ions doped PbTiO ₃ thin films	121
IX.3.	Refractive indices and extinction coefficients of lanthanide ions doped lead titanate thin films	122
IX.4.	Room temperature dielectric properties of pure and doped lead titanate thin films	124
IX.5.	Effect of lanthanide ions doping on the ferroelectric-paraelectric phase transition temperature	125
IX.6.	Ferroelectric properties of PbTiO ₃ thin films doped with the elements of lanthanide series	127
IX.7.	Thickness- and field-dependent dielectric properties of pure and doped lead titanate thin films	128
IX.8.	Voltage-, temperature- and thickness-dependent leakage currents in pure and doped lead titanate thin films	131
X	Choice of application: doped PbTiO₃ thin films for pyroelectric and piezoelectric detectors	137
XI	Summary and conclusions	144
	List of references	147
	Appendix	156
	Curriculum Vitae	164

Acknowledgements

I express my deep gratitude to many people who contributed through their support, experience and friendship to this work. In particular I am in debt to

Prof. Dr. M. Es-Souni for supervision and giving me the opportunity to work at the University of Applied Sciences of Kiel, Institute for Materials and Surface Technology (IMST), his support, confidence and providing facilities for this work to be accomplished.

Prof. Dr. F. Faupel (Department of Engineering, Christian-Albrechts University, Kiel) for the warm encouragement and being co-supervisor during preparation of the thesis.

C.-H. Solterbeck (University of Applied Sciences, Institute for Materials and Surface Technology (IMST), Kiel) for the helpful discussions and the assistance in AFM, dielectric and ferroelectric measurements.

Dr. M. Kuhnke (University of Applied Sciences, Institute for Materials and Surface Technology (IMST), Kiel) for the assistance in pyroelectric and piezoelectric characterizations.

Dr. V. Zaporojtchenko and J. Žekonytė (Department of Engineering, Christian-Albrechts University, Kiel) for the help during XPS experiments.

Dr. K. Rätzke and T. Metzling (Department of Engineering, Christian-Albrechts University, Kiel) for the assistance and troubleshooting during XRD measurements.

Dr. M. Avdeev (Materials Science Division, Argonne National Laboratory) for useful discussions, and different kinds of support.

A. Piorra, E. Girdauskaitė and A. Dreher (University of Applied Sciences, Institute for Materials and Surface Technology (IMST), Kiel) for their help in specimen preparation and creating cooperative and pleasant atmosphere in the laboratories.

Prof. Dr. E. Skou, S.W. Lena (Department of Chemistry, University of Southern Denmark, Odense, Denmark), Prof. Dr. F. Tuczek, U. Cornelissen (Department of Mathematics and Natural Sciences, Christian-Albrechts University of Kiel, Kiel, Germany) for their help in Raman measurements.

Prof. Dr. A. Neiman (Department of Inorganic Chemistry, Ural State University, Ekaterinburg, Russia), Dr. V. Kharton (Department of Ceramics and Glass Engineering, University of Aveiro, Portugal) and Prof. Dr. I. Smirnov (Department of Materials Science, Moscow State Institute of Electronics and Mathematics (Technical University), Russia), for useful discussions and encouragement.

Finally I express the deep gratitude to my family and friends for the support over the years.

Abstract

Ferroelectrics belong to the special class of non-centrosymmetric polar dielectrics in which spontaneous polarization of lattice can be switched via the application of an external electric field. In particular, perovskite-type lead titanate-based ferroelectrics became the most prominent candidates for applications in different kinds of modern transducers, sensors and actuators. Particular interest in these materials is driven by their unique dielectric, ferroelectric, pyroelectric and piezoelectric characteristics. The application of these materials in *thin film form* is even more attractive since it allows direct integration into existent semiconductor technology. The properties of lead-titanate based ferroelectrics are known to strongly depend on the stoichiometry and nature of substituent elements either on Pb (A) or Ti (B) sites. In this respect appropriate doping by different elements offers the possibility to tune materials functional properties.

Lanthanides (rare-earths) constitute a series of chemically similar elements with gradually decreasing ionic radius. Therefore, systematic investigations of lanthanide ions doped ferroelectrics can reveal the effect of the ionic radius of substituent on the structural and electrophysical properties of the host material. To our knowledge, these investigations are still lacking. Moreover, interrelation between doping level and performance of the materials must be established.

In the present work, a modified sol-gel method was adopted to fabricate lead titanate thin films doped with Ce, Sm, Dy, Er and Yb. Two different substrate heterostructures including Si/SiO₂/Ti/(111)-textured Pt and Si/SiO₂/Ti/(111)-Pt/LNO (polycrystalline lanthanum nickel oxide LaNiO₃) were used. The structural properties, phase composition and preferentially oriented state of the films were analyzed by means of X-ray diffractometry (XRD), including pole figure and fibre texture (FT) analyses, Raman spectroscopy, scanning electron microscopy (SEM) and atomic force microscopy (AFM). The optical, dielectric, ferroelectric and leakage current properties were investigated in order to reveal the effects of nature and concentration of doping ions, substrate heterostructure and film thickness on the main characteristics of the films.

Fine grained (grain size was found to be in the range of 100-140 nm) homogeneous microstructures were obtained under the conditions optimised in this work. The formation of the perovskite phase was confirmed by means of X-ray diffractometry and Raman spectroscopy. The softening of the $E(1TO)$ soft mode was found for pure and doped films. Doping with rare-earth ions caused further decrease of the soft phonon frequency indicating decrease of the ferroelectric order in the films. The results are discussed in terms of combined effects of stress state, grain size and doping. Additionally, XRD characterization revealed decrease of the lattice tetragonality for all doping ions investigated.

Pole figure and fibre texture plot analyses of the films deposited on (111) textured Pt bottom electrode showed the effect of lanthanide ions doping on preferred orientation of the films. (100) out-of-plane texture was revealed for pure and Dy and Er substituted films. Ce, Sm and Yb substituted films were found to be characterized by (100)+(111) preferred orientations with no in-plane alignment.

It is demonstrated that the electrophysical properties of the films can be effectively tuned via doping by rare-earth ions. An interrelation between the atomic number/ionic radius of lanthanides and the low and high (optical) frequency dielectric properties is shown and discussed in terms of polarizability of the ions involved. Analysis of the leakage current data obtained at various temperatures for the films deposited on metal and oxide electrodes revealed specific conduction properties depending on electrode type and temperature range. The conduction mechanisms have been found to be complex involving interface- and bulk-limited or both. The results are compared to the data obtained for undoped films and also to the data reported by other research groups for bulk ferroelectric materials and thin films. Finally, the pyroelectric and piezoelectric characteristics of selected thin film specimens were investigated in order to explore their applicability in pyroelectric and piezoelectric sensors. It is shown that the functional properties (in particular, effective pyroelectric and piezoelectric coefficients) of the investigated ferroelectric thin films depend on the nature of dopant. The possibility to tailor the pyroelectric and piezoelectric coefficients of the films via the appropriate doping is demonstrated.

Introduction

More than 80 years since *ferroelectricity* was discovered by J. Valasek in 1920 [1] this phenomenon has been drawing an ever increasing attention of scientists and technologists. Unique properties of ferroelectric materials made them attractive for fundamental research as well as for military and civil applications. Since then intensive investigations that were undertaken by many research institutions resulted in the development of new classes of devices, and the technology is well established at present. A detailed history of ferroelectricity can be found elsewhere [2-6]. Table 1 shows in a brief form the main events in the history of ferroelectricity [6]. Ferroelectricity has been found to be inherent to a vast group of organic and inorganic materials and a number of phenomenological approaches have been proposed for ferroelectric phenomena explanation. At the earliest stages bulk materials such as single crystals and ceramics were the only objects available for investigations. At the same time, the compelling drive to miniaturization of up-to-date electronic devices made urgent the integration of ferroelectric materials into existent silicon technology, mainly in the form of thin films. Significant progresses in thin films deposition technology that were made at the end of the 70's stirred up new scientific interest in the area. Nowadays ferroelectric thin films are being successfully used in discrete electronic devices as well as components of integrated circuits. Microelectromechanical systems (MEMS), pyroelectric infrared (IR) sensors, non-volatile and dynamic random access memory devices (DRAMs) are among them. Moreover the present-day technology has allowed the fabrication of different kinds of heterostructures with unique characteristics which could not be attained before in homogeneous materials.

In comparison to ceramics or single crystals, thin film properties are affected by additional factors: the choice of substrate material chiefly affects microstructure development through substrate texture, and stress state of the film through thermal expansion mismatch. Furthermore, the required thickness of the films usually lies in the sub-micron region; hence the contribution of transitional film-electrode layers can not be neglected. In addition, the properties of thin films are strongly affected by deposition conditions and different kinds of impurities. In terms of ferroelectric properties there is no significant difference between bulk

Notable events in the history of ferroelectric materials (after Haertling [6]).

Timeline	Event
1820	Pyroelectricity discovered in Rochelle salt
1880	Piezoelectricity discovered in Rochelle salt, quartz, and other materials
1912	Ferroelectricity discovered in Rochelle salt
1935	Ferroelectricity discovered in KH_2PO_4
1941	BaTiO_3 high-k (>1200) capacitor developed
1944	Ferroelectricity discovered in ABO_3 -type perovskite BaTiO_3
1945	BaTiO_3 reported as useful piezotransducer, Pat. No. 2486560
1949	Phenomenological theory of BaTiO_3 introduced
1949	LiNbO_3 and LiTaO_3 reported as FE
1951	Concept of ferroelectricity introduced
1952	PZT reported as FE solid-solution system, phase diagram established.
1953	PbNb_2O_6 reported as FE
1954	PZT reported as useful piezotransducer, Pat. No. 2708244
1955	PTC effect in BaTiO_3 reported
1955	Chemical coprecipitation of FE materials
1955	Alkali niobates reported as FE
1957	BaTiO_3 barrier layer capacitors developed
1959	PZT and 5H MPB-type piezo compositions, Pat. No. 2911370
1961	Lattice dynamics theory for FE materials, soft modes introduced
1961	PMN relaxor materials reported
1964	Oxygen/atmosphere sintering for FEs developed
1964	FE semiconductor (PTC) devices developed.
1967	Optical and E/O properties of hot-pressed FE ceramics reported
1969	Terms “ferroic” and “ferroelasticity” introduced
1969	Optical transparency achieved in hot-pressed PLZT ceramics
1970	PLZT compositional phase diagram established, Pat. No. 3666666
1971	Useful E/O properties reported for PLZT, Pat. No. 3737211
1973	Oxygen/atmosphere sintering of PLZT to full transparency
1977	FE thin films developed
1978	Engineering (connectivity designed) FE composites developed
1980	Electrostrictive relaxor PMN devices developed, Pat. No. 5345139
1981	Sol-gel techniques developed for the preparation of FE films
1983	Photostrictive effects reported in PZT and PLZT
1991	Moonie piezoflexional devices developed, Pat. No. 4999819
1992	RAINBOW piezobending actuators developed, Pat. No. 5471721
1993	Integration of FE films to silicon technology, Pat. No. 5038323
1997	Relaxor single-crystal materials developed for piezotransducers

and thin films. However the latter, because it is clamped on a substrate, is the subject of specific influences (for instance, ferroelectric thin films are usually characterized by higher values of coercive field, and lower remnant polarization and pyroelectric coefficient). All these factors make the study of ferroelectric films far more complicated than their ceramic counterparts.

The present work attempts to contribute to the understanding of film formation, film properties and potential applications of lead containing perovskite type ferroelectric materials.

The sol-gel method was adapted and modified for the purpose to fabricate high quality perovskite-type films of sub-micron thickness. Elements of the lanthanide series were used as dopants to modify the electrophysical properties of lead titanate thin films. A systematic investigation of the effects of lanthanide elements doping on microstructure and properties of lead titanate thin films which is still lacking, is undertaken in this work. The films were investigated by means of scanning probe microscopy, scanning electron microscopy, X-ray diffractometry, Raman spectroscopy and X-ray photoelectron spectroscopy. The optical, dielectric, ferroelectric and leakage current properties of the films were characterized, and are discussed with respects to microstructures obtained. Additionally, effects of film thickness and the nature of bottom electrode were investigated. Finally, the potentials of these films for IR and piezoelectric sensor applications have been explored.

I. Basics of ferroelectric materials

I.1. What is ferroelectricity?

There is a vast group of materials that possess spontaneous polarization in absence of an external electric field. This polarization arises from the center of positive charges being not coincident with that of negative charges [7,8]. Adjacent unit cells are inclined to polarize in the same direction. The areas with equally directed vectors of polarization have typical size of nano- or microregions and are called ferroelectric domains. Nowadays the presence of spontaneous polarization is recognised in a wide group of non-centro-symmetrical lattice materials, although the most studied materials belong to so-called oxygen-octahedral class of dielectrics [9]. To this class one can refer dielectrics with perovskite structure having generalized formula ABO_3 . Fig I.1.1 shows the perovskite structure. A is usually a large positive ion situated at the corner of the lattice. B is small positive ion located at the body center. The oxygen ions are situated at the face centre. A is a divalent and B a tetravalent metal. Among the most important materials from the point of view of applications are

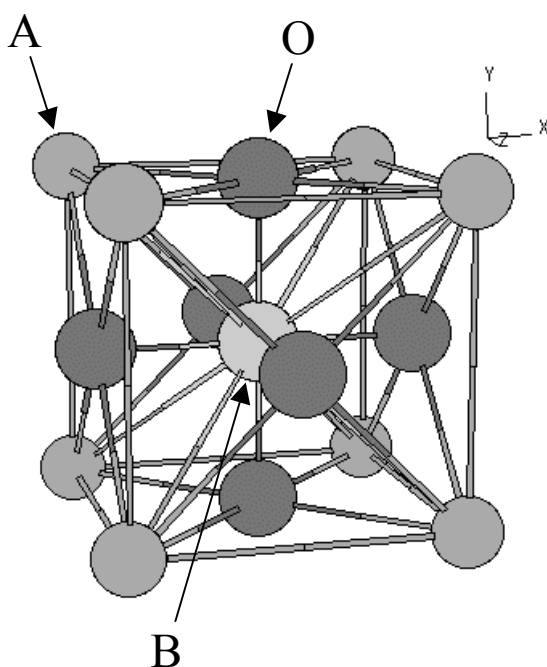


FIG.I.1.1. Lattice with perovskite structure having formula ABO_3 . A atom, B atom, and oxygen occupy the corner site, body-centered site, and face-centered site, respectively.

barium titanate (BaTiO_3), lead zirconate (PbZrO_3), lead titanate (PbTiO_3) and solid solutions of lead zirconate titanates $\text{Pb}(\text{Zr,Ti})\text{O}_3$ (PZT).

From the geometry of the structure it follows that for the “ideal” structure there is the following relationship between the radii R_A , R_B and R_O of the A, B and O^{2-} ions [9]:

$$R_A + R_O = \sqrt{2}(R_B + R_O) \quad (\text{I.1.1})$$

Actually the cubic perovskite structure or slightly deformed variants of it are found for ions which do not obey this relation exactly, and this was expressed by introducing a “tolerance factor” [9]:

$$R_A + R_O = t\sqrt{2}(R_B + R_O) \quad (\text{I.1.2})$$

Provided that the ionic sizes are right, the only other condition to be fulfilled is that the structure is electrically neutral, that is, that the sum of the charges on A and B is 6.

It then appeared that for all the compounds with the perovskite-type structure the value of t lies between approximately 0.8 and 1 – for lower values of t the ilmenite structure is found – and that for the ideal cubic structure, t must be greater than 0.89.

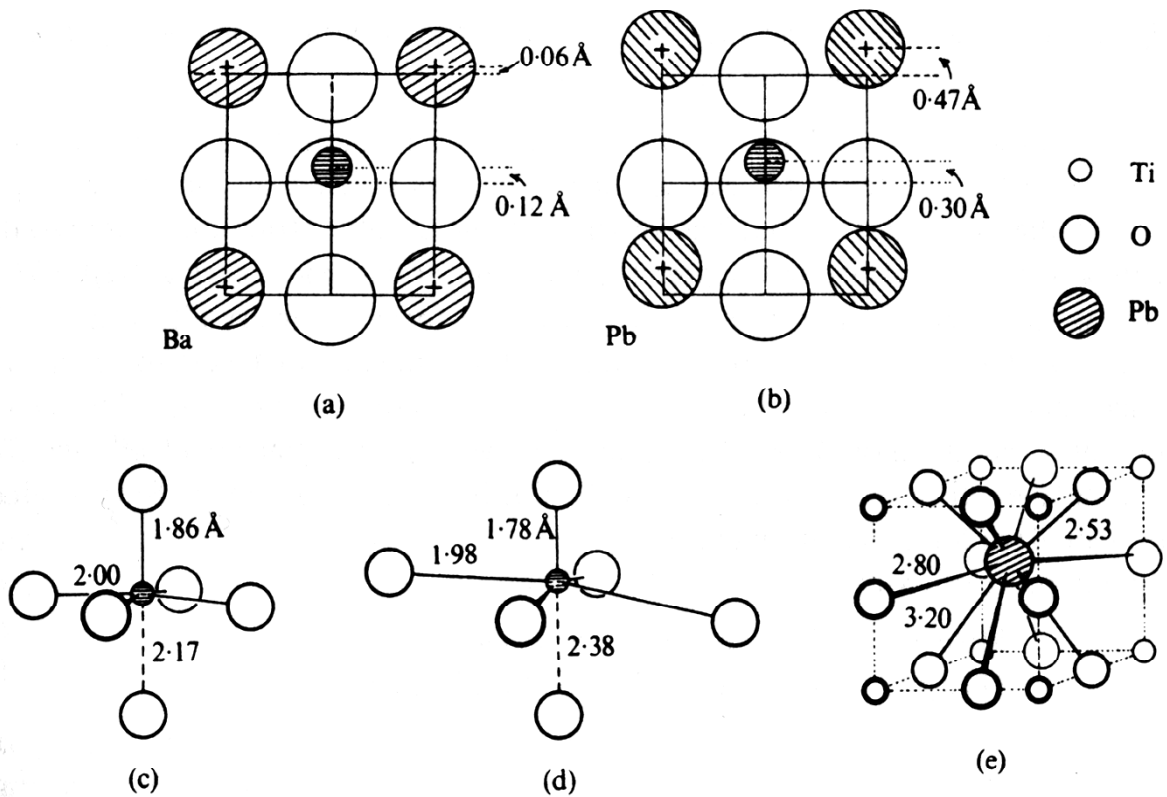


FIG.I.1.2. Environment of ions in perovskite-type structures (see text) [9].

For the determination of the structures of the tetragonal forms of BaTiO₃ and PbTiO₃ [9] both X-ray and neutron diffraction studies were used. The shifts of Ti and Ba (Pb) are conventionally shown relative to the O₆ octahedra around the original Ti position. In BaTiO₃ Ti shifts by 0.12 Å and Ba in the same direction by 0.06 Å (Fig.I.1.2(a)). In tetragonal PbTiO₃ Ti is shifted by 0.30 Å with respect to the oxygen octahedra and Pb moves in the same direction by 0.47 Å (Fig.I.1.2(b)). The Ti environments in these crystals are shown at (c) and (d). In both cases Ti is displaced from the centre of its octahedron giving one short Ti-O distance of 1.86 Å in BaTiO₃ and 1.78 Å in PbTiO₃. With regards to Ba, the shift has a negligible effect on the twelve Ba-O distances, but in the Pb compound the large shift of Pb does have an appreciable effect on the Pb-O distances as shown at (e). These distances may be compared with 2.78 Å, the sum of the Goldschmidt ionic radii for 12-coordination. This difference is the most marked one between ferroelectric BaTiO₃ and PbTiO₃, and the environment of Pb, with four short Pb-O distances to one side, is reminiscent of that in tetragonal PbO [9].

Ferroelectricity in perovskite-type materials manifests itself via reversible spontaneous polarization i.e. polarization can be switched by the application of an external bias field [1]. The value of polarization plotted vs. applied bias field shows a specific response called ferroelectric hysteresis. As an example, the hysteresis loop of PZT45/55 (the numbers denote the composition of the solid solution, the first number denotes the amount of Zr, the second the amount of Ti in mol.%) is illustrated in Fig.I.1.3(a) [10]. The hysteresis loop was taken at room temperature with a frequency of sinusoidal driving voltage at 100 Hz. The film of 500 nm thickness was deposited by conventional sol-gel method on a platinized commercial silicon substrate. There are two thermodynamically stable positions of B-ions inside the oxygen octahedra. Under electric field ion B is displaced upward or downward depending on polarity of electric field, as illustrated in Fig.I.1.3(b). This displacement generates a dipole moment inside the oxygen octahedra and leads to saturated polarization ($\pm P_s$). When the applied electric field is removed, the B atom remains in the displaced position and generates a remnant polarization ($\pm P_r$). In order to reverse the direction of polarization, a coercive field ($\pm E_c$), which is defined as a minimum electric field for switching the polarization, is needed.

As already mentioned, a number of theoretical approaches were proposed to explain the behaviour of ferroelectric crystals. One of the most widely known is the Landau-Devonshire theory [11]. The Landau-Devonshire formalism has been applied to ferroelectric thin films by Brennan [12]. The Landau-Devonshire model expresses the thermodynamic

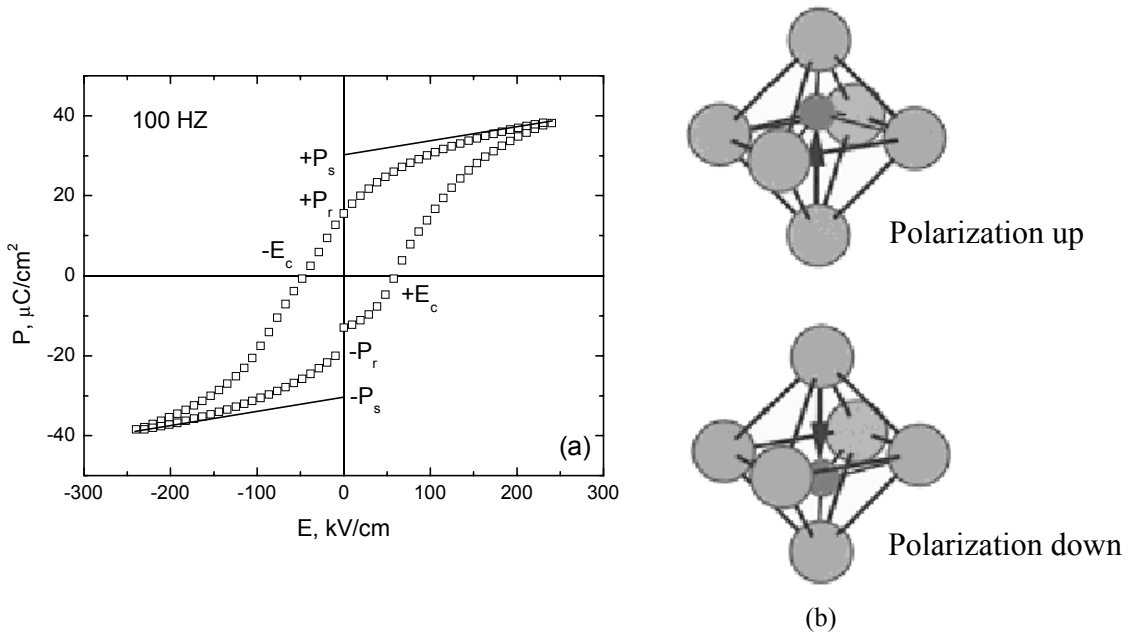


FIG.I.1.3. Ferroelectric hysteresis loop of PZT45/55 film ($d=500$ nm) measured with the frequency of driving signal of 100 Hz. The film was fabricated on platinized silicon substrate via conventional sol-gel method [10] (a); polarization reversal due to displacement of cation inside oxygen octahedra (b) [6].

properties of ferroelectric material in terms of the polarization, which serves as the Landau order parameter. A detailed model of the theory, taking into account nonhomogeneities of polarization, stresses and electrostrictive effects is rather complex, although, for the first simple examination of ferroelectric properties, the contribution of stress and electrostrictive effects can be omitted. Furthermore, since the lowest energy of the system is considered, saddle point approximation can be used [12]. Further, the uniform polarization of each domain is assumed. The resulting expression is a simple polynomial free energy function of polarization:

$$F(P) = \frac{1}{2}\alpha P^2 + \frac{1}{4}\beta P^4 + \frac{1}{6}\gamma P^6 \quad (\text{I.1.3})$$

where F is the free energy of the system, P is polarization, α , β and γ are Landau coefficients. The relation between the electric field and the polarization is given by the derivative of the free energy expression:

$$E = \frac{dF}{dP} = \alpha P + \beta P^3 + \gamma P^5 \quad (\text{I.1.4})$$

This expression for the electric field can be used in conjunction with the Poisson equation $\nabla \cdot \mathbf{D} = \rho_f$ (where \mathbf{D} is the dielectric displacements and ρ_f is the density of charged defects) to derive the contributions of charged defects to the local field and hence its influence

on the structure of the nearby domains [12]. The electric displacement induced by charged defects can be related to the electric field and polarization by the following familiar equations:

$$\begin{aligned} \mathbf{D} &= \epsilon_0 \mathbf{E} + \mathbf{P} \\ \nabla \mathbf{E} &= \frac{1}{\epsilon_0} (\nabla \mathbf{D} - \nabla \mathbf{P}) = \frac{1}{\epsilon_0} (\rho_f + \rho_b) \end{aligned} \quad (\text{I.1.5})$$

where ρ_b is the charge density due to the polarization of the ferroelectric lattice.

By expressing the polarization as a function of electric field the hysteresis of a single domain, single crystallite can be found. This gives a complex function if we use all terms of Landau expression. However, using only the two first terms of (I.1.4), a useful expression can be obtained.

$$E(P) = \alpha P + \beta P^3 \quad (\text{I.1.6})$$

This expression describes a simple bistable system which manifests the properties of hysteresis and coercivity. The inverse roots of expression (I.1.6) are straightforward to obtain. There are three roots, but only one of them is necessary to plot the real part of the polarization function. The real-valued

$$P(E) = -\frac{\alpha}{3\beta \left(\frac{E}{2\beta} + \sqrt{\frac{\alpha^3}{27\beta^3} + \frac{E^2}{4\beta^2}} \right)^{\frac{1}{3}}} + \left(\frac{E}{2\beta} + \sqrt{\frac{\alpha^3}{27\beta^3} + \frac{E^2}{4\beta^2}} \right) \quad (\text{I.1.7})$$

portion of this root forms one half of the hysteresis loop of the polarization vs. electric field. The return trace of the hysteresis is found by reflecting this function about the origin. Fig.I.1.4 shows the polarization hysteresis of single domain (or single crystalline which is in monodomain state) [12].

This simplified model provides the two characteristics of the ferroelectric that are most important for device application: remnant polarization and coercive field. However, we must note that processes related to real material behaviour like domain walls pinning, preferred domain configuration i.e. imprint, conductivity are out of consideration.

A thin ferroelectric film consists of many domains, which generally exhibit a distribution in their polar response [12]. The crystallites in a polycrystalline film will have a certain distribution in their orientation with respect to the electrodes, depending on the type of material and its microstructure. Those crystallites that are misaligned with respect to the field will be harder to switch than those that are more closely aligned, and this creates a distribution

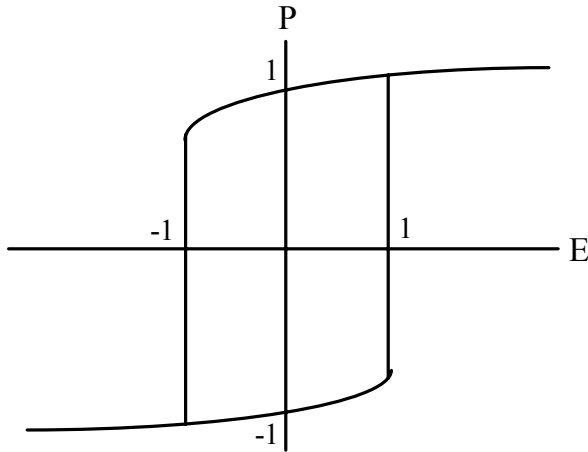


FIG.I.1.4. Polarization vs. electric field for the case of single domain [12].

of the effective coercive field among the collection of domains. Obviously, the distribution will be related to the number of allowed polarization directions in the lattice. For example, in the case of $\text{PbTiO}_3\text{-PbZrO}_3$ solid solution, depending on Zr to Ti ratio the number of allowed directions changes from 6 for Ti rich “tetragonal” compositions to 8 for Zr rich “rhombohedral” compositions. Thereby, the maximum number of directions is 14 which is peculiar to the MPB composition (PZT 52/48 at room temperature) where these two phases coexist. Distributions in the coercive voltage and remnant polarization can be also caused by pinning effects due to charged defects. Charged defects, defect dipoles and space charges may also create built-in fields that cause offsets in the polar response. For example the hysteresis loop of PZT45/55 ferroelectric film presented in Fig. I.1.3(a) is very similar to that given by Brennan [12] for a collection of identical domains, each obeying the Landau hysteresis function (I.1.7), but have a Gaussian distribution of offset voltages due to charged defects. The distribution of the offset voltages transforms the abrupt hysteresis function of the single domain into the “soft” hysteresis loop usually observed in the case of ferroelectric thin films. It is expected that real ferroelectric devices would have a distribution of all relevant parameters, including coercivity, remanence and offset. In the case of particularly large built-in fields due to trapped charges and defect dipoles, the offset potentials may exceed the coercive field of the domain, and the domain will have negative apparent coercive voltage [12]. In other words, the offset for particular domain may be large enough to force it into a preferred polarization state in the absence of an applied field. In some cases this process can be detrimental for functional properties of ferroelectric thin-film devices.

I.2. Phase transitions in ferroelectric materials.

Another important characteristic of ferroelectrics is the phase transition from the paraelectric (cubic) state to the ferroelectric (tetragonal/rhombohedral) state which occurs at a characteristic temperature called the Curie point T_C [p.11 in ref. 8]. When the temperature is in the vicinity of the Curie point, thermodynamic properties (such as dielectric, elastic, optical, and thermal properties) of the ferroelectric materials show anomalies as the structure of the crystalline material changes. For example, the dielectric constant in most ferroelectric crystals has a very large (abnormal) value (up to 10^4 - 10^5) [p.12 in ref. 8] near their Curie points. This phenomenon is usually called “dielectric anomaly” and considered to be the basic feature of ferroelectric materials.

The Landau-Devonshire thermodynamic approach describes the paraelectric-to-ferroelectric phase transition in terms of phase stability in the vicinity of transition temperature. For further discussions, Landau power series (I.1.3) must be rewritten taking into account that the coefficients α , β and γ are temperature dependent [13]:

$$F(T, P) = \frac{1}{2}\alpha(T)P^2 + \frac{1}{4}\beta(T)P^4 + \frac{1}{6}\gamma(T)P^6 \quad (\text{I.2.1})$$

Equilibrium value of polarization, P_0 , at fixed temperature, T , is the value at which the free energy of the system is minimum. In the absence of an external electric field, the stability condition of F with respect to infinitesimal change of P is

$$\left(\frac{\partial F}{\partial P} \right)_{P_0} = 0 \quad (\text{I.2.2})$$

or, considering (I.2.1),

$$P_0(\alpha(T) + \beta(T)P_0^2 + \gamma(T)P_0^4) = 0 \quad (\text{I.2.3})$$

The solution $P_0=0$ of the equation (I.2.3) corresponds to the paraelectric phase. Another solution, $P_0 \neq 0$, exists only under certain conditions. In fact, not any solution of (I.2.3) is stable. The stable solution can be found if

$$\left(\frac{\partial^2 F}{\partial P^2} \right)_{P_0} > 0 \quad (\text{I.2.4})$$

The second derivative of the free energy with respect to polarization is the reciprocal of the isothermal dielectric susceptibility χ_T^{-1} . In the presence of an external electric field

$$\frac{dF}{dP} = E \quad (\text{I.2.5})$$

and the stability condition (I.2.4) can be expressed as

$$\left(\frac{\partial^2 F}{\partial P^2}\right)_{P_0} = \frac{dE}{dP} = \chi_T^{-1} > 0 \quad (I.2.6)$$

Using (I.2.1), (I.2.6) can be rewritten as follows:

$$\chi_T^{-1} = \alpha(T) + 3\beta(T)P_0^2 + 5\gamma(T)P_0^4 > 0 \quad (I.2.7)$$

In the temperature range where the paraelectric phase is stable, $P_0=0$ and inequality (I.2.7) becomes

$$\chi_T^{-1} = \alpha(T) > 0 \quad (I.2.8)$$

In other words, $\alpha(T)$ must be positive at high temperature for the paraelectric phase to be stable and χ_T^{-1} must tend to zero at the boundary of stability of the paraelectric phase, T_0 . Hence, $\alpha(T)$ can be expanded in a Taylor series in $|T-T_0|$ in the vicinity of T_0 . Taking only the first-order term, we have

$$\begin{aligned} \alpha(T) &= \alpha'(T-T_0) \\ \alpha' &= \left(\frac{d\alpha}{dT}\right)_{T=T_0} > 0 \end{aligned} \quad (I.2.9)$$

Consequently, equations (I.2.8) and (I.2.9) bring us to the Curie-Weiss law for dielectric susceptibility of the paraelectric phase [13]:

$$\begin{aligned} \chi_T &= \frac{C}{T-T_0} \\ C &= \frac{1}{\alpha'} \\ T &> T_0 \end{aligned} \quad (I.2.10)$$

It is supposed further that (i) β and γ only weakly depend on temperature in the vicinity of phase transition, and (ii) $\gamma > 0$. The parameter β determines the character of the temperature dependence of the order parameter near the Curie point. $\beta > 0$ corresponds to the phase

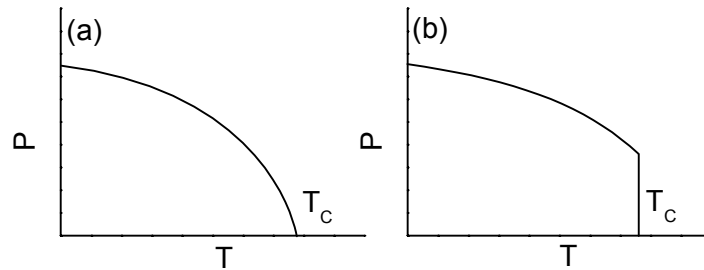


FIG.I.2.1. Temperature dependence of polarization in the case of phase transition of the second order (a) and the first order (b) [13].

transition of the second-order while at $\beta < 0$ a first-order transition takes place. In the case of a first-order transition, the polarization drops abruptly at T_C , whereas for a second-order transition P changes continuously as function of temperature (Fig.I.2.1). First-order transition is shown by BaTiO_3 and PbTiO_3 . Triglycine sulphate is an example of material which undergo second-order phase transition. Detailed discussions of the first and second order phase transitions can be found in a number of textbooks (see, e.g., ref's 8 (pp.16-24) and 13 (pp.36-46)).

I.3. Properties of some well known ferroelectric materials.

The first material of perovskite structure for which the phenomenon of ferroelectricity was reported is barium titanate (BaTiO_3) [14]. More thorough investigations of oxygen-octahedron-based materials have resulted in the discovery of ferroelectricity in PbTiO_3 , KNbO_3 , KTaO_3 , NaNbO_3 , NaTaO_3 , PbZrO_3 , PbHfO_3 , LiNbO_3 and LiTaO_3 (p. 103 in ref. 8). Among these compounds PbTiO_3 , PbZrO_3 and solid solution (PbZrO_3 - PbTiO_3) PZT became the most popular from the applied point of view due to high ferroelectric, pyroelectric and piezoelectric characteristics and relatively simple processing and handling procedures.

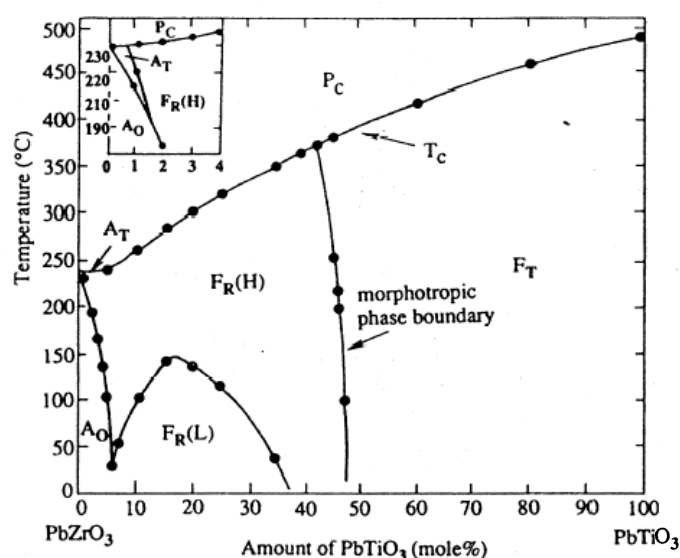


FIG.I.3.1. PbTiO_3 - PbZrO_3 subsolidus phase diagram [p. 109 in ref. 8]. P_C , A_T , A_O , $F_R(H)$, $F_R(L)$ and F_T denote paraelectric cubic, antiferroelectric tetragonal, antiferroelectric orthorhombic, ferroelectric rhombohedral (high temperature), ferroelectric rhombohedral (low temperature) and ferroelectric tetragonal phases, respectively.

Lead titanate (PbTiO_3) is a ferroelectric with a high Curie temperature (490°C) at which the phase transition from the cubic paraelectric phase to the tetragonal ferroelectric phase occurs. At room temperature, the structure of PbTiO_3 has a symmetry of the point group $4mm$ with the ratio of axes (tetragonality) $c/a = 1.063$. From the ferroelectric hysteresis loop of a PbTiO_3 single crystal, a spontaneous polarization of $52 \mu\text{C}/\text{cm}^2$ and a coercive field of

6.75 kV/cm are known [p.105-106 in ref. 8]. When Ti^{+4} ions in PbTiO_3 are partially replaced by Zr^{+4} with a molar ratio x , a solid solution of $x\text{PbZrO}_3-(1-x)\text{PbTiO}_3$ ($0 < x < 1$) binary system is formed. This solid solution is called lead zirconate titanate (PZT), and its chemical formula is $\text{Pb}(\text{Zr}_x\text{Ti}_{1-x})\text{O}_3$. PZT has the perovskite structure with Ti^{+4} and Zr^{+4} ions occupying B-sites at random. Fig.I.3.1 is the T - x phase diagram of the PZT pseudo-binary system, where the T_C -line is the boundary between the cubic paraelectric phase and the ferroelectric phase. A morphotropic phase boundary (MPB) separates the tetragonal phase region (on the Ti-rich side) from the rhombohedral phase region (on the Zr-rich side). At room temperature, the boundary is at the point $\text{Zr}/\text{Ti}=52/48$. In the region where Zr/Ti lies between 100/0 and 94/6, the solution is an antiferroelectric. Zr-rich (rhombohedral) area is also divided by low and high temperature rhombohedral phase, which both are ferroelectric. The lattice parameters of PZT are plotted against composition x in Fig.I.3.2 [p.109 in ref.8]. An abrupt change in the lattice parameters of PZT occurs near the composition corresponding to MPB, where some physical properties, such as dielectric constant, and piezoelectric electromechanical coupling factor, show maxima.

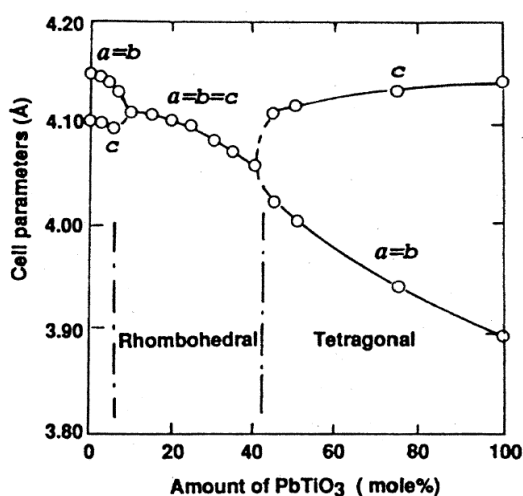


FIG.I.3.2. Lattice parameters at room temperature for the PbTiO_3 - PbZrO_3 system [p. 109 in ref.8].

II. Methods for ferroelectric thin films processing

In the present section, a short presentation of the most widely used thin film processing routes is made. The review of different methods of ferroelectric thin films deposition can be found in textbooks (see, for example ref's 15,16).

II.1. Electron beam evaporation.

This technique has been used mainly for high temperature superconducting oxide thin films [16-18], where it has typically been implemented by using individual thermionically produced electron beams, which are accelerated through 5-10 keV potential, magnetically deflected, and then focused onto spatially separated elemental targets located in water-cooled holders symmetrically positioned in front of the substrate. Process parameters, particularly precise film stoichiometry and sharp interfaces, are difficult to control, since direct sputtering of individual beams near each source is difficult without disturbing the focused electron beam. The evaporation of the elemental material from different spatial locations involves complex hardware and tends to produce nonuniform films across large-area substrates.

II.2. Pulsed laser deposition (PLD).

This method has been extensively used by many groups to produce multicomponent oxide thin films since the first demonstration of the technique for the production of superconducting $\text{YBa}_2\text{Cu}_3\text{O}_{7-x}$ films by ablation of material from sintered $\text{YBa}_2\text{Cu}_3\text{O}_{7-x}$ [16,19,20]. The impact of a laser beam (generally an excimer laser with wavelength of 248 or 193 nm) on the target, produces localized melting and resolidification that for some target materials results in topographical and compositional changes of the impacted area of the target, which affects the reproducibility of the film characteristics after several hundred pulses. The problem is solved by continuous rotation of the target and/or laser beam scanning on the surface to permanently expose a fresh area to the laser beam.

For the synthesis of ferroelectric PZT, initial work on laser ablation from continuously exposed fresh areas of a PZT target demonstrated the feasibility of producing deposited films at substrate temperatures of 500-600°C, and in oxygen atmospheres, needed for nucleation of the perovskite PZT film [16,21]. However, even in the presence of a seemingly appropriate oxygen atmosphere, early as-deposited PZT films contained a pyrochlore phase [16,22], possibly due to Pb deficiency in the film. Furthermore, PLD is particularly not suitable for large-area deposition.

II.3. Multi-ion-beam reactive sputter deposition (MIBRSD).

The basic idea of the MIBRSD technique is that individually mounted single-component targets are sputtered independently yet simultaneously by different ion sources, so that a highly controllable deposition process can be achieved [p. 429 in ref. 16]. Such technique, as can be expected, is rather complicated in instrumentation and requires a series of adjustments, modulations and calibrations. Since different single-element targets are sputtered individually by independently operated ion sources, the MIBRSD allows the utmost capability of varying and controlling the composition of deposited films.

II.4. Organometallic chemical vapour deposition (OMCVD).

Chemical vapour deposition processes (CVD), where volatile compounds of the elements to be incorporated into the solids, the so-called precursors, are transported via the gas-phase to the region where deposition takes place, are well known [p. 485 in ref. 16]. Historically, the most commonly used precursors are chlorides and hydrides. Such compounds are readily available, in most cases easy to handle and often have sufficiently high vapour pressures. Although, good results are usually obtained, process control is not always optimal and the contamination of the films with halogen ions is reported. To overcome this drawback the use of an alternative class of precursors – organometallic compounds (see below) was proposed [16,23].

Due to the advantages of this new type of precursors, such as lower temperature of decomposition, higher volatility as compared to the traditional sources, the OMCVD method allowed the fabrication of high quality, high temperature superconducting (HTSC) and ferroelectric materials in the form of thin films. OMCVD is a technique allowing direct formation of thin films in the proper crystalline phase and even epitaxial films for lattice

matched substrates. It has the advantage over most other techniques that a high oxygen partial pressure can be applied during the deposition. OMCVD can be easily scaled-up, both in wafer throughput as well as in wafer diameter. This makes the technique a promising candidate for deposition on an industrial scale. However, the technique involves high investment and operating cost.

II.5. Sol-gel processing of thin films.

Among the chemical deposition methods the sol-gel processing route have earned great attention [24] for coatings, fibres, ultrafine and ultrapure powders and bulk materials fabrication. Being firstly utilized by Budd *et al.* [25] for ferroelectric thin films deposition, e.g. PbTiO_3 , PbZrO_3 , $\text{Pb}(\text{Zr,Ti})\text{O}_3$ and $(\text{Pb,Lu})(\text{Zr,Ti})\text{O}_3$, the sol-gel method remains until now the method of choice for ferroelectric coating fabrication [26]. Analysis of the publications on ferroelectric thin films processing shows that the sol-gel method is the leading and most accessible one as compared to other physical and epitaxial (i.e. metalorganic chemical vapour deposition OMCVD) methods. High quality ferroelectric and relaxor thin films of different compositions are successfully obtained by sol-gel [27-32]. Unlike physical

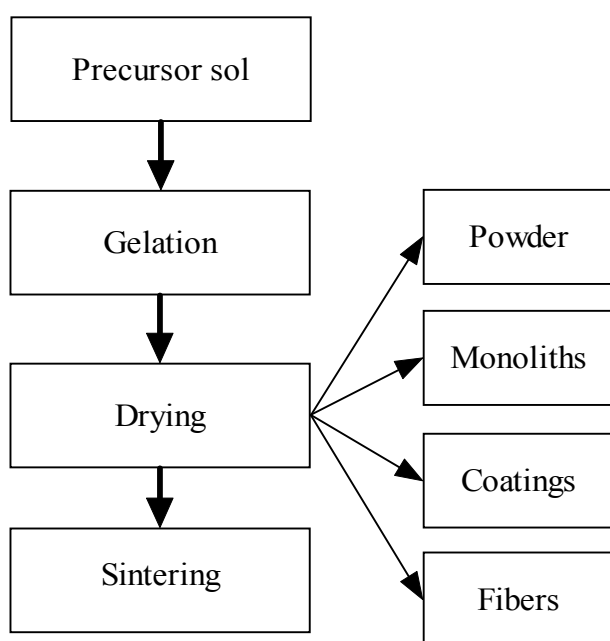
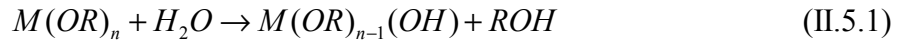


FIG.II.5.1. Generalized flow chart diagram of sol-gel process.

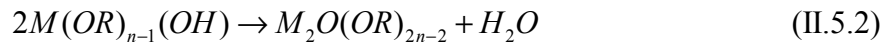
deposition methods mentioned above, the sol-gel route does not require sophisticated and expensive equipment; on the other hand it provides suitable stoichiometric control that is very important for the fabrication of oxides of complex stoichiometry such as perovskite

ferroelectrics. Many definitions of the sol-gel process have been proposed. One of them is “Sol-gel is the process of production of inorganic oxides either from colloidal dispersion or from metal alkoxides”. This definition has been introduced by Segal [33]. Although developments of sol-gel include now also the promising field of hybrid organic-inorganic materials [34], the definition of Segal is valid in the case of ferroelectric fabrication, where alkoxides are the basic reagents, and can be accepted in this work. Alkoxides are compounds with generalized chemical formula $M(OR)_n$. They are obtained from direct or indirect reactions between a metal M and an alcohol ROH . As an example the titanium alkoxides $Ti(OC_2H_5)_4$ (titanium ethoxide), $Ti(OC_3H_7)_4$ (titanium isopropoxide) and $Ti(OC_4H_9)_4$ (titanium butoxide) which can be used for TiO_2 or titanate fabrication can be mentioned. An exhaustive review on the history and chemistry of alkoxides can be found elsewhere [pp. 233-327 in ref. 16].

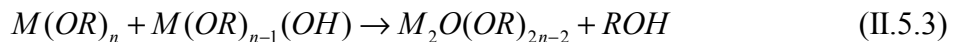
A simplified flow chart of the sol-gel process is given in Fig. II.5.1. The first step of sol-gel consists in the so-called precursor or sol preparation, usually by mixing the alkoxide with an appropriate solvent. Many routes can be utilized for solution preparation. In general two processes determine the structure and characteristics of particles in a sol. The first one is hydrolysis:



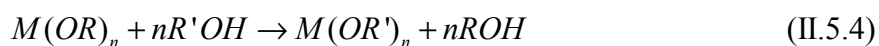
Since metal alkoxides are very reactive due to the presence of highly electronegative $-OR$ groups, the kinetic of reaction (II.5.1) is sensitive to ambient conditions, and sometimes the sol preparation requires an inert atmosphere with controlled humidity (N_2 , glove box). The second process involves the formation of $M-O-M$ bonds by oxolation reactions [26,35]:



or:

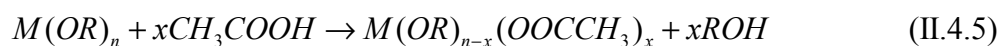


Different methods of solution fabrication can be classified according to the starting reagent used and the chemical reactions involved in alkoxide modification. The first one, most widely spread, utilizes $C_3H_8O_2$ (2-methoxyethanol) as solvent. In this case, the alkoxide modification occurs in the course of an alkoxy exchange reaction:



here -OR' is the methoxyethoxy group. The resultant methoxyethoxide $M(OR')_n$ is usually more stable and less sensitive to water.

The “hybrid” or “chelate” process uses other reagents for alkoxide modification by the chelating reaction:



Although as a chelating agent acetylacetone [36] or acetic acid [37,38] are usually used, 2-methoxyethanol can be utilized as a final solvent and agent controlling concentration and rheology of the solution.

Further growth of sol species, which are oligometric in nature, according to processes similar to (II.5.2) and (II.5.3) leads to the gelation of the sol. This is the next step of sol-gel processing (see Fig. II.5.1). A gel is a porous 3-dimensionally interconnected solid that expands throughout a liquid, and is limited only by the size of the container. The gel must then be dried at moderate temperatures to evaporate the solvent. Depending on conditions and technology of gelation and drying, powders, monoliths, coatings or fibers can be formed. In the case of thin film processing, spin-coating, dip-coating or spray-pyrolysis routes are usually utilized for thin dense layer formation. The final product is annealed at high temperature (but not higher than 1000°C) in order to complete phase transformation.

III. Applications of ferroelectric thin films

In this section some outstanding application potentials for ferroelectric thin films will be presented and discussed. The applications of ferroelectrics in passive electronic components such as high power capacitors will not be considered.

III.1. Non-volatile and dynamic random access memories.

As mentioned in the Introduction, the trend towards miniaturization and integration of electronic devices into the existent semiconductor circuits production technology has been the main driving force for the development of ferroelectric thin films [39]. The main efforts have been focussed on the development of non-volatile (NVRAM) and Dynamic Random Access Memory (DRAM) using ferroelectric thin films based on barium-titanate and lead-zirconate-titanate. Barium titanate based non-volatile memory was developed in the early 50's in the research laboratories of AT&T, Ford, IBM and Westinghouse [40]. The first storage devices comprised a 100 mm slice of single crystal BaTiO_3 provided with x-y addressed electrode matrix. An electric field was used to switch the spontaneous polarization, or "write", each ferroelectric cell into either positive or negative polarization state. From the perspective of binary encoding, one polarization state could be regarded as a "1", and the opposite as a "0". Whilst the principle of a ferroelectric memory was demonstrated, the device did not prove commercially practical because of the crystal being too expensive, excessive cross-talk between adjacent address lines, and the large write voltage required. With the advent of thin film ferroelectrics and the introduction of semiconductor architectures [41], non-volatile random access memories (NVRAM) have now become a commercially viable option.

Dynamic random access memory (DRAM) is the most widely used method of temporary data storage, providing the memory for all personal computers. In its structure it comprises a transistor connected to an integrated capacitor. A binary state is stored by maintaining a potential on the capacitor but, because the capacitor discharges, its voltage is refreshed several times per second. Since ferroelectric materials typically show large dielectric constants, ferroelectric thin films have been considered as strong candidates for high

density DRAM applications. As the density of DRAM increases over 1 Gbit, the cell size is tremendously reduced, so that the current SiO₂ dielectric layer is regarded as impractical due its low dielectric constant of typically 4. Practically the charge storage capability can be improved either by increasing the capacitive area or the dielectric constant for a given dielectric layer thickness. However, in conventional DRAM most of the space is occupied by the capacitor, therefore in order to reduce cell size the area of the capacitor must be decreased. Therefore, the search for high-permittivity thin films is a reasonable choice. Since most of the commonly used ferroelectrics have dielectric constants at least two orders of magnitude higher than that of SiO₂, ferroelectric thin films can be used as non-switching capacitor materials in high density DRAM devices. Some excellent work on the application of ferroelectric thin films for memory devices fabrication has been published [42 and references therein]. An exhaustive description of materials and device issues in the application of ferroelectric thin films for memory devices can be found in the monograph of Scott [15].

III.2. Microelectromechanical systems.

Microelectromechanical systems (MEMS) combine traditional Si-integrated circuit (IC) electronics with micromechanical sensing and actuating components. According to [43], the term MEMS has become synonymous for many types of microfabricated devices such as accelerometers, flow-meters, micro-pumps, motors and mechanical components. The ultimate goal of MEMS is a self-contained system of interrelated sensing and actuating devices together with signal processing and control electronics on a common substrate, most often Si. Since fabrication involves methods common to the IC industry, MEMS can be mass-produced. Commercial applications of MEMS already span biomechanical, manufacturing, information processing, and automotive industries. More applications are projected in consumer electronics, manufacturing control, communications, and aerospace. Ferroelectric materials have many properties desirable for MEMS applications. The strong piezoelectric effect allows electromechanical sensing and actuation. The spontaneous charge induced from mechanical strain in ferroelectric thin films is easily sensed across a capacitor structure using a voltage- or charge-sensitive amplifier. Direct and converse piezoelectric effects in ferroelectric materials are expressed as [6]:

$$D = dT + \epsilon^{T} E \quad (\text{III.2.1})$$

$$S = s^E T + dE \quad (\text{III.2.2})$$

where D is the dielectric displacement, T the stress, S the strain, d the piezoelectric coefficient* and s the material compliance (inverse of modulus of elasticity). The direct effect (III.2.1) is identified with the phenomenon whereby electrical charge (polarization) is generated from a mechanical stress, whereas the converse effect (III.2.2) is associated with the mechanical movement generated by the application of an electrical field. The superscripts in (III.2.1) and (III.2.2) indicate the quantity held constant: in the case of ϵ'^T , the stress is held constant, which means that the piezoelectric element is mechanically unconstrained, and, in the case of S^E , the electric field is held constant, which means the electrodes on the elements are shorted together.

Electrostriction is another electromechanical effect which can be exploited for MEMS application. In electrostriction, the sign of the deformation that occurs as a result of an applied electric field is independent of the polarity of the field [6], and the value of deformation has a quadratic dependence on the applied field (in piezoelectricity, the deformation is linear with respect to the applied field and changes sign when the field is reversed). The corresponding equation in terms of electric field is:

$$S = mE^2 \quad (\text{III.2.3})$$

and in terms of polarization:

$$S = QP^2 \quad (\text{III.2.4})$$

where m and Q are corresponding electrostrictive coefficients.

Although electrostriction is a general property of all dielectric materials, whether they are crystalline, amorphous, polar, or centrosymmetric, it can be particularly large in ferroelectric materials just above their Curie point, where an electric field can enforce the energetically unstable ferroelectric phase. More commonly this effect is utilized to good advantage in relaxor materials, such as lead magnesium niobate (PMN), lead zinc niobate (PZN), and lead lanthanum zirconate titanate (PLZT). Electrostrictive materials can be operated either in the electrostrictive mode (as stated above) or in the field-biased piezoelectric mode [6]. Device design for electromechanical applications typically includes a thin, flexible structural material covered with the ferroelectric thin film sandwiched between metal electrodes.

* In general, since piezoelectric coefficient is a second-rank tensor value, it is correct to write d in the equations (III.2.1) and (III.2.2) as the tensor components; in the case of polycrystalline thin films we are talking about the effective value of piezoelectric coefficient, d_{eff} . Notation d_{33} is also used sometimes to represent piezoelectric coefficient measured in the direction perpendicular to film surface.

III.3. IR detectors.

IR (infrared) detector arrays and IR cameras play an extremely important role in military and civil applications [44]. Infrared imaging systems have been used for 30 years to provide operational capability in the dark of the night. Traditional night vision systems have been large and costly, and their use has been therefore restricted to aircraft and heavy platforms. Today photon (quantum) detectors in combination with mechanical scanning technique are widely used for these night vision systems. Photon detectors convert absorbed IR radiation directly into an electrical signal. These detectors can be quite sensitive, but need to be cryogenically cooled in order to suppress their noise mechanisms. Until recently, these

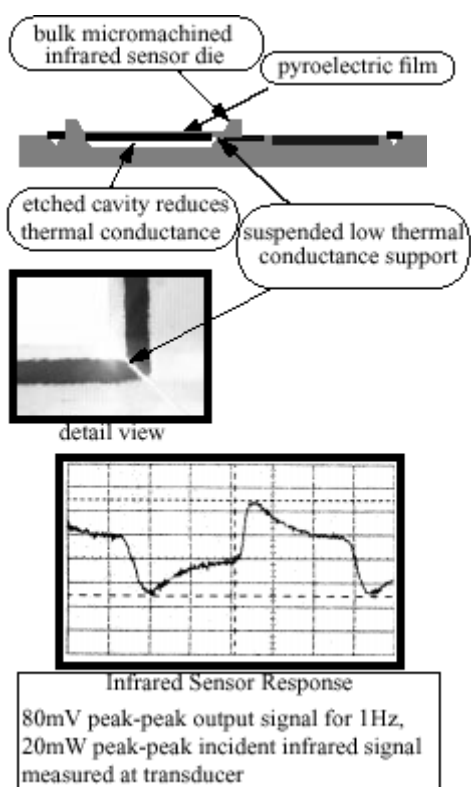


FIG.III.3.1. Scheme of the integrated ferroelectric thin film based pyroelectric detector. Inset shows voltage response to 20 mW incident IR signal.

detectors were considered only for military applications. This situation is completely different for civilian and commercial applications. There is a large potential for application of IR detectors and cameras, which can include surveillance of buildings, the detection and fire-fighting, and night driving assistance. IR detectors and cameras could have a large impact in these areas if their costs can be reduced considerably. Alternatively to IR photonic detectors a cheap technology makes use of the pyroelectric properties inherent to ferroelectric ceramics and thin films. The latter can be easily incorporated into the silicon circuit as exemplified in Fig.III.3.1. For these films, there is no need for cooling and they do not show spectral

dependence [44]. The absorbed IR radiation results in a temperature change of the detector elements, which in turn leads to an electrical response due to the temperature dependence of the spontaneous polarization of the detector material (pyroelectric effect). Dielectric displacement \mathbf{D} in ferroelectric materials is given by the equation

$$\mathbf{D} = \varepsilon' \varepsilon_0 \mathbf{E} + \mathbf{P}_s \quad (\text{III.3.1})$$

where \mathbf{E} , ε' , and ε_0 are the external electric field, the dielectric constant and the permittivity of free space, respectively [45]. Therefore at the constant field

$$\frac{d\mathbf{D}}{dT} = \frac{d\mathbf{P}_s}{dT} + \mathbf{E} \varepsilon_0 \frac{d\varepsilon'}{dT} \quad (\text{III.3.2})$$

and

$$\mathbf{p}_g = \mathbf{p} + \mathbf{E} \varepsilon_0 \frac{d\varepsilon'}{dT} \quad (\text{III.3.3})$$

where

$$\mathbf{p} = \frac{d\mathbf{P}_s}{dT} \quad (\text{III.3.4})$$

\mathbf{p}_g and \mathbf{p} are referred as generalized and true pyroelectric coefficients, respectively.

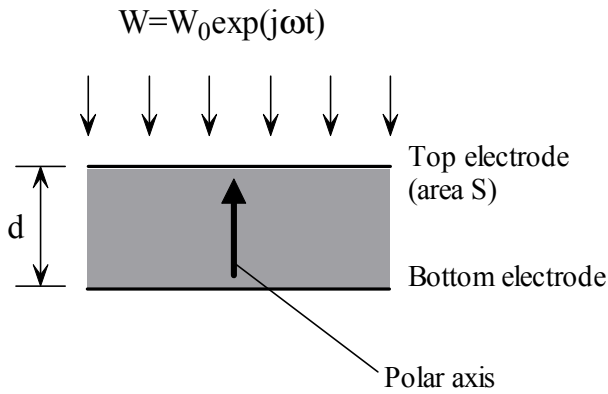


FIG.III.3.2. Face-electroded IR detector [44].

A freely suspended single element detector with electrodes deposited on the surface normal to the polarization axis is illustrated schematically in Fig. III.3.2 [44]. The detector is characterized by the thickness d , area S , pyroelectric coefficient p , emissivity η , thermal capacity H and thermal conductance (to the surroundings) G . The thermal time constant τ_T of this detector is determined as [44]:

$$\tau_T = \frac{H}{G} \quad (\text{III.3.5})$$

The element is exposed to a sinusoidally modulated radiation flux with a power density W (see Fig.III.3.2). The temperature difference between the detector and its surroundings is expressed as follows:

$$\eta W = H \frac{dT}{dt} + GT \quad (\text{III.3.6})$$

The solution of the equation is:

$$T = \frac{\eta W_0}{G + j\omega H} \exp(j\omega t) \quad (\text{III.3.7})$$

where j , ω and t are complex operator, angular frequency and time, respectively. Usually the output of the pyroelectric detector is amplified using current or voltage amplifiers. The electrical time constant of the detector is determined by the capacitance, C_T , and the resistance, R_T , of the circuit and expressed as:

$$\tau_E = R_T C_T \quad (\text{III.3.8})$$

It is usually convenient to define quantities such as the current responsivity, R_I , which is the pyroelectric current generated by the detector per watt of input power:

$$R_I = \frac{I_p}{W_0} = \frac{\eta p S \omega}{G(1 + \omega^2 \tau_T^2)^{1/2}} \quad (\text{III.3.9})$$

If $\omega \ll 1/\tau_T$, R_I is proportional to ω . At high frequencies, R_I is constant and determined by the thermal and pyroelectric properties of the detector material and detector geometry [44]:

$$R_I = \frac{\eta p}{c' d} \quad (\text{III.3.10})$$

The electrical admittance of the detector circuit is:

$$Y = \frac{1}{R_T} + j\omega C_T \quad (\text{III.3.11})$$

The voltage responsivity (pyroelectric voltage generated per watt of input power) is given by:

$$R_V = \frac{V_p}{W_0} = \frac{R_T \eta p S \omega}{G(1 + \omega^2 \tau_T^2)^{1/2} (1 + \omega^2 \tau_E^2)^{1/2}} \quad (\text{III.3.12})$$

The voltage responsivity of the detector is illustrated schematically in Fig. III.3.3. Three regions in $R_V(\omega)$ curve can be distinguished. When $\omega < 1/\tau_T$, the responsivity is proportional to the frequency. At high frequency ($\omega > 1/\tau_E$) the responsivity is proportional to $1/\omega$ and given by:

$$R_V = \frac{\eta p}{c' d C_T \omega} \quad (\text{III.3.13})$$

In the intermediate frequency range $R_V(\omega)$ is rather flat and has its maximum at $\omega=1/(\tau_T\tau_E)$. The maximum value of the voltage responsivity is therefore expressed as:

$$R_V(\text{max}) = \eta p S \frac{R_T}{G(\tau_T + \tau_E)} \quad (\text{III.3.14})$$

Using high IR-absorbing materials as top electrodes (maximising η) and minimising τ_T by making the detector thinner (minimising the thermal capacity) and thermally isolating it (minimising G) can improve the responsivity of certain pyroelectric detector.

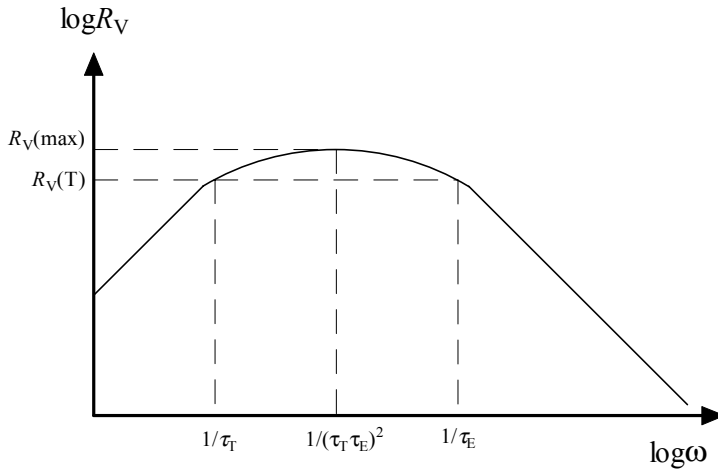


FIG.III.3.3. Frequency variation of voltage responsivity of a pyroelectric detector [44].

There are different figures of merit (FOM) of pyroelectric materials which determine the applicability of the materials under specific conditions. The most important of them are the current FOM which can be expressed as:

$$F_I = \frac{p}{c'} \quad (\text{III.3.15})$$

the voltage FOM:

$$F_V = \frac{p}{c' \epsilon' \epsilon_0} \quad (\text{III.3.16})$$

and detectivity FOM:

$$F_D = \frac{p}{c' \sqrt{\epsilon' \epsilon_0} \tan \delta} \quad (\text{III.3.17})$$

where c' is the volume specific heat and $\tan \delta$ is the loss tangent respectively [44,45]. We can see that the applicability of the material for pyroelectric devices depend on thermal properties, as well dielectric and ferroelectric properties. A good FOM involves high pyroelectric coefficient, p , low ϵ' and $\tan \delta$.

As already mentioned in the Introduction, the advantage of a thin-film device is that the material can be directly deposited on the integrated circuit. The same materials which are actively used for discrete IR detectors fabrication are usually considered for the applications in thin-film devices. These materials are mainly complex oxides of perovskite (like BaTiO₃ or PbTiO₃) and perovskite related (e.g. LiTaO₃ or (Sr,Ba)Nb₂O₆) structures. Lead zirconate titanate based perovskite-type thin films have become of considerable importance from the point of view of their potential applications in IR devices and imaging systems due to good pyroelectric and dielectric properties and relatively low processing temperature. The properties of PZT of various composition are listed in Table III.3.1 (taken from Wersing and Bruchhaus [44], p. 185).

Table III.3.1. Dielectric and pyroelectric properties of PZT thin films of different compositions (Wersing and Bruchhaus, [44], p. 185).

PZT film	ϵ'	$\tan\delta$	$p, 10^{-4} \text{ C/m}^2\text{K}$	$p, 10^{-4} \text{ C/m}^2\text{K}$ (after poling)
PZT(10/90)	172	0.006	2.09	2.02
PZT(20/80)	209	0.007	2.14	2.16
PZT(24/76)	245	0.006	2.12	2.31
PZT(38/62)	539	0.01	1.57	2.50
PZT(44/56)	665	0.014	1.28	2.39
PZT(48/52)	767	0.014	0.33	1.33
PZT(60/40)	598	0.011	0.11	1.24

Furthermore, the performance and properties stability of the active element of the IR detector are affected by the degree of preferred orientation, material composition and fabrication conditions. All these factors are even more important in the case of thin films of sub-micron thickness suspended on the substrate with specific properties and will be discussed in more details in the following.

IV. Characterization of ferroelectric materials

In the present chapter the basics of the methods used for the characterization of the structural and electrophysical properties of ferroelectrics are briefly described. The Experimental details will be presented separately in Chapter VII.

IV.1. X-ray diffractometry.

The basics and the theoretical background of the X-ray diffractometry (XRD) can be found in a number of textbooks (see, for example ref. 46). X-rays are electromagnetic radiation with typical photon energies in the range of 100 eV - 100 keV. For diffraction applications, only short wavelength X-rays (hard X-rays) in the range of a few angstroms to 0.1 angstrom (1 keV - 120 keV) are used. Because the wavelength of X-rays is comparable to the size of atoms, they are ideally suited for probing the structural arrangement of atoms and molecules in a wide range of materials. The energetic X-rays can penetrate deep into the materials and provide information about the bulk structure. X-rays are produced by either X-ray tubes or synchrotron radiation. In an X-ray tube, which is the primary X-ray source used in laboratory X-ray instruments, X-rays are generated when a focused electron beam accelerated across a high voltage field bombards a stationary or rotating solid target. As electrons collide with atoms in the target and slow down, a continuous spectrum of X-rays are emitted, which are termed Bremsstrahlung radiation. The high energy electrons also eject inner shell electrons in atoms through the ionization process. When a free electron fills the shell, an X-ray photon with energy characteristic of the target material is emitted. Common targets used in X-ray tubes include Cu and Mo, which emit 8 keV and 14 keV x-rays with corresponding wavelengths of $\sim 1.54 \text{ \AA}$ and $\sim 0.8 \text{ \AA}$, respectively. (The energy E of an X-ray photon and its wavelength are related by the equation $E=hc/\lambda$, where h is Planck's constant, c the speed of light and λ is the wavelength). Bragg's Law of X-ray diffraction is given by the following formula:

$$2d \sin \Theta = n\lambda \quad (\text{IV.1.1})$$

A monochromatic X-ray beam with a wavelength λ incident onto a crystalline material at an angle Θ , leads to diffraction when the distance travelled by the rays reflected from successive planes differs by a complete number n of wavelengths. By varying the angle *theta*, the Bragg's Law conditions are satisfied by different d -spacings in polycrystalline materials.

One of the most significant drawbacks limiting the applicability of conventional X-ray powder diffractometry for the characterization of thin films of submicron thickness is the contribution of substrate material to XRD spectra due to relatively high penetration depth of X-rays. Very often diffracted reflections which belong to the substrate material mask the reflections coming from the film. Moreover, when the specimen consists of polycrystalline thin film deposited on single crystal or highly textured polycrystalline substrate, the intensity of the peaks diffracted from substrate can exceed the reflections from the films by many orders of magnitude. The acquisition of X-ray spectra from thin films using grazing incidence (GI) adjustment of the diffractometer is one of the possibilities to avoid reflections from substrate [47]. In this experimental configuration the specimen is aligned in such a way as to expose the surface of the film to the incident X-ray beam at a very low ("grazing") angle (usually $1-2^\circ$, as illustrated schematically on Fig. IV.1.1) which is kept constant during the experiment. This increases significantly the path of X-rays within the thin film. The spectra are obtained by changing the position of the secondary goniometer in the desired range of angles (2Θ) with appropriate duration and step width.

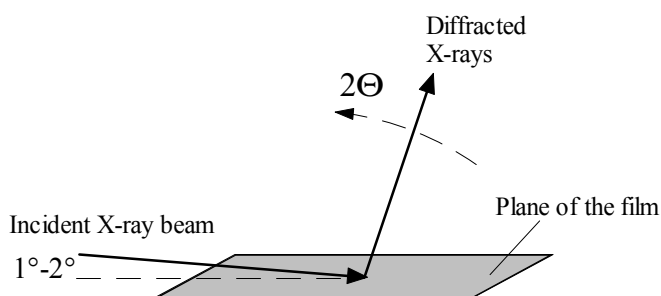


FIG.IV.1.1. Scheme of grazing incidence XRD experiment.

Texture analysis is another important application of X-ray diffractometry. In view of the tensor nature of the electrophysical properties, correlation between preferentially oriented state and dielectric, ferroelectric and piezoelectric properties of ferroelectric polycrystalline thin films is of crucial importance, and have been thoroughly investigated [48-51]. It has to be noted that comparison of the spectra obtained in Θ - 2Θ configuration for textured and random (powdered) specimens gives an idea only about out-of-plane (in the case of the films

perpendicular to the plane of substrate) texture, and in the most of the cases analysis of pole figures is required to reconstruct the full picture of diffracted intensity distribution with respect to the plane of the substrate. Exhaustive theoretical background on the application of X-ray diffractometry and pole figures for texture analysis can be found in textbooks [52-54]. The acquisition of a direct pole figure consists in the registration of the diffracted intensity distribution around the chosen peak. The situation is depicted on Fig. IV.1.2. The specimen is fixed at the angular position ($\Theta-2\Theta$) corresponding to Bragg conditions of one of the reflection. Then the specimen is tilted by an angle Chi with subsequent rotation around the normal to the sample surface (angle Phi). The distribution of the diffracted intensity, usually plotted in the contour plot form, vs. Phi and Chi is called direct pole figure.

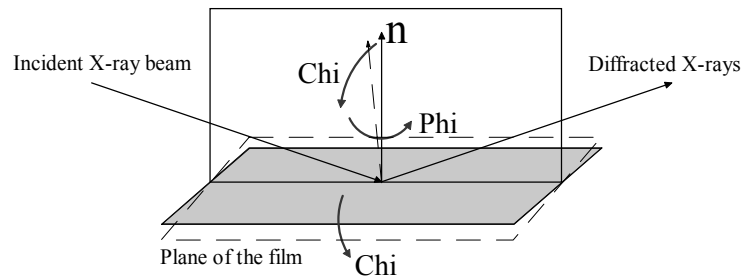


FIG.IV.1.2. Direct pole figure acquisition-scheme of the experiment.

Fibre texture (FT) is usually found for the majority of thin films deposited onto polycrystalline substrates via sol-gel method (a uniform pole density distribution with respect to the azimuthal angle, Phi, indicates the fibre or uniaxial character of the texture). Therefore in the following discussion we will mainly concentrate on the analysis of the FT plots (which are simply the cross-sections of the corresponding pole figures $\text{Phi}=\text{const}$) since the acquisition of a complete pole figure is rather a time consuming experiment.

IV.2. Raman spectroscopy.

After the inelastic scattering of light (Raman effect) was discovered [55] and laser technique developed, Raman spectroscopy has become widely used by physicists and materials scientists for studying excitation processes in solids. Nowadays, a number of spectrometers is available commercially. The theoretical background is given in standard textbooks (see, for example ref. 56). Scattering from time-varying structures (vibration of atoms) is accompanied with conservation of energy:

$$\hbar\omega_0 - \hbar\omega \pm \hbar\omega(\mathbf{q}) = 0 \quad (\text{IV.2.1})$$

where \hbar is the reduced Planck's constant, ω_0 and ω are frequencies of incident and scattered light and \mathbf{q} is wave vector of the elementary excitation of lattice, i.e. phonon [56]. Usually a Raman spectrum consists in set of frequencies or bands. Each band corresponds to specific elementary excitation of lattice. In a Raman spectroscopy experiment, the sample surface is irradiated with a monochromatic polarized light (usually from Ar- or HeNe-laser). The scattered light is then registered with an appropriate detector. Since the intensity of inelastically scattered light is several orders of magnitude weaker than that of elastically scattered (Rayleigh scattering), up-to-date Raman experiment involves a number of sophisticated techniques for signal registration and processing. Apart from the investigations of lattice dynamic processes in solid matter, Raman spectroscopy is actively used in materials science to analyse the structural properties and quality of surfaces and thin films. For example, a Raman spectrum is known to be sensitive to the crystallinity (when polycrystalline specimen is considered) of materials, stresses and surface states. A detailed description of Raman spectra of tetragonal perovskite ceramics and thin films will be given in the following.

IV.3. X-ray photoelectron spectroscopy.

X-ray photoelectron spectroscopy (XPS) is one of the powerful methods of surface analysis developed over the past 20 years [56]. In XPS, the specimen is irradiated under ultra-high vacuum with soft monochromatic X-rays which cause photoionisation of core electrons of atoms in the specimen. If the photoelectrons have kinetic energies high enough for overcoming the work function of the specimen, they escape from the specimen surface and can be collected with an appropriate detector. So-called 127° analyser is often used. Main parts of this detector are cylindrical sector plates and exit slit. Applying a variable voltages across the plates allows the electrons with different kinetic energy to pass through the exit slits (p. 153 in ref. 56). Since the levels of core electrons are quantised, the kinetic energies of emitted electrons provide information on the chemical composition of the sample investigated. The kinetic energy E_k of the photoelectron is expressed by Einstein relation $E_k = h\nu - E_b$. The term $h\nu$ present incident X-ray energy. E_b is the binding energy which is equal to the ionisation energy of the electron. Due to strong absorption of the photoelectrons by the sample material, the escape depth, which is dependent on the kinetic energy of the photoelectron, usually does not exceed 5 nm. Therefore XPS has become a popular method for *in situ* surfaces and thin films analysis. When XPS analysis is accompanied with ion

milling it allows depth analysing and profiling of element distribution in near-surface regions of specimen. As an example, Fig. IV.3.1 illustrates the results of Fe distribution profiling vs. depth of a PZFNT/PZT pyroelectric bimorph thin film (see ref. 58 for experimental details). Milling with Ar ions with subsequent XPS investigation and analysis of the intensities of XPS peaks ($2p_{1/2}$ and $2p_{3/2}$ of Fe on Fig.IV.3.1(a)), has let us to reconstruct Fe distribution profile in our specimen (Fig.IV.3.1(b)).

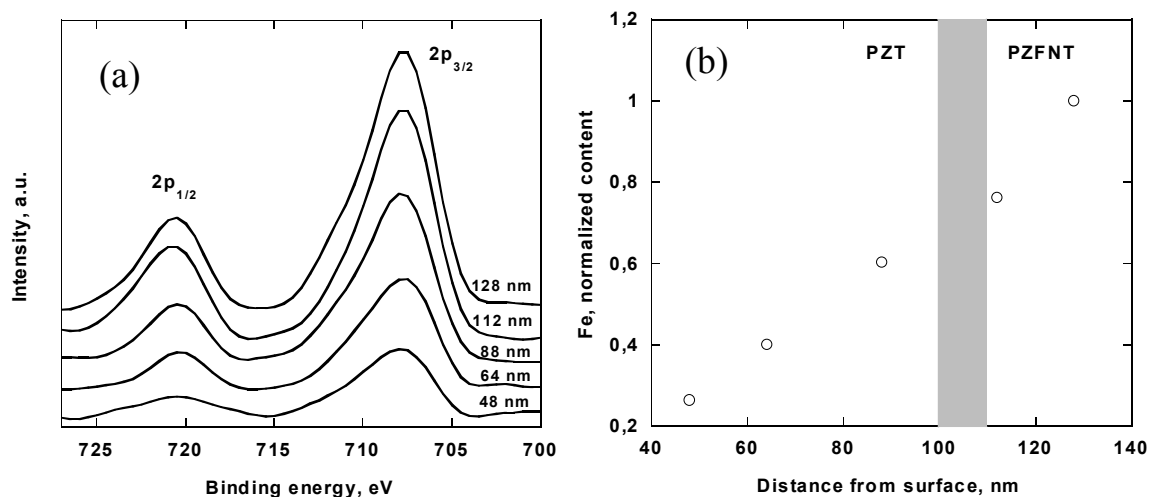


FIG.IV.3.1. Dependence of $2p_{1/2}$ and $2p_{3/2}$ Fe peaks intensity vs. depth of a heterostructure consisting of PZFNT and PZT successive coatings (a), and Fe distribution through thickness of the specimen (painted area shows approximate position of the PZT/PZFNT interface) (b) [58].

IV.4. Scanning electron microscopy.

The standard technique which is used for high resolution imaging of solid surfaces is now scanning electron microscopy (SEM). Many scanning electron microscopes are commercially available. In SEM, an electron beam source emits electrons which are then collected and focused by lenses to form few nanometres sized probes. Deflection coils are used to operate electron beam and scan sample surface. Simultaneously, another electron beam runs over a TV monitor screen in a synchronized mode. The image magnification is the ratio of the scanned monitor range to the scanned sample range, and it is easily controllable by beam deviation elements. Primary electron beam interacts with the specimen surface in a complicated manner resulting in different emitted signals (secondary and back scattered electrons, Auger electrons, cathodoluminescence and X-ray radiation) which could be registered with the appropriate detector. SEM is a versatile and routine surface characterization method and is described in standard text books [59].

IV.5. Atomic force microscopy.

Over the last years atomic force microscopy (AFM) has become a standard and widely used technique for surface characterization, readily providing sub-nanometer resolution. Detailed description of the technique can be found in a number of texts and device manuals (see e.g. ref's 60 and 61)). Two main operation modes, viz. contact and non-contact, were developed and are now available in many commercial devices. In contact mode AFM, a very sharp tip, mounted on a flexible cantilever (Fig.IV.5.1), is attached to the sample surface. The sample is scanned under this probe with three-dimensional piezoelectric scanner (scheme when the cantilever instead of the probe is mounted on the scanner is also realized in some devices). The deflection of the cantilever is measured using laser beam reflected from cantilever and position-sensitive photodetector in order to obtain the surface profile or topography of the specimen (Fig.IV.5.1).

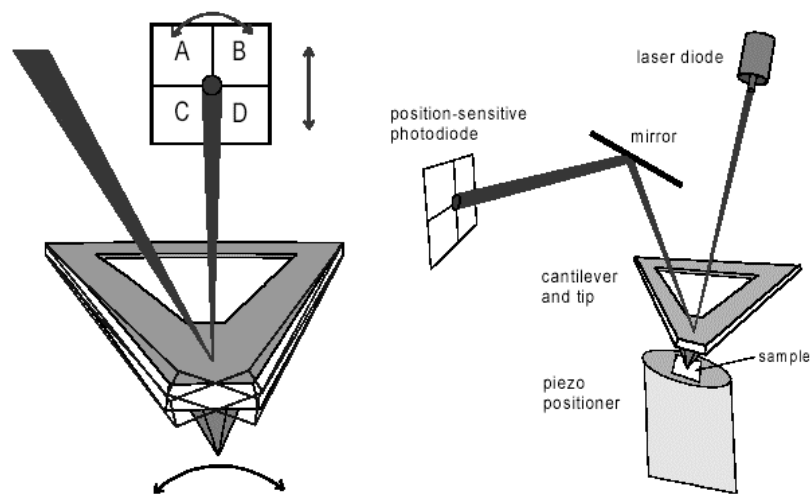


FIG.IV.5.1. Cantilever and photodiode (left) and schematic diagram of contact mode (right) [60].

In non-contact (also called tapping) mode, the cantilever is oscillated at its resonant frequency at a given distance from the sample (several nanometers) and scanned over its surface. The system changes the sample (or cantilever) vertical (Z) position to maintain constant frequency/amplitude of cantilever oscillation. The topography of the surface can be reconstructed from the vertical (Z) position of the piezoscanner. The phase frequency variation of the cantilever provides additional useful information about the tip-specimen interaction and hence sample surface properties. Fig.IV.5.2 exemplifies cantilevers usually used for contact (silicon nitride, left) and non-contact (silicon, right) AFM modes [61].

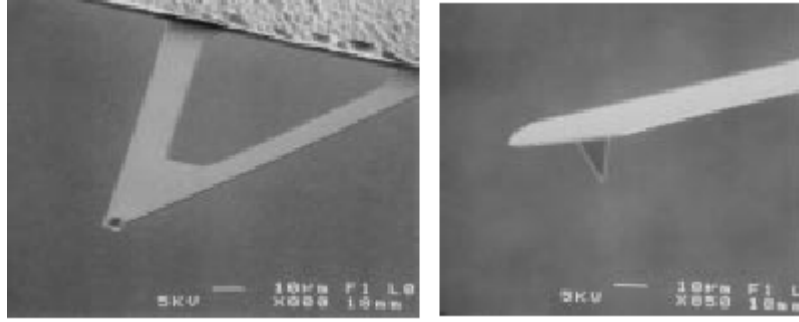


FIG.IV.5.2. Two types of the cantilevers: silicon nitride (left) and silicon crystal (right) (SEM micrographs) (p. 2-11 in ref [61]).

IV.6. Ellipsometry.

Ellipsometry is a powerful method for high precision measurements of optical properties and thickness of thin films. Ellipsometry is based on the reflection of light from a surface [62]. It is supposed that the incident plane wave moves in the direction suggested in Fig.IV.6.1, and that this wave is reflected from the surface as shown in the figure. The plane of incidence is defined as being the plane containing the light beam prior to and after the reflection. The plane of incidence also contains the normal to the surface. We shall refer to plane polarized waves that are in the plane of incidence as “p waves” and plane waves polarized perpendicular to the plane of incidence as “s waves” [62] (E_p and E_s are corresponding components of electric field vector). Suppose that there is the light beam reflecting at an interface between medium 1 and 2 as shown in Fig. IV.6.2. Some of the light is reflected and some is transmitted. The Fresnel reflection coefficient r is the ratio of the amplitude of the reflected wave to the amplitude of the incident one for a single interface. The Fresnel reflection coefficients are given by

$$r_{12}^p = \frac{N_2^* \cos \varphi_1 - N_1^* \cos \varphi_2}{N_2^* \cos \varphi_1 + N_1^* \cos \varphi_2}; \quad r_{12}^s = \frac{N_1^* \cos \varphi_1 - N_2^* \cos \varphi_2}{N_1^* \cos \varphi_1 + N_2^* \cos \varphi_2} \quad (\text{IV.6.1})$$

where N_1^* and N_2^* are the complex refractive indices of matter. The superscripts in r refer to waves parallel or perpendicular to the plane of incidence and the subscript refers to either medium 1 or medium 2. Many real situations involve multiple interfaces, as it is shown in Fig.III.6.3 [p. 15 in ref. 62]. The resultant reflected wave is made up of the light reflected directly from the first interface plus all of the transmissions from the light approaching the first interface from medium 2. Each successive transmission back into medium 1 is smaller.

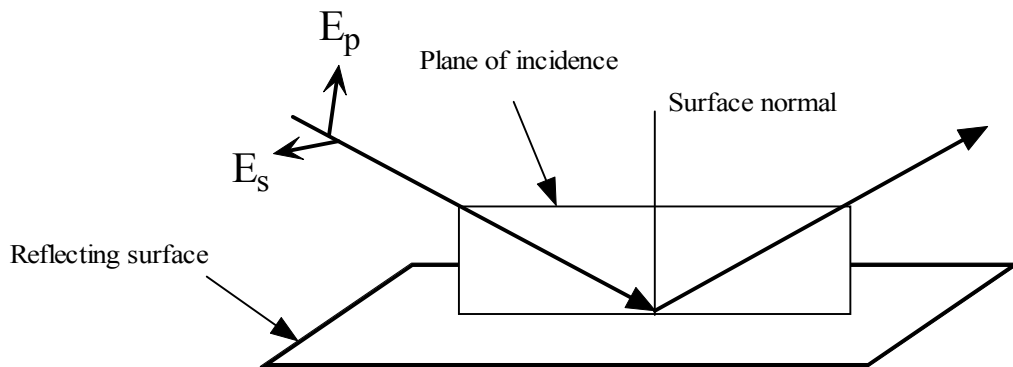


FIG.IV.6.1. Reflection of a light from a surface. The plane of incidence contains the incoming beam and the outgoing beam as well as the normal to the surface (after Tompkins [62])

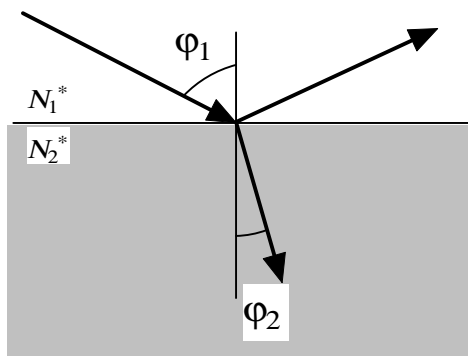


FIG.IV.6.2. Reflection and transmission of the light at a single interface [60].

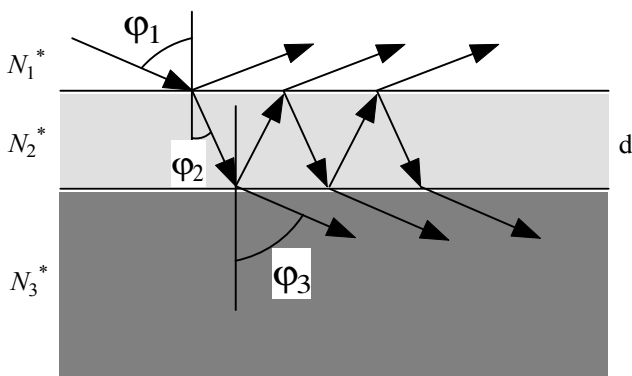


FIG.IV.6.3. Reflection and transmission with multiple interfaces [62].

The addition of thin infinite series of partial waves leads to the resultant wave. The total reflection coefficients are given by

$$R^p = \frac{r_{12}^p + r_{23}^p \exp(-j2\beta)}{1 + r_{12}^p r_{23}^p \exp(-j2\beta)}; \quad R^s = \frac{r_{12}^s + r_{23}^s \exp(-j2\beta)}{1 + r_{12}^s r_{23}^s \exp(-j2\beta)} \quad (\text{IV.6.2})$$

where the subscript “23” denotes that the Fresnel coefficient is for the interface between medium 2 and medium 3. β is the film phase thickness and is given by

$$\beta = 2\pi \left(\frac{d}{\lambda} \right) N_2^* \cos \varphi_2 \quad (\text{IV.6.3})$$

where d is the film thickness.

Referring to Fig.IV.6.1, the phase difference between the parallel component and perpendicular component of the incoming wave is denoted as ζ_1 . Further, the phase difference between the parallel component and perpendicular component of the outgoing wave is denoted as ζ_2 . The parameter Δ , called delta or often abbreviated as “Del” is defined as

$$\Delta = \zeta_1 - \zeta_2 \quad (\text{IV.6.4})$$

Del, then, is the change in phase difference that occurs upon reflection and its value can be from zero to 360° [p. 17 in ref. 62].

Without regard to phase, the amplitude of both perpendicular and parallel components may change upon reflection. $|R^p|$ and $|R^s|$ from equations (IV.6.2) are the ratios of the outgoing wave amplitude to the incoming wave amplitude for the parallel and perpendicular components, respectively. We define the quantity of Ψ in such manner that

$$\tan \Psi = \frac{|R^p|}{|R^s|} \quad (\text{IV.6.5})$$

Ψ then is the angle whose tangent is the ratio of the magnitudes of the total reflection coefficients. The value of Ψ can be between zero and 90° [p. 17 in ref. 62].

The complex quantity ρ is the complex ratio of the total reflection coefficients such that

$$\rho = \frac{R^p}{R^s} \quad (\text{IV.6.6})$$

The fundamental equation of ellipsometry then is

$$\begin{aligned} \rho &= \tan \Psi \exp(j\Delta) \\ \text{or} & \quad (\text{IV.6.7}) \\ \tan \Psi \exp(j\Delta) &= \frac{R^p}{R^s} \end{aligned}$$

where Δ and Ψ are the quantities, measured by an ellipsometer.

IV.7. Ferroelectric hysteresis characterization.

The Sawyer-Tower measuring technique is an established and accepted method for characterizing nonlinear devices and remains a standard against which all other measurement methods are compared. The Sawyer-Tower measuring system utilizes a sense capacitor in series with the device under test (DUT) and measures the voltage drop across the test sample as shown in Fig.IV.7.1 [63,64]. On the other hand, up-to-date commercially available devices (for example, RT6000S Radiant Technologies ferroelectric testing system) utilize another scheme which is called Virtual Ground System (VGS) for ferroelectric properties characterization. Unlike classical Sawyer-Tower scheme, in the virtual ground measuring system the sense capacitor is replaced by the measurement circuit shown in Fig.IV.7.2. In this configuration, the transimpedance amplifier maintains the RT6000S return terminal at a virtual ground potential. All of the charge that flows through the sample as a result of the

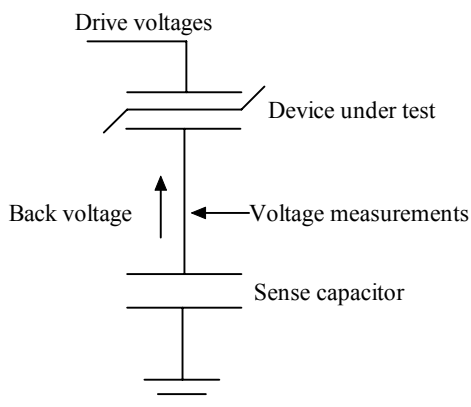


FIG.IV.7.1. Basic Sawyer-Tower test configuration [64].

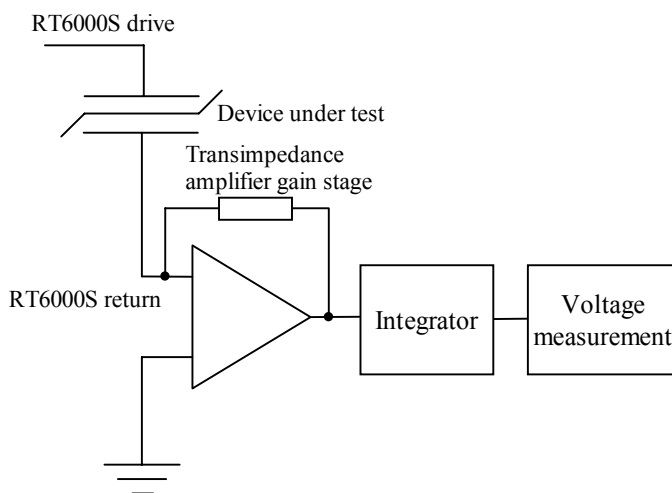


FIG.IV.7.2. RT6000S virtual ground mode measuring system [64].

applied drive voltage is collected by the integrator circuit. The voltage generated on the output of the integrator is then measured and translated into the test results that are displayed by RT6000S software.

In Fig. IV.7.3, the solid black waveform is the normal bipolar drive profile used to produce hysteresis polarization data; it traverses from zero volts to $+V_{\max}$, back through zero volts to $-V_{\max}$, then returns to zero. The dashed waveform (Fig.IV.7.3) is the same as the normal bipolar but with a 180° phase shift. The normal bipolar profile creates the right-hand portion of the P vs. V plot first followed by the left-hand portion. The “inverse” bipolar profile creates the left-hand portion first then the right.

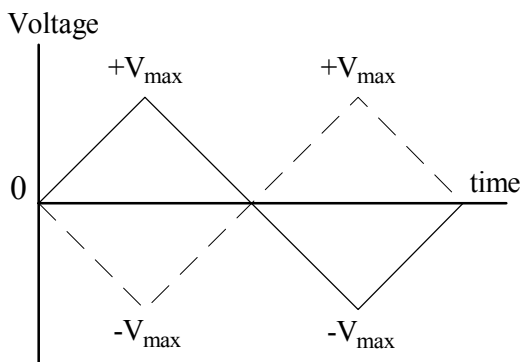


FIG.IV.7.3. Drive voltage profiles [64] (see text).

IV.8. Dielectric properties measurements.

Ferroelectric materials are mainly dielectrics. High dielectric constant (ϵ') and loss tangent ($\tan\delta$) are basic characteristics of these materials. For most applications the dielectric constant and loss tangent are important practical parameters. Suppose a parallel plate capacitor filled with a dielectric medium. When an alternating electric field E with an angular frequency ω is applied to this capacitor, an alternating current i flowing through the condenser plate is given by [p. 38 in ref. 8],

$$i = j\omega\epsilon^* C_0 E \quad (\text{IV.8.1})$$

where j is the imaginary operator, C_0 is the capacitance of the parallel plate condenser in absence of any medium, ω is the angular frequency and ϵ^* the complex permittivity. Because dielectric loss (including the leakage current) exists in dielectric materials, the dielectric constant must be written as a complex number:

$$\epsilon^*(\omega) = \epsilon'(\omega) - j\epsilon''(\omega) \quad (\text{IV.8.2})$$

where $\epsilon'(\omega)$ and $\epsilon''(\omega)$ are the real and the imaginary parts of dielectric constant, respectively. The latter represents the dielectric loss. Often, it is more convenient to use $\tan\delta$ (loss tangent) instead of ϵ'' :

$$\tan \delta = \frac{\epsilon''}{\epsilon'} \quad (\text{IV.8.3})$$

There is a number of techniques for frequency dependent dielectric properties characterization cited in literature. Brief review on the principles of dielectric measurements can be found in ref. 8. Up-to-date commercially available bridges cover the frequency range from 0.01 Hz to approximately 10 MHz. For direct measurements of dielectric constant and loss tangent in audio frequency range, Schering bridge is commonly utilized. Schering bridge is shown schematically in Fig. IV.8.1. Alternating voltage is applied to the bridge circuit, including sample, reference capacitor and resistance. The current through the sample is balanced by the adjustment variable capacitor and resistance in the opposite shoulder of the bridge. Accurate measurements of dielectric properties at frequencies higher than 10 MHz is problematic due to contribution of distributed capacity (p. 40 in ref. 8). Other methods such as resonant circuit, transmission line, waveguides or resonant cavity were developed for characterization of dielectric materials in different frequency ranges. The description of techniques can be found in standard textbooks.

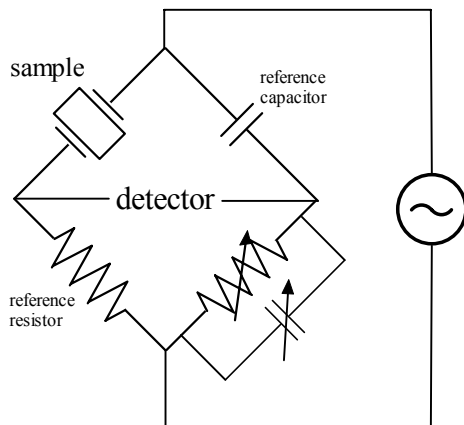


FIG.IV.8.1. Schering bridge.

IV.9. Leakage current measurements.

Leakage current is one of the factors limiting the applicability of ferroelectric thin films in memory devices. Therefore, leakage current measurement is a very important step heading toward the improvement of material performance. Voltage step, voltage ramp or

voltage pulse techniques are used [65]. Following Dietz and Waser [65], if any voltage signal is applied to a dielectric, the current response will be composed of a polarization contribution (arising from charges which are stored in the system) and a leakage contribution (composing charges which are carried from one electrode to another). In order to determine the leakage current of a dielectric thin film as a function of the applied voltage, J - V , either a voltage ramp technique or a voltage step technique are often employed. In the latter case, the correct procedure involves a sufficient charging time and an additional analysis of the discharging current after short-circuiting the sample. This leads to a separation of the polarization and the leakage contribution to the current. Recording the J - V characteristics often requires long measuring times, if the leakage currents are small. It is generally accepted that the voltage-step technique with sufficiently long charging and discharging times reveals the most accurate and unequivocal J - V data. A controversy, however, has been raised on the question of the error which is made by applying the (usually much faster) voltage-ramp technique to record the J - V characteristics [65]. Voltage pulse technique was developed purposely for testing the suitability of thin films for DRAM capacitors application. The voltage pulse technique allows simulation of real memory device operation (for details see ref. 65 and references therein).

IV.10. Determination of pyroelectric coefficient of ferroelectric materials.

Various techniques were developed in the last decades for pyroelectric coefficient measurement. Exhaustive review of methods of quantitative and qualitative characterization of pyroelectric properties of ferroelectric materials is given by Lang [66].

The most widely accepted method is based on the measurement of temperature dependent pyroelectric current (p. 328 in ref. 45). The pyroelectric coefficient is simply calculated using the equation:

$$p = \frac{I_p}{S \frac{dT}{dt}} \quad (\text{IV.10.1})$$

where

$$I_p = I \left(1 + \frac{R_M}{R_C} \right) \quad (\text{IV.10.2})$$

here t is time, S is the area of the capacitor, I is the measured current and R_M and R_C are the input resistance of the amplifier and the leakage resistance of the specimen, respectively. The circuit for direct measurement of the pyroelectric coefficient is shown in Fig.VI.10.1.

In the dynamic method (which is called by Lang (p.34 in ref. 66) Radiant Heating Method), the specimen is irradiated with a sinusoidally modulated heat flow and the pyroelectric current or voltage change are measured. A function generator operated laser diode or Peltier element are mainly used as heat sources to study the pyroelectric response at high and low frequencies, respectively. Although this method allows rather qualitative than quantitative characterization of the material property, it can be very useful for the estimation pyroelectric thin film properties and pyroelectric device performance. For a quantitative characterization of the pyroelectric properties using this technique, either calibration of heat source or precise measurements of sample temperature variation are required. The experimental set-up used in the present work for studying the pyroelectric properties of the thin films investigated will be described in Chapter VII.

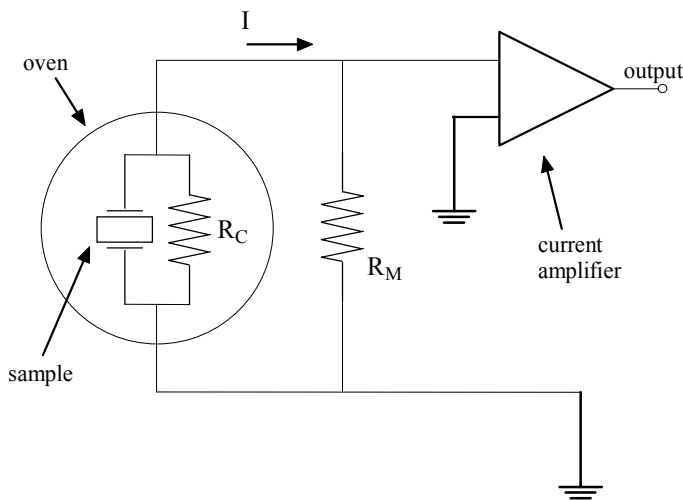


FIG.IV.10.1. Circuit for direct measurement of the pyroelectric coefficient [45].

IV.11. Measurements of piezoelectric characteristics of ferroelectric materials.

There are various standard techniques (dynamic and static) developed for the measurements of piezoelectric coefficients of bulk materials (p.53 in ref. 8). In the dynamic methods, the specimen is included into a transmission line circuit. The vibration of the specimen is induced by an applied weak AC signal at a frequency near the intrinsic resonance frequency of the specimen. The resonance and antiresonance frequencies of specimen are measured. These data are then used for the calculation of the piezoelectric constant of the specimen. In the static mode, an external force of a certain amplitude is applied to the specimen in a fixed direction. The charge accumulated on the sample surface due to the piezoelectric effect is equal to the electric displacement. Value of piezoelectric constant component corresponding to the chosen direction is straightforward to calculate using

(III.2.1). However, geometrical limitations and inadequate sensitivity make these methods not applicable for the characterization of the piezoelectric properties of thin films of submicron thickness. In fact, piezoelectric response (displacement) of such films can be from several angstroms to several nanometres and fundamentally different techniques must be utilized. The laser vibrometer technique has been found to be more appropriate for piezoelectric characterization of thin films. For example, a Doppler heterodyne interferometer was successfully used [67] for studying the piezoelectric properties of PZT thin films. The device

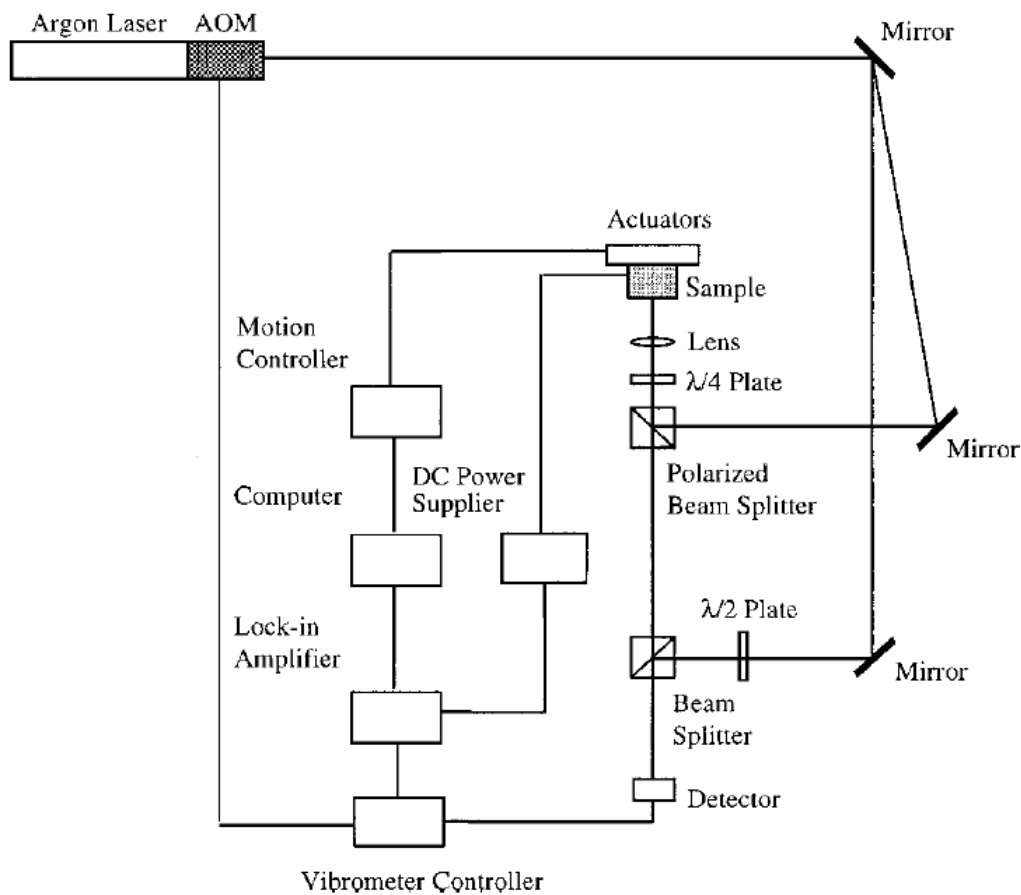


FIG.IV.11.1. Schematic drawing of the Doppler heterodyne interferometer [67].

exploits the Doppler shift effect. When a sinusoidal voltage is applied across the capacitor, a sinusoidal displacement

$$L = \Delta L \sin(\omega t) \quad (\text{IV.11.1})$$

is induced due to inverse piezoelectric effect. Here ΔL is the displacement amplitude (the equation is given for the first harmonic). The Doppler frequency shift, f_D , is given by the equation:

$$f_D = \frac{2v}{\lambda} \quad (\text{IV.11.2})$$

where v is the velocity of a moving surface and λ is the wave length of light reflected normal to the surface. The surface velocity and displacement are converted from interferometrically determined Doppler frequency shift. The Doppler heterodyne interferometer is illustrated schematically in Fig.IV.11.1 [67]. A 40 MHz acousto-optic modulator (AOM) produces two beams. One beam is focused at normal incidence on the sample surface and another one is used as the reference. The sample beam (reflected from the sample surface) and the reference beam are recombined in a beam splitter before incidence on a photodetector. The intensity of light arriving at the photodetector is expressed as [67]:

$$I = I_r + I_s + 2\sqrt{I_r I_s} \cos \left[2\pi \left(40\text{MHz} + \frac{2v}{\lambda} \right) t \right] \quad (\text{IV.11.3})$$

where I_r and I_p are the intensities of the reference beam and the sample beam, respectively [67]. Any out-of-plane velocity of the sample surface which relates to the surface displacement though

$$\Delta L = \frac{\Delta v}{\omega} \quad (\text{IV.11.4})$$

where Δv is the velocity amplitude, produces a corresponding frequency shift in the signal arriving at the photodetector. The signal from the photodetector is decoded using frequency modulation (FM) demodulator in the vibrometer controller (Polytec OFV 3001) and then measured with a digital lock-in amplifier.

V. Overview of the properties of lead-based perovskite-type ferroelectric thin films: microstructural and compositional aspects.

The present chapter gives an overview of the electrophysical properties of lead-based ferroelectric thin films of the perovskite structure. The experimental results reported by other research groups are discussed with emphasis on microstructural and compositional aspects. This section is also aimed at the analysis of specific properties of polycrystalline ferroelectric thin films (not found in bulk materials) such as preferred orientation, development of stresses due to thermal expansion mismatch between film and substrate materials, as well as thickness dependence of the dielectric properties.

V.1. Optical properties.

The analysis of publications devoted to the optical characterization of ferroelectric thin films shows that the topic is of interest from applied and fundamental points of view. The available literature mainly deals with dimensional effects in the films i.e. dispersion of the, optical properties vs. thickness and film-electrode interaction. Some results of ellipsometric and LIMM (Laser Intensity Modulation Method) investigations in PZT thin films can be found in recent works by Glinchuk *et al.* [68] and Deineka *et al.*[69]. Wood *et al.* [70] prepared PT, PZT and PMN films and characterised their optical properties with respect to film thickness and type of substrate. It must be noted that authors could not attain the complete pyrochlore-to-perovskite transformation probably because of inadequate processing conditions and the residual pyrochlore was detected for the majority of the specimens investigated. The results of the refractive coefficients measurements obtained by Wood *et al.* [70] are collected in Table V.1.1. Based on extensive experimental data, these authors have demonstrated that the optical properties of the films are sensitive to both substrate material and fabrication conditions (in particular, annealing temperature). They also have shown that the presence of second phase can cause some change in the value of the refractive index. Wood *et al.* [70] report that their films are, in general, characterized with lower values of the refractive indices with respect to those of bulk materials. At the same time, the results are

discussed with the emphasis on the waveguiding properties of the films and related applications which are out of scope of the present work. Moreover, characterization of the films fabricated utilizing sapphire and single crystalline SrTiO₃ as the substrate materials is, first of all, interesting from the fundamental standpoint. Silicon substrates are required for the correct discussion of the applicability of the films in up-to-date integrated devices.

It must be pointed out that a systematic investigation of lanthanide elements doping effects on the optical properties of lead based ferroelectric films is still lacking which is surprising since firstly, rare-earth elements doping of ferroelectrics is frequently used to tune their properties, and secondly RE modified materials are of great interest from the point of view of photonic applications [71]. Doping effects on the optical properties of lead-based perovskites have been only marginally addressed. Chang and Desu [72] investigated the dependence of refractive index of La and Nd doped sol-gel fabricated PZT 50/50 thin films

Table V.1.1. Optical properties of PT, PZT and PMN thin films as function of thickness and substrate material (after Wood *et al.* [70]).

Composition	Substrate	d , nm	Refractive index ($\lambda=632.8$ nm)
PbTiO ₃	Sapphire	130	2.57
		260	2.60
		520	2.55
PZT 60/40	Sapphire	630	2.25
		830	2.41
PZT 53/47	SrTiO ₃ (100)	280	2.48
	SrTiO ₃ (110)	280	2.50
	SrTiO ₃ (111)	280	2.49
	SrTiO ₃ (100)	610	2.50
PMN	Sapphire	320	2.33
		260	2.45
		260	2.48
		330	2.28
	SrTiO ₃ (110)	380	2.46

on the concentration of doping elements. It was shown that doping with La and Nd up to 6 mol % results in a small increase in the index of refraction (within 5%). The effect was attributed to changing in the density of the films (decreased porosity), and the nature of dopants was not taken into account. In the present work, the optical properties of sol-gel deposited PbTiO₃ thin films as function of the doping level and atomic number of lanthanide elements are reported.

V.2. Microstructure and crystallization kinetics.

The microstructure and phase composition of ferroelectric thin films are known to be strongly affected by the choice of fabrication route, type of substrate material and deposition parameters. Epitaxial, preferentially oriented or randomly crystallized films can be obtained depending on specific processing conditions. The fabrication of epitaxial films requires single crystal substrates with lattice parameters well matched with those of the film material. On the other hand, epitaxial growth can be achieved mainly by *in-situ* deposition methods, such as PLD or OMCVD. For example, Lee *et al.* [73] reported on successful deposition of PZT thin film with composition near the morphotropic phase boundary (MPB), i.e. PZT 52/48 by means of pulsed laser deposition on MgO (100) crystal. Braun *et al.* [74] obtained epitaxial PZT films of different compositions on (1 $\bar{1}$ 02) oriented sapphire. The sol-gel method allows the fabrication of textured, or randomly oriented films. Lian and Sottos [67] obtained high

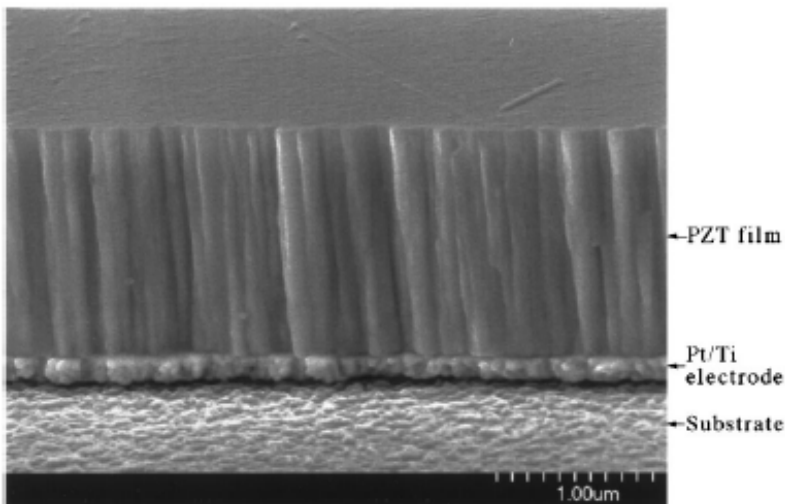


FIG.V.2.1. SEM cross-section of sol-gel fabricated PZT 52/48 (MPB composition) thin film (after Lian and Sottos [67]).

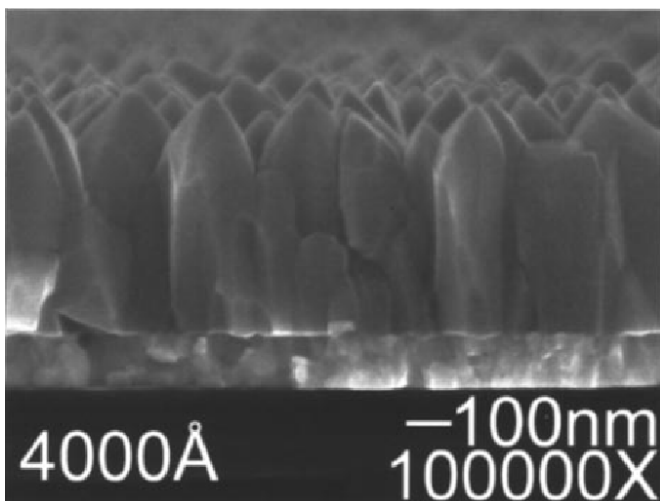


FIG.V.2.2. SEM cross-section of MOCVD processed tetragonal PZT 35/65 thin film (Ir bottom electrode) (after Kelman *et al.* [75]).

quality (111) and (100) preferentially oriented PZT 52/48 thin films by a sol-gel method on platinumized silicon substrates. Such films usually have columnar morphology (as shown in Fig. V.2.1) and lateral grain size less than 100 nm. Similar columnar morphology was reported by Kelman *et al.* [75] for MOCVD derived tetragonal PZT 35/65 thin film (Fig.V.2.2). An example of coarse grain formation is shown in Fig.V.2.3 [76]. It seems, that the choice of a given stoichiometry even within one system of solid solutions ($\text{Pb}(\text{Zr}_x\text{Ti}_{1-x})\text{O}_3$ or PZT) can lead to completely different grain morphology, phase composition and textures of sol-gel processed films.

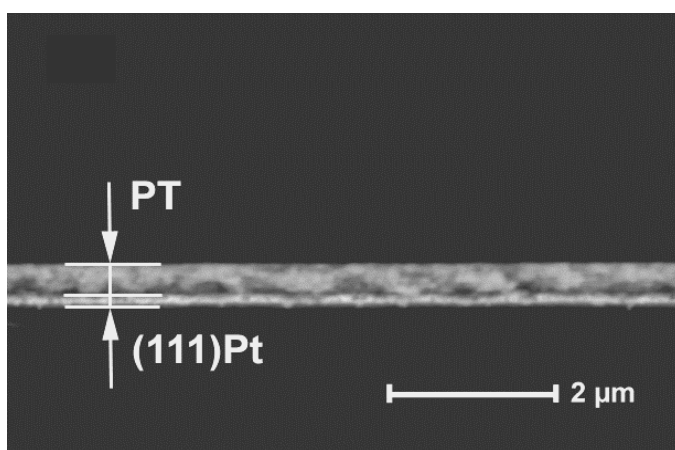


FIG.V.2.3. SEM cross-section of sol-gel fabricated lead titanate thin film [76].

The morphology of thin films is known to depend on deposition parameters. Especially, annealing temperature and duration were found to be critical and must be taken into account in the prediction the final microstructure. In our previous work the effects of annealing conditions on microstructure of sol-gel PZFNT ($\text{Pb}_{1.1}(\text{Zr}_{0.58}\text{Fe}_{0.2}\text{Nb}_{0.2}\text{Ti}_{0.2})\text{O}_3$) thin films have been reported [77]. Based on the results of SEM and XRD characterization it was shown that not only the microstructure but also the phase composition of the films are sensitive to annealing conditions. Annealing at 700°C for 20 min resulted in fine crystallized perovskite phase which was shown to coexist with residual pyrochlore. At higher temperature (750°C) only perovskite phase was detected. When the annealing time was increased to 30 min pyrochlore phase formation due to PbO volatility was observed. Thus, appropriate annealing parameters (temperature and duration) lie in a narrow region and must be carefully optimized. In sol-gel, the desired thickness of the film is usually achieved by multiple deposition sequences. The thermal history of each layer is critical for the resultant microstructure of the film. It was reported [78] that using a seed layer (the first layer is annealed before deposition of the subsequent layers) can significantly affect the morphology

of the film. It was concluded that the presence of a seed layer reduces the nucleation energy of perovskite phase crystallization and promotes the formation of uniform microstructures [78].

The kinetics of thin film crystallization was addressed by many authors. The theoretical background, including various models of thin film formation can be found in standard textbooks [79]. In the particular case of perovskite crystallization, nucleation and growth from an amorphous or pyrochlore phase is supposed to be diffusion controlled. If so, the crystallization and growth kinetics of perovskite phase particles should obey the Avrami-type parabolic law [80]:

$$x(t) = 1 - \exp(-Kt^n) \quad (\text{V.2.1})$$

where $x(t)$ is the crystallized fraction at the time t , K is a temperature dependent constant, and n is the rate exponent. Values of n were found to be in the range from 0.5 to 1.5 depending on the annealing temperature for 5 mol % of Nb substituted thin films [80]. The activation energy of crystallization for these films was found to be 169 kJ/mol which lies in the range of values determined by other authors for crystallization of PZT.

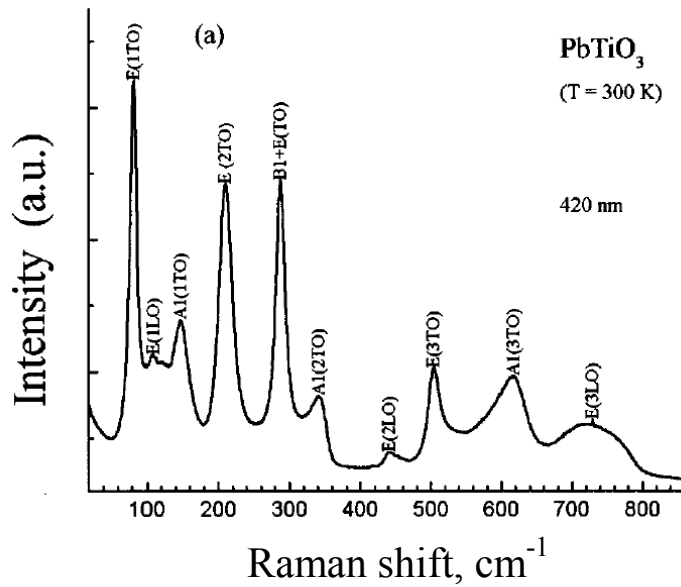
V.3. Raman scattering.

It is appropriate to start the section with a general description of Raman spectra of lead titanate. Investigations of Raman scattering from PbTiO_3 single crystals, powders and thin films were undertaken by many research groups [81-90]. Systematic studying of Raman scattering from lead titanate was first reported by Burns and Scott [81,82]. In the paraelectric phase (above Curie temperature) lead titanate belongs to O_h^1 (Pm3m) space group and there are 12 optical phonons exist. These phonons transforms as the $3T_{1u}+T_{2u}$ irreducible representation of the point group. Triply degenerate T_{2u} mode is IR- or Raman-inactive; the three T_{1u} modes are IR-active. When lead titanate undergoes the paraelectric to ferroelectric phase transition, O_h^1 (Pm3m) space group transforms to the less symmetric tetragonal C_{4v}^1 (P4mm) space group. This reduction of symmetry results in the splitting of three T_{1u} into two modes transforming as A_1+E irreducible presentation of C_{4v} space group. Both A_1 and E are IR- and Raman active [81,82]. In the present work we will use the notation of Burns and Scott [81,82] for Raman modes. The list of Raman-active modes of lead titanate is given in Table V.3.1 [84].

Table V.3.1. Raman active modes of PbTiO_3 lattice below Curie point [84].

$A_1(3\text{TO})$	$A_1(3\text{LO})$	$E(3\text{TO})$	$E(3\text{LO})$
$A_1(2\text{TO})$	$A_1(2\text{LO})$	$E(2\text{TO})$	$E(2\text{LO})$
$A_1(1\text{TO})$	$A_1(1\text{LO})$	$E(1\text{TO})$	$E(1\text{LO})$

TO's are the transverse modes with the polarization perpendicular to the wave vector \mathbf{k} and LO's are longitudinal optical modes with the polarization parallel to \mathbf{k} . The two lowest frequency modes $E_1(1\text{TO})$ and $A_1(1\text{LO})$ are called "soft modes". A Raman spectrum measured for sol-gel deposited lead titanate thin films is exemplified in Fig.V.3.1 [90]. B_1+E is the so-called silent mode. All Raman bands reported earlier for bulk materials are present in the spectrum of the thin film. However, some features peculiar to thin films are found. First, the Raman spectra obtained for thin films demonstrate noticeable line broadening in comparison to single crystal; second, the Raman lines are shifted to lower frequencies [84,85]. These

**FIG.V.3.1.** Raman spectra of sol-gel deposited lead titanate thin films [90].

observations were explained in terms of local disordering of the system and development of stress during film fabrication [84-86,89]. The frequencies of the phonon modes in a PbTiO_3 thin film and PbTiO_3 single crystal are compared in Table V.3.2 (ref. 84 and references therein). Furthermore, it has been reported that the frequency shift of the Raman modes to lower values (of particular interest is the $E(1\text{TO})$ soft mode because it is responsible for the ferroelectric to paraelectric phase transition) is caused by small crystallite sizes [83,87] or doping [88], and is related to lattice tetragonality reduction (induced by the small crystallite sizes of the film and/or stresses).

Table V.3.2. Frequencies of the phonon modes in a PbTiO₃ thin films and crystals [84].

Mode	Frequency (cm ⁻¹)		
	Single crystal		Thin film
	pressure ~0 GPa	pressure~1.4 GPa	
<i>E</i> (1TO)	89	80	80
<i>A</i> ₁ (1TO)	127	117	116
<i>E</i> (1LO)	128		
<i>A</i> ₁ (1LO)	215		
<i>E</i> (2TO)	221	200	206
<i>B</i> ₁ + <i>E</i>	290	290	287
<i>A</i> ₁ (2TO)	364	340	341
<i>E</i> (2LO)+ <i>A</i> ₁ (2LO)	445		443
<i>A</i> ₁ (3TO)	508	508	501
<i>E</i> (3LO)	717		~720
<i>A</i> ₁ (3LO)	797		

V.4. Dielectric properties.

The dielectric properties of thin films can be affected by a number of variables including processing conditions, substrate materials, phase purity and preferential orientation. Furthermore, the size effect, i.e. dependence of the dielectric properties on the film thickness is a specific feature of ferroelectric thin film.

It is quite common for dielectric properties of ferroelectric thin films to be treated from the point of view of contribution of electrode-film interface(s) into small-signal response from the film. A number of experimental results published show that the dielectric constant of the films decreases with film thickness. Paek *et al.* [91] reported some degradation of dielectric and leakage properties of BST thin films of thickness ranging from 50 to 300 nm deposited on platinum electrode. By means of scanning electron microscopy and high resolution transmission electron microscopy (HRTEM) very thin layer (of thickness between 9.5 and 11 nm) with crystallinity different from that of the bulk of the film was revealed. Decreasing of the dielectric constant was also reported by Hwang *et al.* [92] for BST thin films deposited on platinum electrode. Yet, the dielectric constant of BST films of the same composition, fabricated on IrO₂ bottom electrode was found to be thickness independent in the film thickness range investigated (from 30 to 100 nm). Degradation of the dielectric properties with decreasing film thickness is also observed by Amanuma *et al.* [93], Sakashita *et al.* [94] and Es-Souni *et al.* [95]. On the other hand, Shin *et al.* [96] deny thickness dependent variation in the dielectric constant of PZT films in the thickness range from 100 to 250 nm processed via sol-gel method on platinized silicon substrate. Thermal expansion

mismatch, chemical interaction between materials of the film and bottom electrode lead to the formation of so-called “dead layer”. This layer has significantly lower dielectric constant and contains high concentration of defects which, in turn, serve as an effective trap centres for mobile charges and domain walls. The existence of such layer affects the dielectric properties of the films especially for very thin films (thinner than 200 nm). It is thought that the formation of dead layers occurs rather at film-bottom electrode interface than film-top

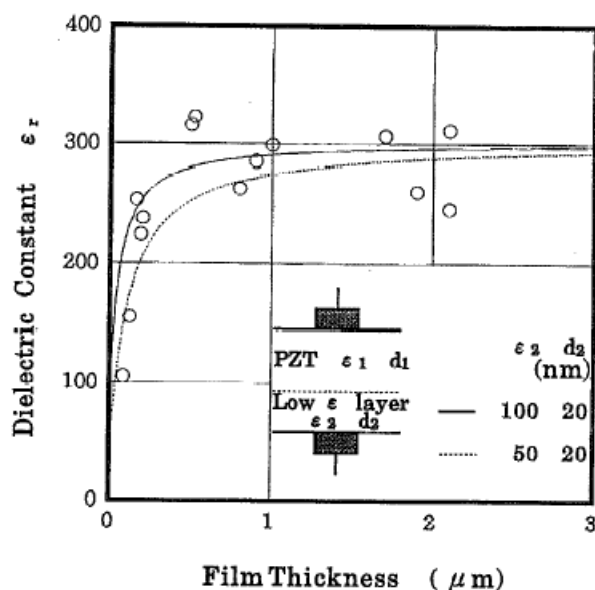


FIG.V.4.1. Relationship between film thickness and the relative dielectric constant [94]. Experimental results are represented with circles. Solid and broken lines are calculated from a model which assumes that a low dielectric constant layer exists in series with the PZT layer.

electrode interface since the former is exposed to high temperature during film fabrication. An example of thickness dependent dielectric constant of PZT film, produced by OMCVD on platinumized (100) MgO substrates is shown in Fig.V.4.1 [94]. The structure of the specimen where low ϵ' layer exists in series with bulk part of the specimen is shown schematically on the inset. These authors also show that microstructure (grain size) and stress state are also thickness dependent (exhaustive papers on the stress state of lead-based perovskite thin films are published by Spierings *et al.* [97] and Sengupta *et al.* [98]). The survey of literature reveals that degradation of dielectric properties with film thickness is rather complex. Authors in [94] suggest 5 possible mechanisms, viz. i) nonstoichiometric phase formation near film-electrode interface; ii) chemical reaction with platinum electrode; iii) a space-charge layer; iv) stress and v) the size effect. Yet, Auger electron spectroscopy (AES) depth profiling revealed rather uniform element distribution of the elements through film thickness. At the same time, while the results of dielectric and ferroelectric characterization confirm the existence of low dielectric constant layer in series with bulk of the film, no interaction or interdiffusion among the PZT film, platinum electrode and MgO substrate were evidenced by means of AES. Secondary-ion mass spectroscopy (SIMS) also shows similar results. As suggested by Hwang

et al. [92] for BST thin films, dielectric constant of the film can decrease with film thickness even without any interfacial low dielectric constant layer when metal electrodes such as Pt are used. This is due to the intrinsic low dielectric constant of few surface layers due to the termination of the chemical bonds at the electrode interface and nonpenetration of the ferroelectric polarization into the metal electrodes. It seems that interfacial layer formation mechanisms are strongly dependent on method of film fabrication, deposition parameters, film composition and type of substrate material. Chung *et al.* [99] analyzed PZT thin films deposited by OMCVD method. TEM, AES, EDS (energy dispersion spectroscopy) and XRD analysis revealed that: i) Pb-deficient interfacial layer of 25 nm thickness exists near the bottom electrode; ii) detrimental processes (Ti out-diffusion into the Pt layer, the oxidation of Ti by the in-diffused oxygen, and the formation of Ti-silicide by the reaction between the SiO₂ and Ti layers) take place in Pt/Ti/SiO₂/Si substrates during film fabrication. It is important to note that such processes occur at temperatures as low as 470°C. However results of dielectric and ferroelectric properties were not presented by these authors [99].

Usual thin film capacitor consist in a dielectric layer and a metallization produced by various methods. Along with bulk and interface parts of the thin film dielectric capacitor, electrode properties contribute to the measured frequency dependent dielectric properties. Fig. V.4.2 shows a simplified equivalent circuit of a ferroelectric thin film capacitor. The thin film can be represented as a capacitance C_f connected in parallel with a resistance R_f . Series resistance R_{el} is formed by electrode material. This resistance causes an abrupt drop of the measured value of the dielectric constant at frequencies of several MHz and hence constitutes a limitation for dielectric measurements at higher frequencies. The effect is not attributed to real relaxation process since in displacive-type ferroelectrics (BaTiO₃, PbTiO₃, PZT) frequency dispersion is evident in frequencies as high as 10⁸-10⁹ Hz [100].

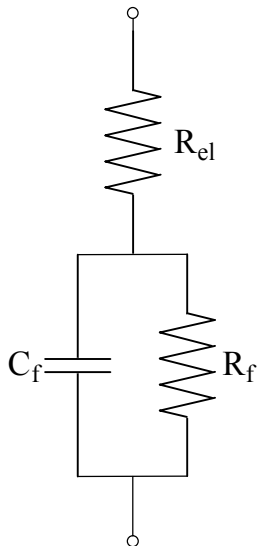


FIG.V.4.2. Simplified equivalent circuit of thin film specimen.

A characteristic feature of ferroelectric materials is the field dependence of capacitance (or dielectric constant). Measurement of dielectric properties of the material under an applied DC bias, higher

than the coercive field is a widely used experimental technique since it allows the estimation of the contribution of domain structure to the dielectric constant. The dielectric constant is being measured with sinusoidal AC voltage within the range of the linearity, i.e. the amplitude of the AC signal is much smaller than the coercive voltage. Room temperature C - V characteristic (capacitance and voltage are recalculated for the convenience into the real part of the dielectric constant and the electric field using the equation for plane capacitor) is exemplified in Fig. V.4.3 for a lead titanate thin film, fabricated by sol-gel method (for details see Chapter VII). The directions of DC bias sweep are indicated by arrows. In the vicinity of coercive field the value of capacitance (or dielectric constant) has a high value due to the switching of ferroelectric domains. This occurs due to: i) during switching a very small change in the applied electric field results in a very large change in the ferroelectric polarization, and ii) the highest concentration of domain walls is achieved in the vicinity of $E=E_c$. The hysteresis (butterfly shape) of C - V (or ϵ' - E) is peculiar to ferroelectric materials. Besides, one can note that ϵ' - E curve can be non-symmetrical with respect to both ϵ' and E axes, and this can give valuable information about trapped charges. These features of the ϵ' - E curves will be the topic of original discussion.

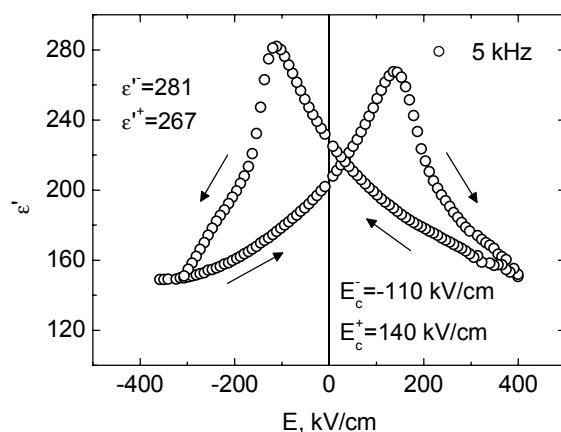


FIG.V.4.3. ϵ' - E characteristic of 8 mol % of Sm doped PbTiO_3 thin film. The given values of E_c^- , ϵ'^- , E_c^+ and ϵ'^+ show the position of maxima for negative and positive branches of the plot.

Voltage dependent dielectric properties of ferroelectric films were extensively investigated by different researchers [101-103]. First attempt to analyze quantitatively ϵ' - E characteristics of ferroelectric capacitor was undertaken by Brennan [101]. The model suggested is based on the assumption that ferroelectric C - V characteristic is affected by space-charges near film-electrode interfaces. It is proposed that the thickness of depleted layer near film-electrode interface is voltage dependent and that the depleted region possesses lower dielectric constant as to compare to the interior parts of the film. Specific shape of C - V reflects the contribution of depleted layer into small signal response. However, the model

needs to be extended to take into account asymmetrical nature of $C-V$ characteristics due to imprint and built-in field (will be discussed later), obtained for real metal-ferroelectric-metal capacitors (Fig.V.4.3). Difference in bottom electrode-film and top electrode-film interfaces due to different thermal histories is also not taken into account. Chai *et al.* [102] developed domain-related model for $C-V$ characteristics of the films. 1, 3 and 5 mol % of Nb doped PZT 50/50 thin films were investigated. Specimens were prepared on platinized silicon substrates using sol-gel method. Asymmetries of $C-V$ characteristics were attributed to correlation between ferroelectric properties of the films and dopant-ion induced local-field variation through the depth of the capacitors [102]. Vorotilov *et al.* [103] investigated sol-gel deposited PZT thin films deposited on platinized silicon wafer. As in the case exemplified in Fig. V.4.3, strong shift along field axis and non-symmetry of $C-V$ curve with respect to capacitance axis were observed. It was suggested that disturbed layer near bottom electrode may screen effectively external bias field causing asymmetrical nature of $C-V$ curves.

V.5. Ferroelectric properties.

Ferroelectric properties of the films are also known to be determined by method of deposition, microstructure and choice of electrode material. The best ferroelectric properties (high remnant polarization and low coercive field) were found for epitaxial films. Example of

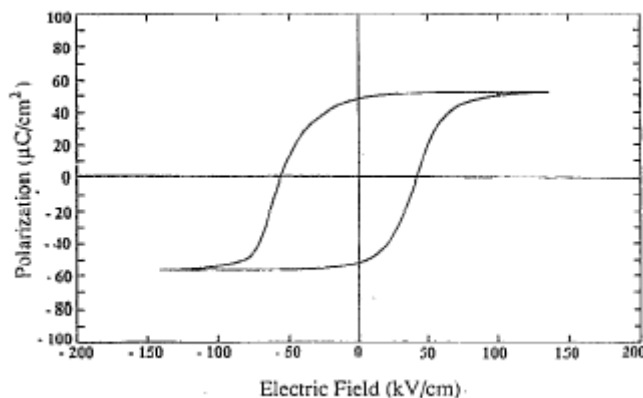


FIG.V.5.1. Field-polarization hysteresis loop of epitaxial PZT thin film, deposited by pulsed laser ablation [73].

ferroelectric hysteresis loop of PZT film, deposited on MgO substrate by PLD is presented in Fig. V.5.1 [73] where high remnant polarization can be seen. Polycrystalline films usually show somewhat lower ferroelectric properties. Fig.I.1.3(a) exemplifies the hysteresis loop of sol-gel fabricated film. Remnant polarization and coercive field were found to be $15 \mu\text{C}/\text{cm}^2$ and $58 \text{ kV}/\text{cm}$, respectively [10]. Influence of fabrication parameters on ferroelectric properties of polycrystalline ferroelectric thin films has been investigated by many research groups. Es-Souni *et al.* [80] discussed ferroelectric properties of Nb doped PZT thin films in

terms of microstructure and preferentially oriented state. Better results (higher value of remnant polarization) were reported for (111) preferentially oriented samples. It must be stressed here that correlation between microstructure and ferroelectric properties is still an object of controversy. Lian and Sottos [67] compared (100) and (111) preferentially oriented films. The former revealed noticeably higher remnant polarization. Whether the film is randomly crystallized or preferentially oriented is determined by processing condition and doping (will be discussed in more details in the following). It is also suggested that ferroelectric properties strongly correlate with type of sol-gel route. Kwon *et al.* [38] prepared PZT thin films using Acetate-, 2-methoxyethoxide-, and 2-ethylhexanoate-based precursor

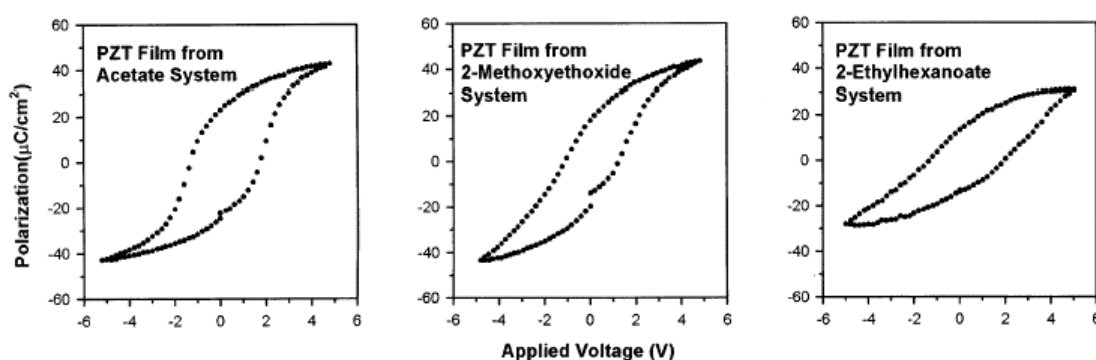


FIG.V.5.2. Effect of sol-gel precursor on ferroelectric properties of PZT thin films [38].

solutions. Dependence of ferroelectric properties on sol-gel chemistry was revealed. Fig.V.5.2 exemplifies P - V characteristics, obtained for the films prepared from different precursor solutions [38]. Well developed and saturated hysteresis loops were acquired for acetate- and 2-methoxyethoxide-based films (although, value of remnant polarization is noticeable smaller than that found for epitaxial PZT film [73]). Poorly developed P - V curves were obtained for the films deposited using 2-ethylhexanoate-based precursor.

Algueró *et al.* [104] discussed ferroelectric properties of lanthanum doped PbTiO_3 thin films deposited by sol-gel method on silicon substrates. Microstructure and phase content were found to be dependent on excess PbO added to the sol to compensate lead volatility during annealing. They suggest that ferroelectric properties of their specimens are chiefly determined by the grain size of the films, which, they claim, is dependent of PbO excess, viz. with increasing PbO excess from 10 to 20 mol %, the grain size decreases from approximately 1 μm to 100 nm.

Furthermore, doping by various impurities can affect ferroelectric hysteresis of the films. Modification of ceramics by donor or acceptor elements to tune the properties for specific application is widely used in industry (see ref. 8). The effects of doping on

ferroelectric properties of thin films are also reported for lead based perovskite thin films of different compositions (see next paragraph for more details). As an example Fig.V.5.3 represents hysteresis loops obtained by Mah *et al.* [105] for La doped $(\text{Pb}_{1-x}\text{La}_x)(\text{Zr}_{0.5}\text{Ti}_{0.5})\text{O}_3$ films. Incorporation of La into the perovskite lattice caused the reduction of ferroelectric characteristics (P_r and E_c). Similar trend (the reduction of ferroelectric characteristics with increasing La content) was reported by Es-Souni *et al.* [106] and Kurchania and Milne [107] for PLZT films derived by sol-gel technique. Dobal *et al.* [108] measured ferroelectric hysteresis loops of Ce doped PLT films. It is reported that remnant and spontaneous polarization are generally increases with Ce content. The same behaviour was observed by Chang and Desu [72] and Matsuzaki and Funakubo [109] for La doped PZT and Nb doped PT thin films, respectively. Teowee *et al.* [110] reported that remnant polarization of La doped PZT 65/35 thin films shows a maximum in the vicinity of 4 mol % of La. In the other words, ferroelectricity in thin films is far more complex than in bulk ceramics and is still an object of intensive research.

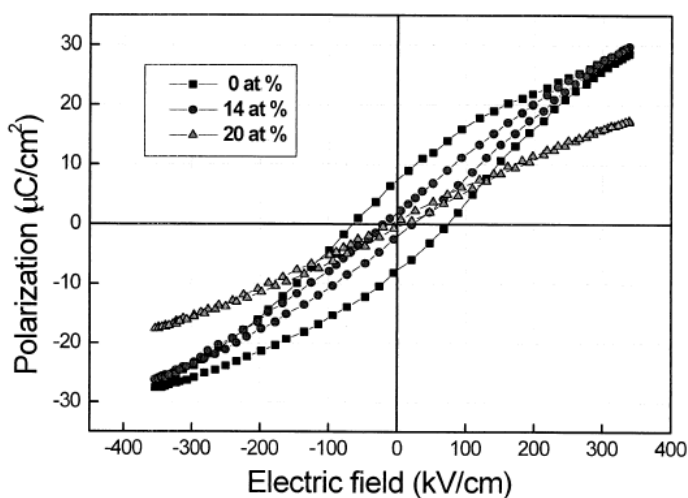


FIG.V.5.3. Hysteresis loops of PLZT thin films modified with various amounts of La [105].

Finally, dependence of ferroelectric characteristics of polycrystalline films on the nature of bottom electrode was investigated by many research groups. The use of conductive oxide instead of metallic platinum or gold electrodes can cause some improvement in ferroelectric properties and fatigue resistance of ferroelectric thin films. In particular, fabrication and characterization of BaTiO_3 and PZT thin films upon lanthanum nickel oxide (LNO) electrode were reported [31, 111-114]. Fig. V.5.4 exemplifies ferroelectric hysteresis loops of PZT thin films deposited on stainless steel (a), titanium (b) and nickel (c) substrates

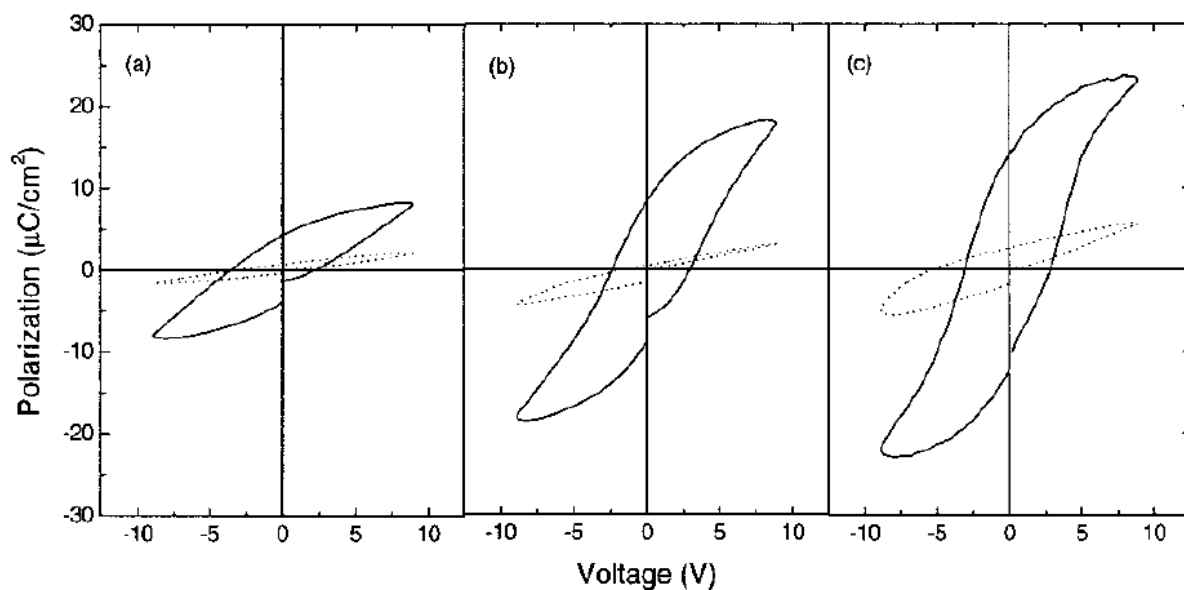


FIG.V.5.4. Hysteresis loop of PZT thin films on (a) stainless steel, (b) titanium and (c) nickel substrates annealed at 600°C, measured at 180 kV/cm. Solid lines are for the PZT films fabricated incorporating LNO layers and dotted lines are for the PZT without LNO layers [111].

with and without lanthanum nickel oxide buffer layers [111]. The results unambiguously demonstrate that good ferroelectric response can be achieved for the films deposited on LNO buffer layer. Contrary, film deposited on bare metallic substrate revealed significant degradation of ferroelectric properties due to chemical interaction of the films with the substrate material.

V.6. Curie phase transition temperature.

Similar to bulk ceramics or crystals, the dependence of the dielectric constant of ferroelectric thin films shows anomaly in the vicinity of Curie transition temperature. However some specific features of the behaviour of ferroelectric films near ferroelectric-to-paraelectric phase transition were reported. Fig. V.6.1 shows the temperature dependent dielectric constant of $\text{Ba}_{0.7}\text{Sr}_{0.3}\text{TiO}_3$ thin film in comparison to that of bulk ceramics of the same composition (after Shaw *et al.* [115]). As can be seen, the ceramic specimen shows a sharp peak in the vicinity of 300K, which is attributed to ferroelectric-to-paraelectric phase transition, whereas the thin film demonstrates a very broad transition. Furthermore, a close look at the figure reveals that the BST film undergoes ferroelectric-to-paraelectric phase transition at remarkably lower temperature. Shaw *et al.* [115] explain the phenomenon from the point of view of stress development during film fabrication. Moreover, as reported in

recent work of Chattopadhyay *et al.* [116] for epitaxial BaTiO₃ thin film, Curie temperature decreases smoothly with decreasing film thickness. Additionally, broadening of $\epsilon'(T)$ characteristics was observed for thinner films. As in the former case, the results are treated in terms of stress state development effect. In bulk barium titanate and strontium titanate compressive stress dependent dielectric properties and Curie phase transition temperature were systematically investigated by Samara [117]. It was observed that Curie temperature decreases linearly with increasing pressure with the rate being in the range from -4.6 to -5.9 °C/kbar. Dausch and Haertling [118] claimed that lead lanthanum zirconate titanate thin films undergo ferroelectric-to-paraelectric phase transition at higher temperatures compared to ceramics of the same compositions. The results obtained were explained from the point of view of stress development during cooling. Rossetti *et al.* [119] calculated possible shift of Curie transition temperature in epitaxial lead titanate thin film. It was predicted that two-dimensional compressive stress oriented orthogonal to the *c*-axis increases Curie temperature, while hydrostatic (three-dimensional) compressive stress reduces Curie temperature.

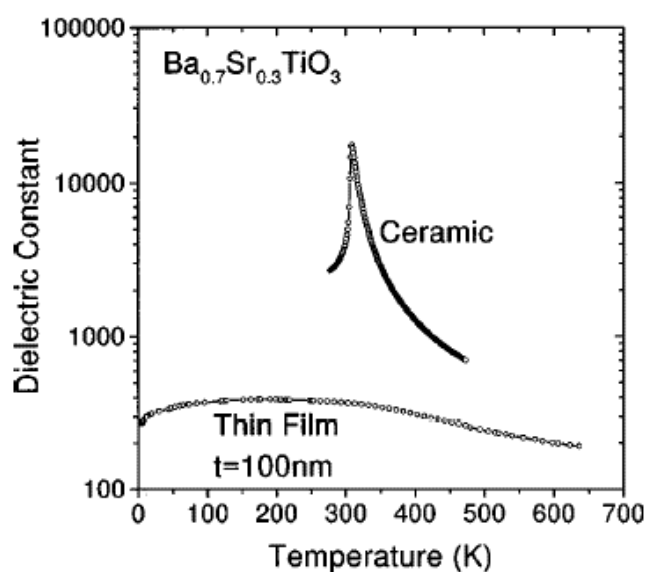


FIG.V.6.1. Variation of the dielectric constant of Ba_{0.7}Sr_{0.3}TiO₃ bulk ceramics and a film as a function of temperature [115].

The grain size is an additional parameter which determines deviation of Curie temperature from crystal value. Okazaki and Nagata [120] investigated the dielectric properties of PLZT ceramics of composition (Pb_{0.92}La_{0.08})(Zr_{0.65}Ti_{0.35})_{0.98}O₃. It was shown that with the decreasing grain size from 4 μm to 1.5 μm, the Curie transition temperature increases from approximately 120 to 140 °C. This effect was explained taking into account surface layer of the grains. This layer possesses specific properties which differ from those of interior part of grain. Following Okazaki and Nagata [120], in particles less than 5 μm in size, the effects of the surface layer in which the ferroelectric polarization is locked-in by the space-

charge layer become increasingly important. If the locked-in ferroelectric polarization inside each domain persists to temperature, far beyond the usual Curie point, the ferroelectric-paraelectric transition temperature can be expected to increase with decreasing grain size, because, when the grain size decreases, the surface area of the space-charge layer increases, and both the space-charge field and the locked in ferroelectric polarization increase simultaneously. This mechanism explains the grain-size dependence of the Curie point. On the other hand, Curie transition temperature of ferroelectric thin films and nano-sized powders shows completely opposite behaviour. Chattopadhyay *et al.* [121] studied Curie phase transition in nanocrystalline PbTiO_3 powder. They revealed a decrease in phase transition temperature with decreasing particle size. The most pronounced effect was found for particles size less than 100 nm. This behaviour was attributed to size induced structural distortion, viz. lattice tetragonality decreases with decreasing particle size.

To recapitulate, shift of the Curie phase transition temperature of ferroelectric thin films arises from the superposition of two effects, which must be taken into account. One is stress development and another one is related to grain size. Contribution of these effects into the measured value of Curie temperature depends on thin film microstructure, thermal expansion properties of substrate and thin film and thermal history of the sample.

V.7. Doping effects.

In order to tune the properties of interest, the effect of doping is under investigation by many research groups. In general, the term “doping” implies either that some ions, whose chemical valence is different from those of the original ions in the lattice [pp. 133-140 in ref. 8], or some compounds with a chemical formula $\text{A}^+\text{B}^{5+}\text{O}_3^{2-}$ or $\text{A}^{3+}\text{B}^{3+}\text{O}_3^{2+}$, are added during materials processing. Depending on the type of additive one can distinguish between “soft” and “hard” dopants (effect of isovalent elements doping is out of scope of the present work). Ions for soft doping include La^{3+} , Nd^{3+} , and other rare earth, Sb^{3+} , Bi^{3+} , Th^{4+} , Nb^{5+} , Sb^{5+} , W^{6+} , etc. The softening effect of soft doping is attributed to the creation of cation vacancies in the perovskite lattice when the soft doping ions enter the lattice structure [6]. Soft doping counteracts the natural p-type conductivity of the PZT and thus increases the electrical resistivity of the material by at least 3 orders of magnitude. A-site vacancies introduction enhances domain mobility under applied electric field and results in better ferroelectric and piezoelectric properties [6]. Ceramics produced with these additives are characterized by square hysteresis loop, low coercive fields, high remnant polarization, high dielectric

constant, maximum coupling factor, higher dielectric loss, high mechanical compliance, and reduced aging. Hard doping ions in PZT include K^+ , Na^+ , which occupy A-sites and Fe^{3+} , Co^{2+} , Mn^{2+} , Mn^{3+} , Ni^{2+} , Mg^{2+} , Al^{3+} , Ga^{3+} , In^{3+} , Cr^{3+} , and Sc^{3+} , which occupy B-sites in the perovskite structure. Hard doping is accompanied by oxygen vacancies which have only limited solubility in the lattice. Domain reorientation is “hard” since oxygen vacancies serves as the effective pinning centers. Hence, ceramics with acceptor-type additives are characterized by poorly developed hysteresis loops, lower dielectric constant, low dielectric losses, and low compliances. High mobility of the oxygen vacancies results in higher aging rates. The most well known doping effect is perhaps La doping of PZT ceramics (PLZT) which opened the way for the production of technologically important transparent ceramics for electro-optical applications. After optical transparency of hot-pressed ferroelectric PLZT ceramics was achieved in 1969 and PLZT compositional phase diagram established (1970) (see Introduction) this group of material has been attracting attention. The first attempt to fabricate PLZT thin films by sol-gel method was done by Budd *et al.* [25]. Ever since a large number of reports on the effects of different doping elements appear every year. Despite that, the systematic investigations of rare-earth elements doped ferroelectric materials, particularly in the case of thin films, are still lacking. Investigations undertaken by Tan *et al.* [122], Sharma *et al.* [123], Boyle *et al.*, [124] and Park *et al.* [125] showed for ceramics and thin films of different compositions that lanthanides smaller than La have the tendency to substitute on B-site, leading to an acceptor-type behaviour (they substitute elements (Zr and Ti) with higher valence). Boyle *et al.* [124] investigated lanthanide series doping effects in PLnZT 4/30/70 thin films prepared by sol-gel method. It is shown that the elements from La to Gd substitute A-site i.e. are donors, elements from Th to Ho are amphoteric i.e. can occupy both A- and B-sites, and elements from Er to Lu substitute B-site, i.e. are acceptors and thus substitute Zr and Ti in B-sites. Park *et al.* [125] investigated PLZT ceramic modified with 3 mol % of lanthanide elements. The same tendency towards B-site substitution with decreasing ionic radius is concluded. Thus, atomic number of lanthanide element (hence, ionic radius) was found to determine the substitution site. The conclusions about the distribution of doping elements between A and B site are made considering the tolerance (or Goldschmidt) factor (see paragraph I.1, equation (I.1.2) and ref's 9 and 126). According to the rules of Goldschmidt, the position of the dopant in the A or the B site can be determined if the host ion and the substituted ion radii do not differ by more than 15 %.

A model for the calculation of the average size of A- and B-sites for the case of PZT type solid solution can be found in the work of Gonnard and Troccaz [126]. Thereby with

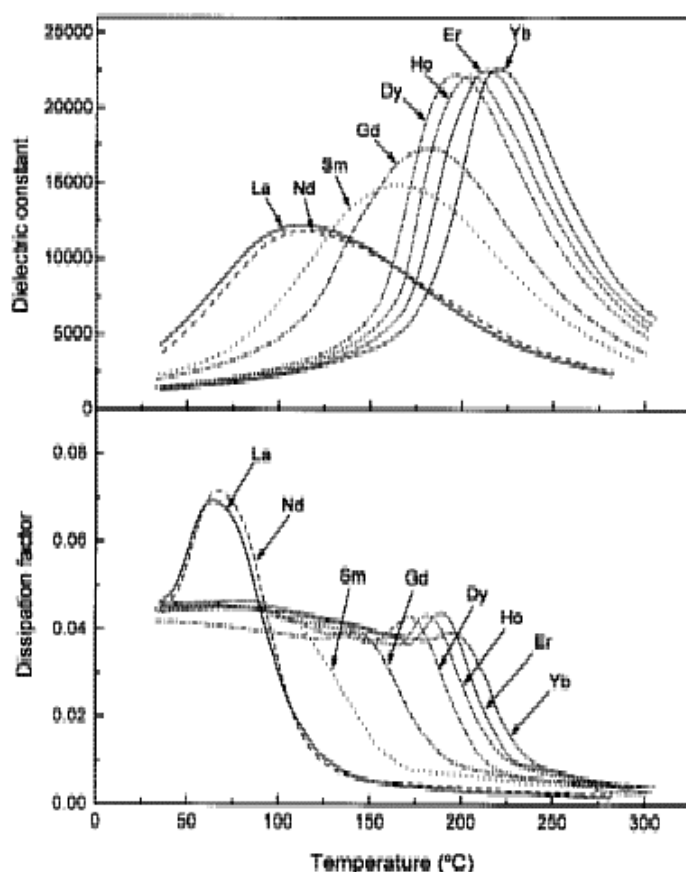


FIG.V.7.1. Temperature dependent dielectric constant and dissipation factor (loss tangent) of PLZT ceramics, modified with lanthanide ions (from the original paper of Park *et al.*[125])

decreasing ionic radii of the lanthanide element the tendency to substitute B-site rather than A-site is expected. Change in substitution type was found to strongly affect ferroelectric, dielectric and structural properties of the material. Moreover, structural sensitive parameters, such as Curie transition temperature correlate with radii of doping elements. The data, taken from the original work of Park *et al.* [125] (Fig.V.7.1) illustrate how the paraelectric-to-ferroelectric phase transition temperature can be changed in Ln elements doped PLZT ceramics. Shannigrahi *et al.* [127] fabricated and explored Er doped PZT ceramics. La- and Sm-modified PZT ceramics were investigated by Pramila *et al.* [128]. Some improvement of ferroelectric properties and fatigue resistance in Ce doped PZT thin films have been reported by Majumder *et al.* [129], who suggest that Ce can be distributed between A and B sites in 3+ and 4+ oxidation states, respectively. Structural and electrical properties of Gd and Ce doped (Pb,La)TiO₃ thin films have been investigated by Dobal *et al.* [108]. We note that Shannigrahi *et al.* [127] treat Er as A-site donor, contrary to what is proposed by Boyle *et al.* [124] and Park *et al.* [125]. Sharma *et al.* [123] also proposed rare-earth elements to be A-type donors. They claim that along with the ionic radii, the electronic configuration of rare-earth elements play an important role in the structural properties of perovskite-type materials. The

distribution of rare-earth elements between A and B sites seems also to depend on doping element concentration [128 and references therein].

It must be mentioned that (as usually accepted in the literature) the term “dopant” is used for atomic percentages less than 5%. Above this value, the compound is called “modified”. Because the present work deals with doping levels from 2 to 8 mol % of rare-earth ions, the terms will not be discerned for simplicity.

V.8. Leakage currents.

In view of leakage currents being known as one of the most important factors limiting the application of ferroelectric thin films in memory devices, this phenomena has been investigated extensively for barium strontium titanate (BST) [91,92,130], SrTiO_3 [131] $\text{Bi}_4\text{Ti}_3\text{O}_{12}$ [132] and lead-based titanates [48,96,133-138]. The analysis of temperature- and voltage-dependent leakage currents in polycrystalline thin films is one of the most complicated issues, since different conduction mechanisms may take place in the same temperature and voltage ranges. Review of basic conduction processes in dielectric films can be found in textbooks (see, for example Scott [15] and Sze [139]).

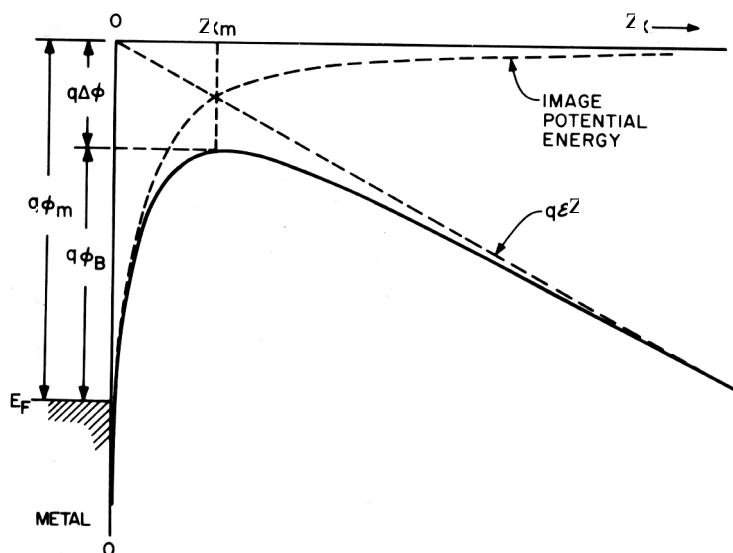


FIG.V.8.1. Energy-band diagram of a contact between a metal surface and a vacuum. The metal work function is $q\phi_m$. The effective work function (or barrier) is lowered when an electric field is applied to the surface. The lowering is due to the combined effects of the field and the image force (p.250 in ref. 139).

Following Scott [15], ferroelectric film capacitors on metal electrodes consists of very complex structures in which electrons, holes, and ions all contribute to conduction, and where a variety of mechanisms – including surface-limited processes such as thermionic Schottky

currents and quantum mechanical Fowler-Nordheim currents, as well as bulk-limited processes such as Poole-Frenkel and Space-Charge-Limited Currents (SCLC) can all play an important role. Typically these processes are all present at the same time, and unfortunately they are not additive; rather, they result in non-linear integral equations for total leakage current $J(V)$.

The Schottky conduction mechanism is based on the image-force-induced lowering of the potential energy for charge carrier emission when an electric field is applied across metal-semiconductor interface. When an electron is at the distance z from the metal, a positive charge will be induced on the metal surface. The force of attraction between the electron and induced positive charge is equivalent to the force that would exist between the electron and an equal positive charge located at $-z$. This positive charge is referred to as the image charge. The attractive force, called the image force, is given by the Coulomb relation (p. 250 in ref.139):

$$G = \frac{-q^2}{4\pi(2z)^2 \epsilon_0} = \frac{-q^2}{16\pi\epsilon_0 z^2} \quad (\text{V.8.1})$$

where q is the charge of the electron and ϵ_0 is the permittivity of free space. The work done by an electron in the course of its transfer from infinity to the point z is given by

$$A(z) = \int_{\infty}^z G dz = \frac{q^2}{16\pi\epsilon_0 z} \quad (\text{V.8.2})$$

when an external field E is applied, the total potential energy PE as a function of distance is given by the sum

$$PE(z) = \frac{q^2}{16\pi\epsilon_0 z} + qEz \quad (\text{V.8.3})$$

at the equilibrium position

$$\frac{dPE(z)}{dz} = -\frac{q^2}{16\pi\epsilon_0 z^2} + qE = 0 \quad (\text{V.8.4})$$

The Schottky barrier lowering (also referred to as image force lowering) $\Delta\phi_B$ and the location of the lowering, z_m are given by

$$z_m = \sqrt{\frac{q}{16\pi\epsilon_0 E}} \quad (\text{V.8.5})$$

and

$$\Delta\phi_B = \sqrt{\frac{qE}{4\pi\epsilon_0}} = 2Ez_m \quad (\text{V.8.6})$$

Corresponding energy-band diagram is shown on Fig.V.8.1 [139]. The equations can also be applied to metal-semiconductor systems. However, the field should be replaced by the maximum field at the interface, and the free-space permittivity ϵ_0 should be replaced by an appropriate permittivity ϵ , characterizing the semiconductor medium, that is,

$$\Delta\phi_B = \sqrt{\frac{qE}{4\pi\epsilon}} \quad (\text{V.8.7})$$

The current density is expressed as:

$$J = A^* T^2 \exp\left[\frac{-q(\phi_B - \sqrt{qE/4\pi\epsilon})}{k_B T}\right] \quad (\text{V.8.8})$$

if Schottky-type emission is the process, determining charge transport in dielectric film. A^* is so-called effective Richardson coefficient.

The Poole-Frenkel emission (p. 402 in ref. 139) occurs due to field-enhanced thermal excitation of trapped electrons into conduction band. Current density for the case of Poole-Frenkel emission is given by the equation:

$$J \approx E \exp\left[\frac{-q(\phi_B - \sqrt{qE/\pi\epsilon})}{k_B T}\right] \quad (\text{V.8.9})$$

For trap states with coulomb potentials, the expression is virtually identical to that of the Schottky emission. The barrier height, however, is the depth of the trap potential well, and the quantity $\sqrt{q/\pi\epsilon}$ is larger than in the case of Schottky emission (V.8.8) by a factor of 2, since the barrier lowering is twice as large due to the immobility of the positive charge.

The space-charge-limited current (SCLC) results from a carrier injected into the insulator, where no compensating charge is present. The current for the unipolar trap-free case is proportional to the square of the applied voltage. In SCLC regime current varies with thickness of insulating film not ohmically ($1/d$), but as $1/d^3$. This

$$J = B \frac{V^2}{d^3} \quad (\text{V.8.10})$$

dependence is known as the Mott-Gurney law (p.86 in ref.15). B is proportional to dielectric constant of the material and mobility of electrons μ_e . In more general case current density is expressed as [96]:

$$J = B \frac{V^n}{d^m} \quad (\text{V.8.11})$$

where n and m are voltage and thickness exponents, respectively.

As already mentioned, leakage current phenomena are being extensively investigated in different systems of ferroelectric materials. BST, PZT, PT, PLZT and BTO (bismuth titanium oxide) are among them. Paek *et al.* [91] showed that leakage current through BST thin films decreases with increasing film thickness. This effect was attributed to change in microstructure as function of film thickness. In fact, SEM and HRTEM observations confirmed that grain size in sputtered BST films increases with film thickness. Grain boundaries were treated as the leakage current paths. From this point of view it is expected to observe increased contribution of grain boundaries into conduction processes for thinner films. However, voltage and temperature dependences of leakage current were not presented. More detailed analysis of leakage currents in BST thin films were reported by Hwang *et al.* [92] who discussed the influence of deposition techniques on conduction behaviour. It was claimed that BST and Pt junction form so-called blocking contact with potential barrier strongly dependent on deposition method. While the barrier height for sputtered film was found to be 1.6-1.7 eV, OMCVD deposited film was characterized by a value of 1.2 eV. Different interfacial properties of the films were claimed to be the reason for these results. It was also suggested that at low temperature tunnelling processes are responsible for charge transport. At high temperature Schottky type conductivity is dominant. Change of operating mechanism occurs at temperatures of about 120°C.

Nagaraj *et al.* [130] investigated leakage current in all-perovskite LSCO (lanthanum strontium cobalt oxide)/BST/LSCO system. From J - E measurements it was inferred that bulk-limited Poole-Frenkel mechanism is predominant in the investigated system. The same conclusion was drawn by Al-Shareef and Dimos [137] for conduction processes in lead titanate thin films.

The role of SCLC mechanism in PZT thin film has been discussed by Shin *et al.* [96]. It was shown that this mechanism is dominant at high values of applied bias ($E > 400$ kV/cm) whereas at lower field, conduction processes are being operated by Schottky emission. Space-charge-influenced-injection model has been advanced by Stolichnov and Tagantsev [134]. They analyzed voltage and time dependent leakage currents in PZT thin films fabricated on platinized Si substrates by sol-gel, OMCVD and sputtering techniques. Following the proposed model, the leakage current is determined by carriers injection through the electrode (the carriers injected are holes). Specifically, the current is limited by the built-in charge in near-electrode area which has the same sign as the injected carriers due to upward band bending near the electrodes.

Cho and Jeon [135] showed that not only the leakage current magnitude but also the type of operating mechanism is sensitive to processing conditions. The fitting of the J - E curves obtained for sol-gel processed PZT films to different (interface and bulk limited) conduction processes revealed Schottky type emission for the specimen annealed in N_2 atmosphere and mixed Schottky and SCLC conductivity for the specimen annealed in O_2 atmosphere.

In another report Stolichnov *et al.* [136] discussed the role of electrode material in the degradation of the leakage properties of PLZT thin films (hybrid Pt/SRO (strontium ruthenium oxide) structure was utilized as the top electrode). The authors supposed that diffusion from the electrode into the thin film material can cause leakage current increase through the capacitor. They concluded that electrode material is one of the critical parameters determining the performance of ferroelectric thin film devices.

Finally, the effects of donor doping on the leakage currents in PZT thin films were reported by Kim *et al.* [138]. They obtained lower leakage current density in Nb and La doped films as compared to non-doped specimens, which is expectable bearing in mind p -type conductivity of PZT.

It can be concluded that the leakage currents in ferroelectric thin film capacitors are affected by various factors such as fabrication conditions, microstructure, electrode material and doping. Appropriate choice of deposition parameters, substrate and doping can suppress conductivity and thereby improve the quality of the device. From fundamental point of view, the mechanisms of conductivity are still subject of controversy, and the phenomenon of leakage current in ferroelectric thin films is not well understood. Systematic investigations including thickness effects, voltage and temperature dependences as well as type of electrode material are therefore needed for a thorough understanding of the conduction mechanisms in ferroelectric thin films.

V.9. Pyroelectric and piezoelectric properties of ferroelectric thin films.

Pyroelectric and piezoelectric properties of lead-based perovskite thin films prepared by different methods are considered for applications in integrated IR detectors and imaging devices and MEMS by many research groups [43, 140-144]. The possibility to fabricate high quality thin films with pyroelectric coefficients comparable to those known for bulk ceramics has been demonstrated [140,141]. It was shown that composition of thin film is critical for pyroelectric properties. Tseng *et al.* [142] reported on preparation and characterization of lead

titanate thin films substituted with various amounts of La by pulsed laser deposition. Films modified with 10 mol % of La (PLT10) revealed a higher pyroelectric coefficient compared to that of 5 mol % modified film (PLT5). This result was explained in terms of La induced decrease of the Curie transition temperature (it is known that the pyroelectric coefficient of ferroelectric materials reach maximum in the vicinity of the phase transition temperature). Similar effects of La doping on pyroelectric properties was reported by Kamada *et al.* [143] for RF-magnetron sputtered PbTiO_3 thin films. Furthermore, it was discovered [44,140,141] that while non-poled ferroelectric ceramics do not show any pyroelectric activity, as-grown thin films reveal measurable pyroelectric response. This effect is attributed to self-polarization developed in films during cooling through the Curie transition temperature. This effect is reported to be very stable and comparable to subsequent room temperature poling [144].

Compared to bulk ceramics, the piezoelectric properties of lead based thin film were studied to a lesser extent. In general, the piezoelectric response of ferroelectrics is determined by the contribution of domain structure which, in turn, depends on grain size. Ferroelectric thin films with grain sizes below 1 μm demonstrate lower piezoelectric coefficients compared to bulk ceramics [145]. Film thickness and texture dependent piezoelectric properties are another important feature of ferroelectric thin films. Lian and Sottos [67] investigated the piezoelectric properties of PZT thin films with emphasis on thickness and preferentially oriented state effects. The piezoelectric coefficient was found to decrease with the film thickness. This result was attributed to residual stress in the films which relaxes as thickness of the films increases. On the other hand, films grown with (100) preferred orientation were found to have a higher piezoelectric constant than that of (111) preferentially oriented films. Doping effects on the piezoelectric properties were mainly addressed in bulk ceramics [6,8]. The piezoelectric properties of thin films arise from the superposition of many factors such as doping, thickness, stress state, grain size, nature of electrodes, preferred orientation of grains in polycrystalline films, self-polarization states and presence of electrode-film interfacial layers and are, therefore, more complex than in bulk materials.

VI. Aims of this work

Analysis of the literature available revealed that La is the most explored doping element in lead-based ferroelectric ceramics and thin films. Effects of doping by other elements of lanthanide series were mainly investigated in PZT and PLZT bulk ceramics and have not been adequately understood in the case of thin films. Moreover, to our knowledge, systematic efforts to investigate the dependence of structural, optical and electro-physical properties of *lead titanate thin films* on rare earth elements type and concentration were not undertaken. In view of increasing importance of application of ferroelectric thin films in up-to-date device technology, it is considered to be necessary to trace the structural and electro-physical properties of the films with regard to the nature and concentration of doping ions. It is believed that it is important to demonstrate the possibility of the most critical properties from the point of view of thin films application (optical, dielectric, ferroelectric properties and leakage currents) to be tailored by appropriate doping. It is also believed that detailed analysis of dielectric, ferroelectric and leakage properties of the films can cast light onto the substitution type and distribution of lanthanide elements between A- and B-sites of perovskite lattice with respect to their ionic radii. For this purpose, conventional sol-gel method is adopted to process films because it provides versatile and cost-effective processing route with controlled stoichiometry and microstructure. (111)Pt/Ti/SiO₂/Si and LaNiO₃/(111)Pt/Ti/SiO₂/Si heterostructures are taken as the substrates. Commercially available (111)Pt/Ti/SiO₂/Si substrates are used in the majority of the cases for polycrystalline thin films deposition. Considering the effect of substrate on the structural and electro-physical properties of the films, the same substrates is utilized in the present work purposely to compare correctly the results obtained with those published by other research groups.

Utilization of conducting oxides as an electrode material instead of traditional metallic (platinum or gold) was discussed in literature [31, 111-114]. Although the improvement of thin films performance was reported, correlation between structural, dielectric and ferroelectric properties and kind of substrate have not been investigated systematically.

It was also shown that such effects as imprint and thickness dependent properties found especially for the ferroelectric thin films significantly limit the area of possible

application. Understanding the nature of these effects will contribute to the improvement of the material performance.

In this work, the results obtained on microstructure development and Ln-doping effects on properties of lead titanate thin films are summarized. Attention is also paid to effects due to bottom electrode material and film thickness. The results are discussed taking into account substitution site preference, film texture, lattice parameters modification and stress states. Owing to the importance of ferroelectric thin films in device development, the pyroelectric and piezoelectric properties of selected films are also investigated. The attempt to tailor pyroelectric and piezoelectric response from the thin film detector via the doping with lanthanide elements is done.

VII. Preparation and characterization of lanthanide ions doped PbTiO₃ thin films: experimental details

In the present chapter the detailed procedure of sol-gel processing used for specimen preparation is described. The main efforts were directed towards optimization of thermal conditions and precursor solution properties in order to obtain high quality, crack-free samples with controlled microstructure and thickness, crucial for the comparative characterization to follow. The experimental techniques involved in the characterization of the structural and electrophysical properties are also described in the corresponding sections.

VII.1. Sol-gel fabrication of pure and rare-earth substituted PbTiO₃ thin films and optimisation of deposition parameters.

Acetic acid, acetylacetone and 2-methoxyethanol modified sol-gel method was utilized to fabricate pure and lanthanide (Ln) elements doped lead titanate thin films. The flow chart diagram shown in Fig.VII.1.1 illustrates the process of precursor solutions preparation. Lead acetate, tetraisopropyl orthotitanate, acetic acid, acetylacetone and 2-methoxyethanol were provided by Fluka Chemical, Inc., Germany. Ce, Sm, Dy, Er and Yb acetates were purchased from Strem Chemicals, Inc., U.S.A. The stoichiometry of doped specimen was $\text{Pb}_{(1-x)}\text{Ln}_x\text{TiO}_3$, where $x = 0.02, 0.05$ and 0.08 . I.e. 2, 5 and 8 mol % of lanthanide ions were designated to substitute lead on A-sites. Firstly lead and Ln acetates were dissolved in acetic acid and refluxed for 3 hours at 110°C to evaporate associated water. 3 mol of acetic acid were taken to dissolve 1 mol of lead and Ln acetates. Tetraisopropyl orthotitanate was stabilized with acetylacetone in a ratio of 1:2 mol. Both parts were then mixed together at room temperature and diluted with 2-methoxyethanol to reach the final concentration of 0.5 mol/l. Regardless of the type of dopant and doping level, yellow, transparent sols were obtained. The solutions were filtered through 0.2 μm syringe filter just prior to film deposition. The films were formed by multiple spin-coating depositions onto different substrates with 3000 rpm for 30 s using Chemat Technology, Inc. (USA) KW-4A photoresist spin-coater. Each coating was dried on a hot plate at 340°C for 5-10 min followed by annealing at temperatures between 550 and 700°C.

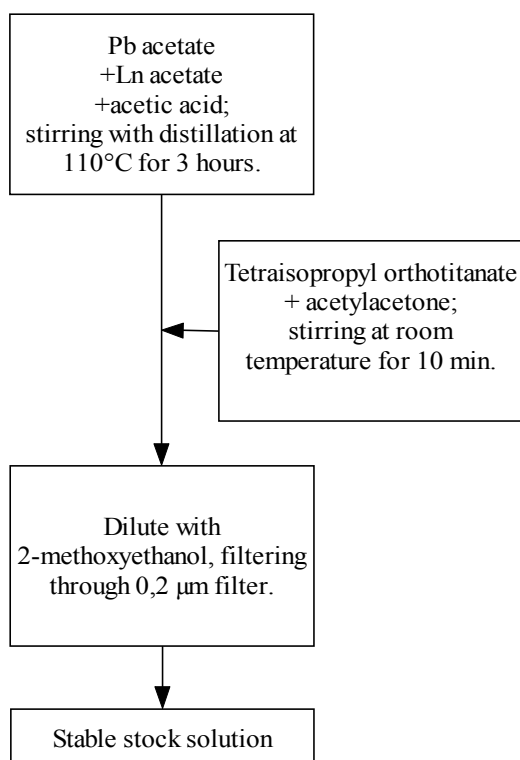


FIG.VII.1.1. Flow chart diagram of PLnT precursor solution preparation.

It is known that lead is the most volatile element in PZT based solid solutions [146]. Purposely to compensate lead loss during high temperature annealing of the specimens lead excess is being added at the stage of sol preparation. At the same time, excessive Pb can lead to the formation of liquid phase that in turn affects microstructure of the specimens. In order to trace the effect of lead excess on the morphology of the films and optimize their microstructure, 0, 10 and 20 mol % of Pb excess were added to non-doped lead titanate precursor. As shown before [76], fabrication of pure lead titanate films is more difficult in comparison to lanthanide elements doped samples due to strong cracking effects caused probably by the high tetragonal distortion and stress development during cooling through the Curie temperature. Similar deposition parameters (temperature and time of annealing, solution concentration etc.) for pure and doped lead titanate films appear therefore difficult to maintain [76]. At the same time, the electrophysical properties of ferroelectric films are very sensitive to deposition parameters. In order to allow a meaningful discussion of the effects of doping elements on the film properties to be made, the processing parameters were explored and optimised first on pure lead-titanate for the purpose to obtain crack free films. The optimized processing conditions were then adopted for doped and non-doped films. The processing parameters explored were: annealing conditions, lead excess and sol concentration.

Fig.VII.1.2 shows back scattered electron (BSE) SEM micrograph of lead titanate thin films prepared from the sol of calculated stoichiometry $\text{Pb}_{1.2}\text{TiO}_3$ and consisting of 7 coatings. The first layer was pre-annealed at 550°C for 10 min in order to reduce the energy of crystallization of next layers. Then, three coatings were performed followed by pre-annealing at 550°C for 10 min. Finally, additional three coatings were deposited and the specimen was subsequently annealed in the furnace at 600°C for 10 min in air. As can be seen from the surface morphology illustrated in Fig. VII.1.2, the deposition conditions described above lead to rather coarse and non-uniform microstructure interspersed with cracks, but free from visible second phase inclusions. The film thickness determined by means of SEM cross-section specimen is about 650 nm. Under these conditions, crystallization was accompanied with crack formation which is unacceptable for a proper characterization of the film properties.

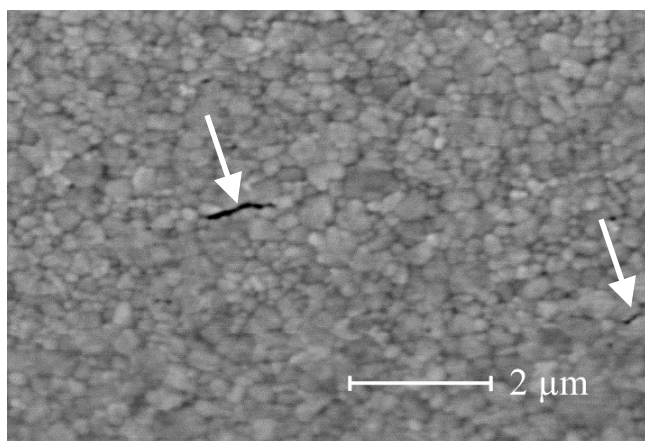


FIG.VII.1.2. BSE SEM top-view of lead titanate thin film, consisting of 7 layers of solution with the stoichiometry $\text{Pb}_{1.2}\text{TiO}_3$ and concentration 0.5 mol/l, annealed at 600°C for 10 min. Cracks appeared due to the development of stress during film crystallization are indicated by arrows.

Fig.VII.1.3 shows lead titanate processed from a sol containing no lead excess. The film consisted of 3 layers, and annealed at 600°C for 10 (a), 20 (b) and 30 (c) min. The reduction of the amount of deposited layers and the use of a stoichiometric sol composition (with no lead oxide excess) has allowed to obtain crack-free films. On the other hand, it seems that, regardless of annealing time, complete crystallization of the perovskite phase was not achieved, and some fraction of a lead depleted phase, probably pyrochlore (lead depleted areas are seen in the BSE micrograph as dark contrast areas because of atomic number contrast) still exist.

In order to avoid lead depletion and to improve crystallization of the films, a Pb-excess of 10 mol % was adopted, and a temperature of 700°C was chosen keeping the sol concentration at 0.5 mol/l. Fig. VII.1.4 shows the microstructure obtained. One can see that the film has been damaged by peeling probably due to high stress.

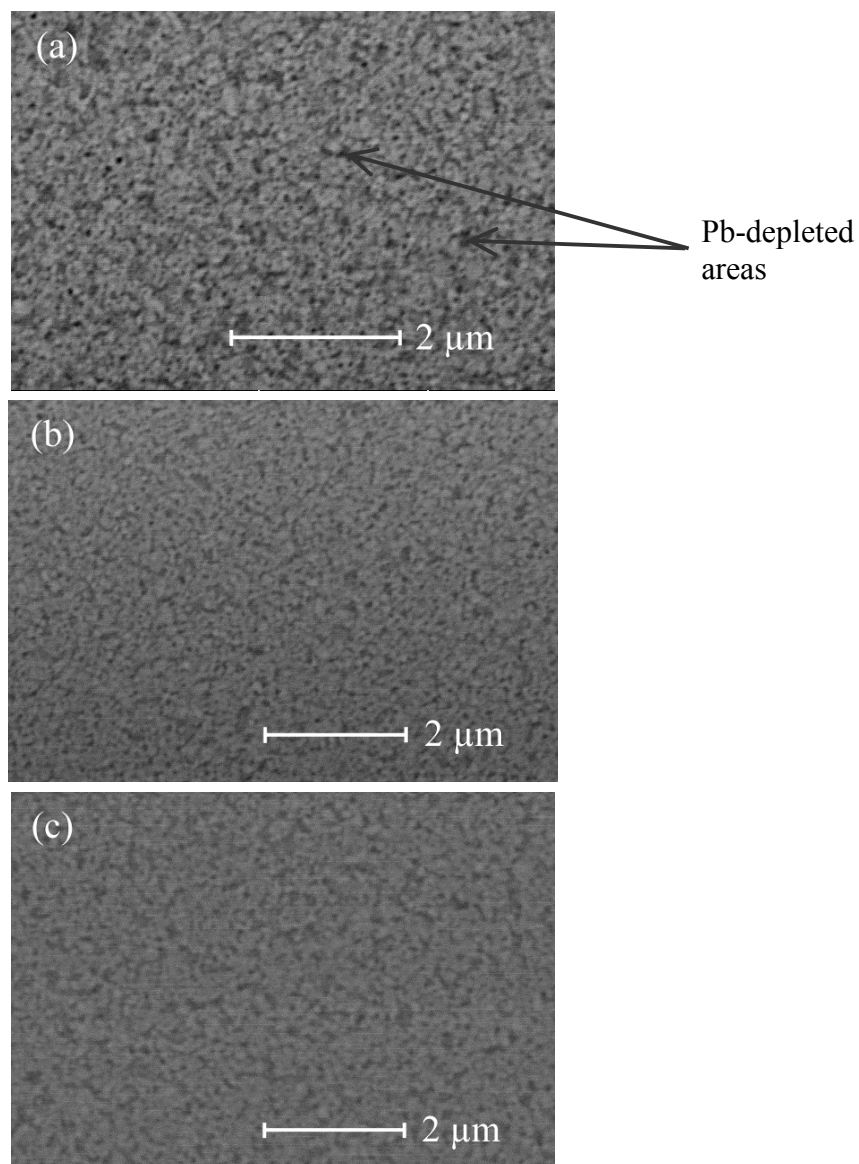


FIG.VII.1.3. BSE SEM micrographs of lead titanate thin films, processed from a stoichiometric sol and concentration of 0.5 mol/l. The films consisted of 3 layers with final annealing at 600°C for 10 (a), 20 (b) and 30 (c) min. Dark areas are Pb-depleted second phase particles, probably pyrochlore (indicated by arrows).

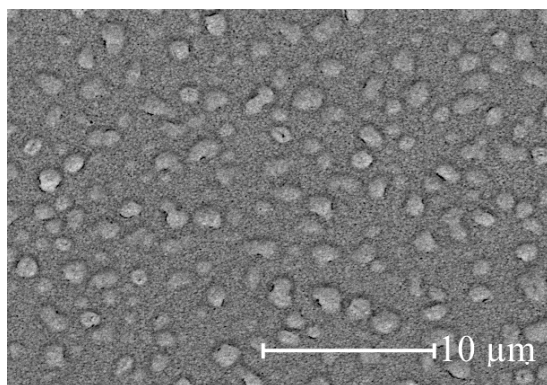


FIG.VII.1.4. Lead titanate thin film, prepared from the sol with 10 mol % Pb excess and the concentration 0.5 mol/l. The film consisted of 3 layers. Film was annealed at 700°C for 5 min.

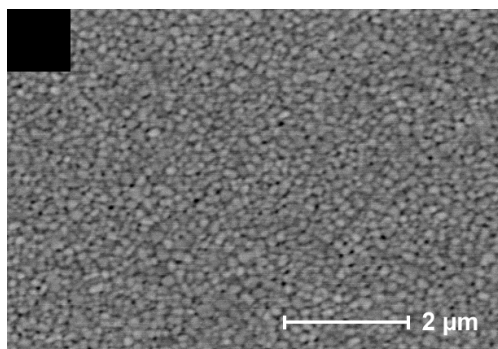


FIG.VII.1.5. BSE SEM micrograph of PbTiO_3 thin film deposited by sol-gel method upon (111)Pt/Ti/SiO₂/Si commercial substrate. Film is fabricated from the sol containing 10 mol % of Pb excess and concentration 0.4 mol/l and consists of four coatings. Film was annealed at 700°C for 5 min.

The next step in the deposition optimization consisted in reducing the concentration of the sol which leads to thinner individual layer. Considering the results of microstructural characterisation presented above, it was inferred that the reduction of the sol concentration can diminish the risk of cracking or peeling. Therefore, the sols were diluted with 2-methoxyethanol to give a final concentration of 0.4 mol/l. The crystallization temperature was kept at 700°C and the number of layers at four. It appeared that 5 min annealing time was sufficient for well crystallized, fine grained films (Fig.VII.1.5). The same conditions were then utilized to fabricate Ce, Sm, Dy, Er and Yb doped specimens. As mentioned above, doping levels were set to 2, 5 and 8 mol %. However, a sol with 8 mol % Ce could not be successfully prepared because of the low solubility limit of Ce-acetate in 2-methoxyethanol. Doping with Yb led to high conductivity of the film for doping levels higher than 2 mol %. These films were therefore omitted from further electrical characterization. The thickness of the films was determined by means of ellipsometry (see corresponding sections for experimental details). The microstructures of substituted films are very similar to that of non-doped lead titanate. Fig'sVII.1.6(a-g) exemplify the AFM micrograph obtained in non-contact mode for pure and doped with 2, 5 and 8 mol % of Sm and Er films. Mean grain size and root mean square (RMS) roughness of the corresponding specimens are listed in Table VII.1.1.* For pyroelectric and especially piezoelectric properties characterization, thicker films are preferable since it can increase signal-to-noise ratio and improve the quality of the data. 950 nm thick PST5 and PET5 thin films were fabricated on commercial (111)Pt/Ti/SiO₂/Si substrates. 12 layers in total were deposited under the following conditions. Each layer was dried on a hot plate at 340°C for 5 min and pyrolyzed at 550°C for 5 min. Intermittent annealing in a preheated furnace at 700 °C had to be used in order to avoid cracking.

* Grains diameter and RMS roughness were calculated using the scanning probe imaging processor (SPIP, version 2.3, Image Metrology) software.

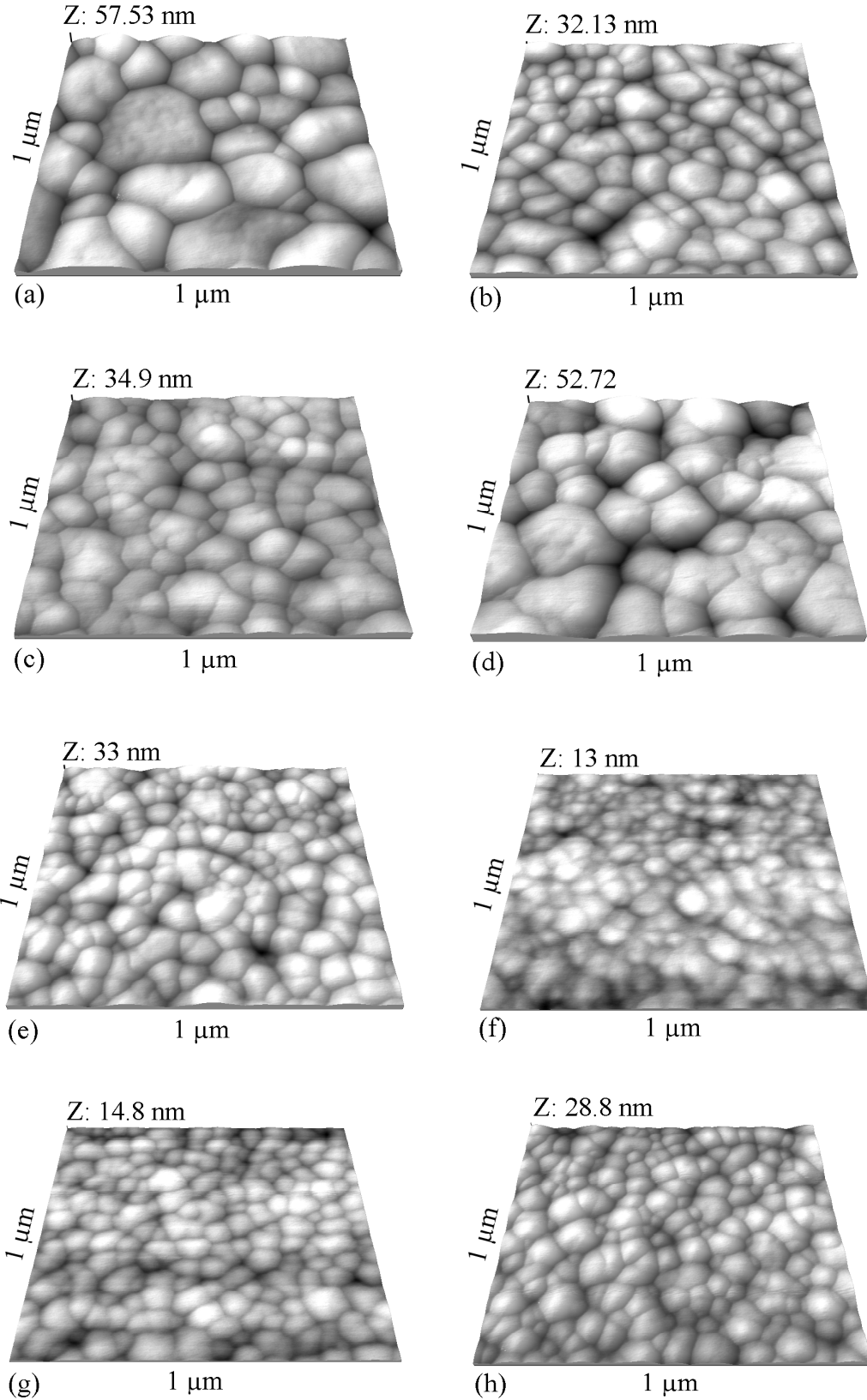


FIG.VII.1.6. AFM micrographs of pure and Sm and Er doped films: PbTiO_3 , Pt electrode (a); PbTiO_3 +2 mol % Er, Pt electrode (b); PbTiO_3 +5 mol % Er, Pt electrode (c); PbTiO_3 +8 mol % Er, Pt electrode (d); PbTiO_3 +2 mol % Sm, Pt electrode (e); PbTiO_3 +5 mol % Sm, Pt electrode (f); PbTiO_3 +8 mol % Er, Pt electrode (g); PbTiO_3 +5 mol % Er, LNO/Pt electrode (h).

Table VII.1.1. Mean grain diameter and RMS surface roughness obtained from AFM investigations of pure and doped films (corresponding micrographs are shown in Fig's VII.1.6 (a-g).

Doping level	Mean grain diameter, nm		Surface roughness (RMS), nm	
	Sm	Er	Sm	Er
0	143		7.7	
2	114	107	4.73	4.32
5	100	102	2.06	4.85
8	98.7	141	3.08	8.44

To investigate thickness and the electrode material effects on the dielectric and leakage current properties (see corresponding chapters), a set of specimens doped with 5 mol % of Er was prepared on platinum and lanthanum nickel oxide (LNO). The films consisting of three, four and six coatings were prepared under the conditions described above. Sol-gel was utilized to produce the LNO buffer layer onto commercial (111)Pt/Ti/SiO₂/Si substrates. Lanthanum nitrate hexahydrate and nickel acetate were dissolved in 2-methoxyethanol in ratio 1:20 mol and refluxed with back-flashing at 135°C for 30 min. 2 layers were spin-coated, dried on a plate at 340°C for 5 min before final annealing at 700°C for 10 min. A film thickness of 67 nm was determined by means of ellipsometry. A AFM micrograph of 5 mol % of Er doped film is shown in Fig.VII.1.6(h). RMS roughness and average grain diameter were calculated for this specimen as 5.24 nm and 108 nm, respectively. Pure and doped lead titanate films, involved in the present study are listed in Table VII.1.2.

Table VII.1.2. List of the lead titanate films investigated. The film thickness was obtained from ellipsometric measurements.

Dopant	Doping level, mol %	Film thickness							Sample designation
		Substrate							
		(111)Pt/Ti/SiO ₂ /Si				LNO/Pt/Ti/SiO ₂ /Si			
none	-	267				-			PT
Ce	2	245				-			PCT2
	5	280				-			PCT5
	8	235				-			PCT8
Sm	2	245				-			PST2
	5	308		950	-			PST5	
	8	235				-			PST8
Dy	2	224				-			PDT2
	5	208				-			PDT5
	8	264				-			PDT8
Er	2	203				-			PET2
	5	200	285	375	950	195	260	390	PET5
	8	212				-			PET8
Yb	2	238				-			PYT2

For electrical measurements, round Pt top electrodes with a diameter of 0.6 mm were sputtered through a shadow mask. Post top electrode deposition annealing was conducted on a plate at 400°C for 10-15 min. The contact to the bottom electrode was produced by scratching a corner of the specimen and subsequent deposition of silver paste. For pyroelectric and piezoelectric measurements (case of 12-layer films) Pt top electrodes of the configuration shown in Fig. VII.1.7 were sputtered through a shadow mask, and annealed as described above. In the interferometric measurements of the piezoelectric properties, the adjacent (small) contact was used to apply the driving AC voltage whereas central (large) contact was exposed to the laser. In the pyroelectric characterization of the films, opposite extra-contacts were used to measure the temperature dependent resistance of the contact group (see below). This specific configuration of the top electrode was developed since the existent experimental set-ups did not allow getting the reliable contacts utilizing the conventional round electrodes.

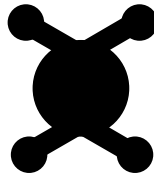


FIG.VII.1.7. Scheme of the sputtered Pt top electrode utilized for pyroelectric and piezoelectric measurements. Central contact (diameter 1.5 mm) is connected via the strips (1x0.5 mm) with four extra contacts (diameter 1 mm).

VI.2. Experimental details on structural and electrophysical properties characterization.

A. X-ray diffraction (XRD)

Phase characterization included Θ - 2Θ and grazing incidence (GI) X-ray diffractometry (Seifert 3000 PTS powder diffractometer equipped with four-cycle goniometer, $\text{CuK}\alpha$ monochromated radiation, $\lambda=1.5418 \text{ \AA}$, grazing angle 2°). Θ - 2Θ scans were measured in 2Θ angle range from 20° to 50° with a step of 0.04° and a duration 20 s/step. For grazing incidence experiment step width and duration were held at 0.05° and 10 s/step, respectively. In-plane alignment was monitored by (100) pole figures, which were measured in Schulz reflection geometry by scanning the tilt angle of the goniometer, Chi , in the range from 0° to 65° and azimuthal angle, Phi , from 0° to 360° , using a 2.5° step for both. No correction for defocusing and absorption were introduced since, for the thickness of the film studied, both

effects compensate each other in the range of χ used [52]. Fibre texture (FT) plots were obtained by scanning χ angle with a step of 0.5° .

B. Raman spectroscopy

The Raman spectra were obtained at room temperature in back-scattered geometry using a Dilor spectrometer supplied with micro-Raman set-up. 514 nm, 488 nm and 458 nm lines from Ar-laser and 633 nm line from HeNe-laser were used. The collection time was varied in the range from 5s to 100 s to optimize signal-to noise ratio and minimize the contribution from the intense line of Rayleigh scattering.

C. X-ray photoelectron spectroscopy (XPS)

Additionally, oxidation state of Ce in Ce-substituted lead titanate thin films was investigated by means of X-ray photoelectron spectroscopy using Al $K\alpha$ monochromator (Omicron Full Lab System). The measurements were performed on as-deposited films and after Ar ion cleaning at 1 keV and 70 nA for 2 min.

D. Scanning electron microscopy (SEM)

The microstructures of the specimens were observed by means of scanning electron microscopy (Philips XL 30). The best resolution was achieved by using the back scattered electrons (BSE) imaging mode. SEM was mainly involved in specimen characterization during optimisation of film deposition parameters (see paragraph VII.1).

E. Atomic force microscopy (AFM)

Additionally to SEM, AFM technique (Surface Imaging Systems) was used for monitoring the microstructure of the films. Grains diameter and RMS roughness were calculated using the scanning probe imaging processor (SPIP, version 2.3, Image Metrology) software (see paragraph VII.1).

F. Ellipsometry

The thickness and optical properties (refractive index and extinction coefficient) of the films prepared were measured by means of ellipsometry. Considering the data obtained at $\lambda=632.8$ nm (HeNe-laser) for various incidence angle from 30° to 85° and four points of the sample surface, an over determined system was achieved, which allowed for cross-checking, increased resolution and testing the employed model. As a measure of the resolution, the

change in the thickness due to change in n by 1% is noted. The algorithm of the complex refractive index calculation and optimisation was realized with MathCAD software [147,148]. The ellipsometric thickness of prepared thin films was found to be in the range from 200 to 300 nm (see Table VII.1.2). The refractive indices of the specimens were obtained from ellipsometrically determined Ψ and Δ utilizing equations (IV.6.1-IV.6.7). The film thickness was then found as the result of parameters fitting to the film-substrate model (Fig.IV.6.3).

G. Ferroelectric hysteresis measurements

The ferroelectric hysteresis loops of the films were measured using Radiant Technologies, Inc. RT6000S ferroelectric testing systems operated in a virtual ground mode (VGM). The principles of this mode are described in paragraph IV.7. In our experiments, the signal was applied to the bottom electrode of the ferroelectric capacitor structure. The amplitude of the driving signal and pulse time were from 0.5 to 19 V and from 0.13 to 0.2 ms, respectively.

H. Impedance and leakage current measurements

The dielectric properties (dielectric constant, loss tangent) of the ferroelectric films can be characterized by the bridge methods depicted in Fig.IV.8.1. The leakage current characteristics of the specimens are usually measured with high precision electrometers.

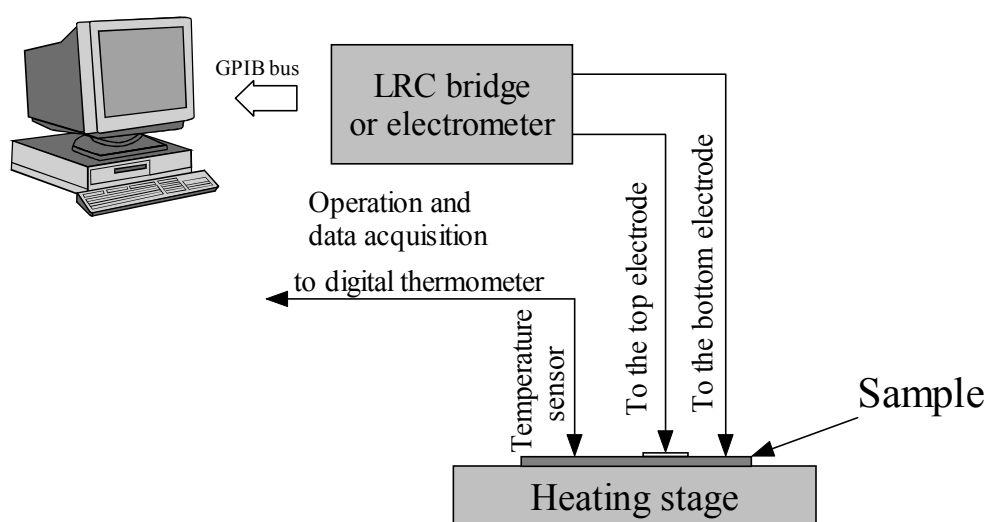


FIG.VII.2.1. Scheme of the set-up for characterization of dielectric and leakage properties of the films.

In the present work Agilent 4192A LRC meter (or impedance analyser) was utilized for dielectric testing. The leakage current properties were investigated using Keithley 6517A electrometer. Fig.VII.2.1 shows schematically the set-up utilized in this work for dielectric

and leakage properties characterization. The Curie temperatures, dielectric constants and loss tangents of the films were investigated using an appropriate set-up including a heating stage and Agilent 4192 A LRC meter. For measurements at elevated temperatures, the set-up contains heating stage which allowed temperature controlling within an accuracy of 0.2-0.5 °C. Commercial GMH3230 (Greisinger Electronic, Germany) digital thermometer interfaced with personal computer was utilized for sample surface temperature control. In the case of impedance measurements, in order to exclude contribution from resistance and inductance of wires and contact group (particularly at high frequency), measurement through overall frequency range allowed by the device (from 5 Hz to 13 MHz) was conducted in a short-cut regime. The data obtained were then subtracted from the experimental results.

I. Pyroelectric measurements

Pyrodynamic and bolometric measurements were performed using a self-made experimental set-up including a computer controlled lock-in amplifier (Ametek 7225), function generator (Agilent 33120 A), current source and voltmeter (Keithley 2420). The thermal excitation is done sinusoidally with a Peltier element. Surface temperature measurements are performed using the front electrode as a bolometer, Fig. VII.2.2. The lock-in amplifier is employed to monitor the bolometric voltage variation. The Pt electrode is contacted with two needles and the current and voltage is supplied and measured separately (4-wire sense). For a constant current of 3 mA the measured voltage was found to be around 1.5 V. For the calibration of the Pt electrode as a bolometer, the Peltier element is modulated at a frequency of 5 mHz and the temperature is monitored with a thermocouple element. The amplitude of the temperature variation was about 1.4 °C and the resulting voltage amplitude was around 2.2 mV. An evaluation method using the two first-order Fourier coefficients of the temperature and voltage signals is applied to determine the amplitudes. From the amplitudes the calibration coefficient can be calculated. The bolometric calibration was done twice and the coefficients values of 0.6131 and 0.6162 °C/mV obtained were close to each other. The dependence of surface temperature of the modulation frequency of thermal excitation is computed from the measured bolometric voltage amplitude and the above-mentioned coefficient. For pyroelectric coefficient measurements the temperature was modulated in the frequency range from 30 mHz to 200 mHz and the pyroelectric coefficient was obtained from measuring the resulting pyroelectric current as a consequence of temperature changes in the ferroelectric material [45]. For sinusoidal temperature modulation

the pyroelectric coefficient of a ferroelectric film can be calculated from the pyroelectric current:

$$p = \frac{\Delta i_p}{\omega \Delta T S} \quad (\text{VII.2.1})$$

It is assumed that the temperature variation is homogeneous in the film and hence equal to measured surface temperature.

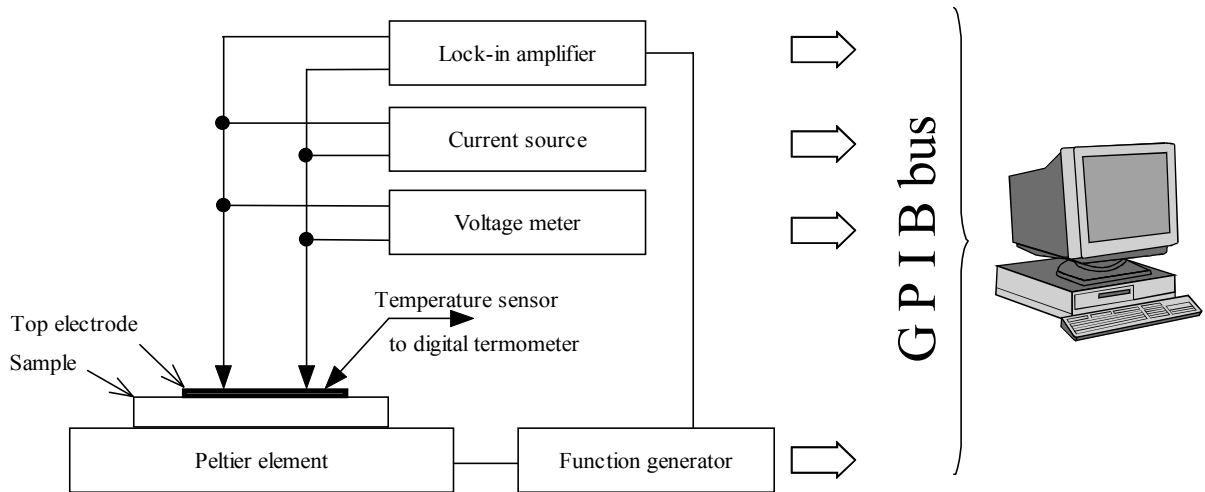


FIG.VII.2.2. Experimental set-up for bolometric and pyrodynamic measurements.

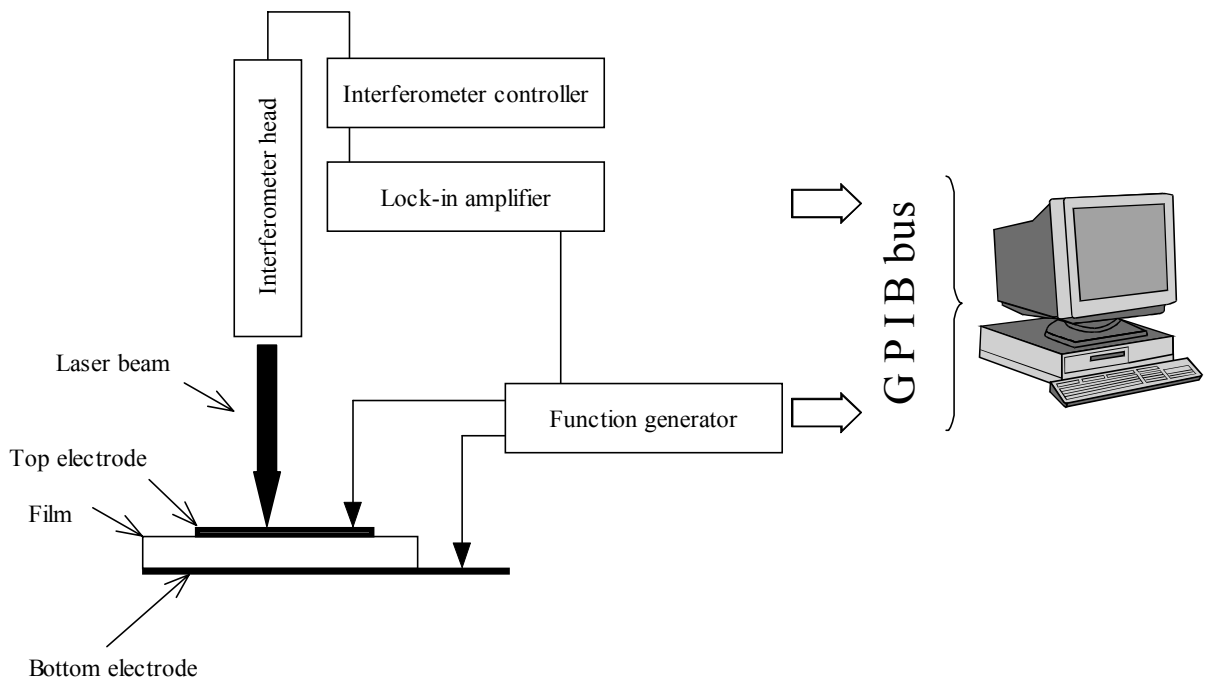


FIG.VII.2.3. Experimental set-up for piezoelectric measurements.

J. Piezoelectric coefficients determination.

Interferometric technique was utilized to investigate the piezoelectric response from selected specimens. Principles of Doppler heterodyne interferometer are described in paragraph IV.11. The experimental set-up includes Polytec OFV 353 sensor head (laser source and optical system), interferometer controller (Polytec OFV 3001), lock-in amplifier and function generator. The set-up is schematically represented in Fig.VII.2.3. The laser beam is focused on the front electrode of interest. An AC signal of various amplitudes and a frequency of 1 kHz is applied using a computer controlled function generator to corresponding pad to excite surface vibration (due to converse piezoelectric effect). The output signal (surface velocity) from the interferometer controller is measured with the computer operated lock-in amplifier and used for the calculation of surface displacement.

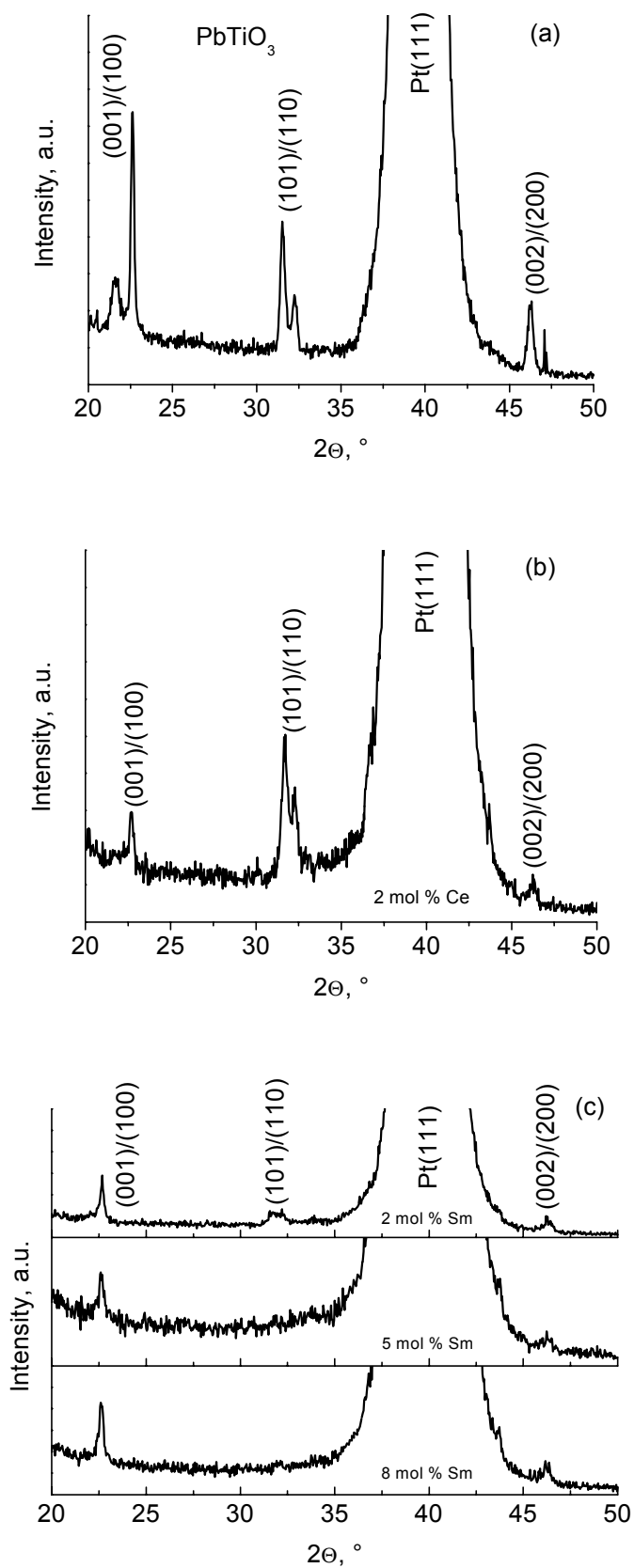
VIII. Experimental results

In the present chapter the results of structural, optical, dielectric, ferroelectric and leakage current properties characterizations of pure and Ln ions substituted PbTiO_3 thin films will be presented. The experimental methods have been described in the previous chapter. Emphasis is put on the effects of nature (atomic number/ionic radius) and concentration of dopants. In the present part of the thesis only a brief overview of the experimental results is given and the reader is referred to the next chapter for the discussions.

The results of pyroelectric and piezoelectric measurements are also presented and discussed in a separate chapter devoted to application aspects of ferroelectric thin films.

VIII.1. Structural properties of rare-earth substituted PbTiO_3 thin films.

XRD analysis in Θ - 2Θ geometry was undertaken mainly to investigate phase content, although some conclusions about preferentially oriented state of the film can also be made. Fig.VIII.1.1 illustrates the Θ - 2Θ XRD patterns of non-doped (a) and Ce, Sm, Dy, Er and Yb doped lead titanate thin films (Fig's VIII.1.1(b, c, d, e and f)). It must be noted firstly, that annealing at 700°C for 5 min leads to the formation of pure perovskite phase in undoped and doped films with dopant concentrations up to 5 mol%, and up to 8 mol% for the particular case of Sm. No second phase inclusions were detected within the sensitivity of the method (5-10%). The most possible pyrochlore phase with a generalized formula $\text{Pb}_2\text{Ti}_2\text{O}_6\text{O}'$, which manifests itself via a broad peak in the vicinity of 30° , was not found for these specimens. However, depending on the concentration and nature (ionic radius/atomic number) of rare-earth ions, doping can result in the stabilization of second phases. Sm doped films show no second phase for all concentrations investigated, whereas the Θ - 2Θ XRD spectra of the films doped with 8 mol % of Dy and Er contain broad peaks (indicated by arrows in Fig's VIII.1.1 (d,e)) attributed to the reflections of the non-ferroelectric pyrochlore phase. The appearance of the pyrochlore phase in doped PbTiO_3 thin films with decreasing radius of doping ions is in agreement with the results reported by Tan *et al.* [122], and is attributed to the lower solubility limit of the elements with smaller ionic radius in the perovskite phase.



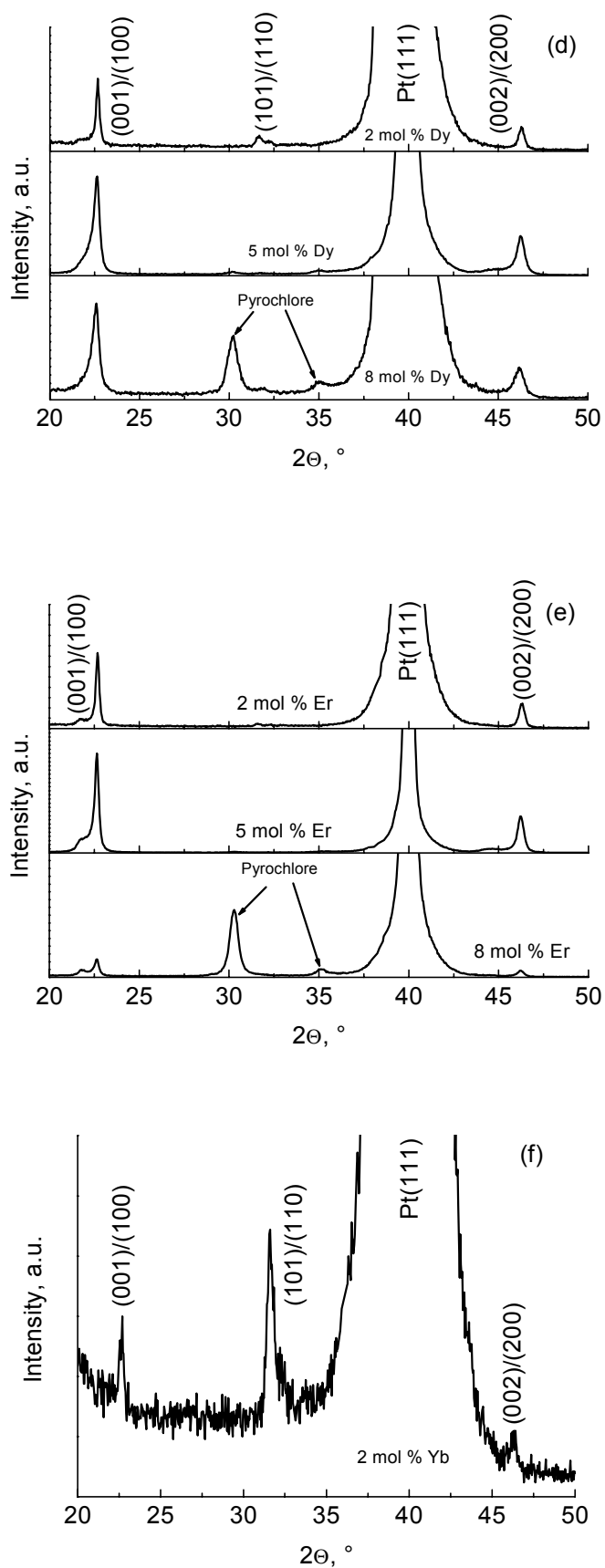
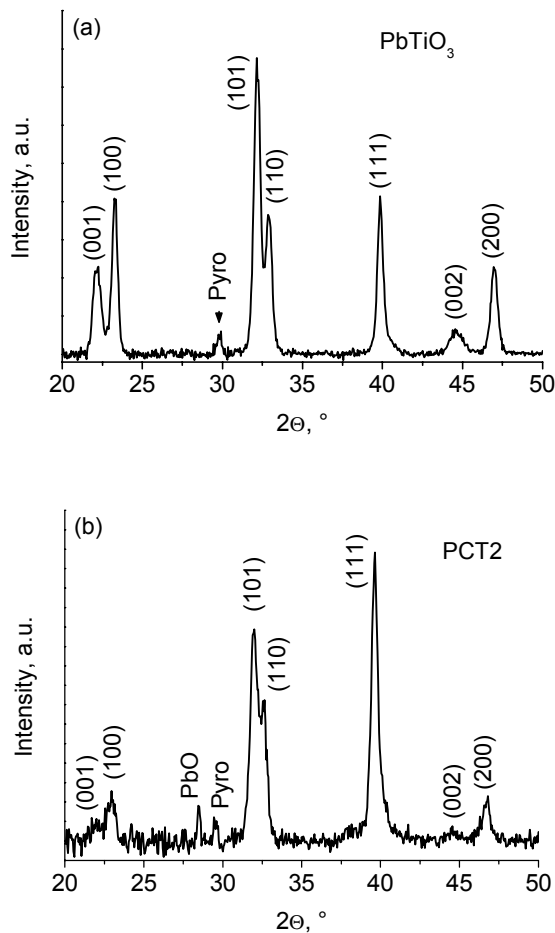
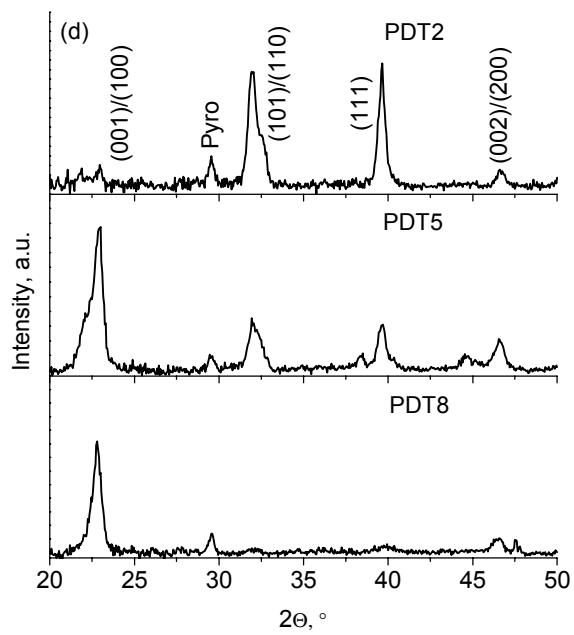
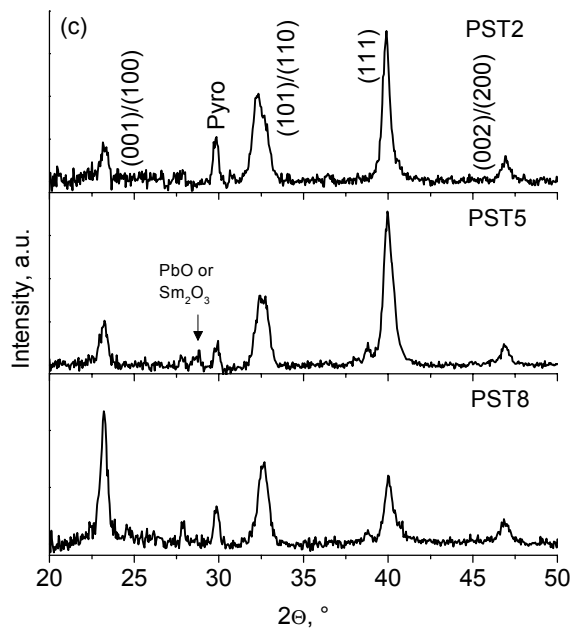


FIG.VIII.1.1. Θ - 2Θ X-ray diffraction patterns of lead titanate thin films: undoped specimen (a), and Ce (b), Sm (c), Dy (d), Er (e) and Yb (f) doped films.

The main problem of X-ray diffractometry of lead titanate based thin films deposited on platinized substrates lies in the (111) perovskite reflection being completely masked with the very intense (111) reflection from the textured platinum bottom electrode in the vicinity of $2\Theta=40^\circ$. This limitation makes it very difficult to have an exact idea about the ratio of peak intensities, i.e. about preferentially oriented state from Θ - 2Θ scans. Thereby only the ratio of (001)/(100) and (101)/(110) main peaks can be discussed. From Fig.VIII.1.1 we can see that the ratio of (001)/(100) and (101)/(110) peak intensities differ from that known for lead titanate powders [149], where the most intense peak is (101)/(110). It seems that depending on the nature of dopant, the thin films may be to some extent preferentially oriented or, otherwise, randomly crystallized. The films doped with 2 mol % of Ce and Yb (Fig's VIII.1.1(b,f)) revealed (001)/(100) and (101)/(110) peak intensity ratios very similar to those found for lead titanate powders. Yet for Sm, Dy and Er doped specimens (Fig.VIII.1.1(c, d, e)) the (101)/(110) peaks are less intense. Furthermore, modification of lead titanate thin films with Sm, Dy and Er with concentrations higher than 5 mol % leads to complete suppression of (101)/(110) reflections, i.e. Sm, Dy and Er doping promotes rather preferentially oriented state of the specimens.





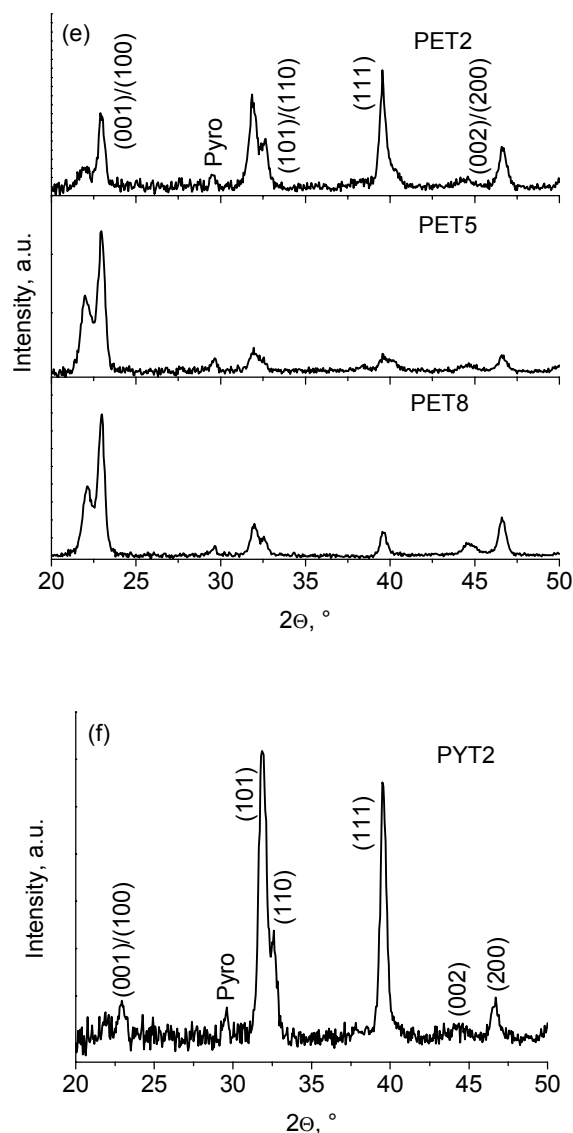


FIG.VIII.1.2. GI XRD patterns obtained for pure (a) and Ce (b), Sm (c), Dy (d), Er (e) and Yb (f) doped PbTiO_3 thin films.

Fig. VIII.1.2 shows the results of GI XRD characterization. It must be stressed that while Θ - 2Θ scans showed only the existence of the perovskite phase in pure and films doped with 2 mol % of Ce, Dy, Er and Yb, and 2-8 mol % of Sm, GI experiments revealed small amounts of second phases along with the perovskite phase for the specimens of all compositions investigated. The spectra obtained by GI geometry clearly show peaks in the vicinity of 29° which were attributed to the pyrochlore phase. Additionally, the modification of the films with Sm and Ce was found to result in the formation of lead oxide (the corresponding peaks are clearly seen on Fig's VIII.1.2 (b,c)). The discrepancy between the XRD data obtained in Θ - 2Θ and GI configurations is caused by the basic difference between

these two techniques. Comparison of the XRD data obtained in Θ -2 Θ and GI geometries will be considered in the next chapter (see "Discussions").

The lattice parameters of the tetragonal lattice, a and c , can be calculated from the angular positions Θ_1 and Θ_2 of any splitted pair of peaks with indices $(h_1k_1l_1)$ and $(h_2k_2l_2)$ using familiar equations

$$a^2 = \frac{\lambda^2}{4} \frac{l_2^2(h_1^2 + k_1^2) - l_1^2(h_2^2 + k_2^2)}{l_2^2 \sin^2 \Theta_1 - l_1^2 \sin^2 \Theta_2} \quad (\text{VIII.1.1})$$

$$c^2 = \frac{\lambda^2}{4} \frac{l_2^2(h_1^2 + k_1^2) - l_1^2(h_2^2 + k_2^2)}{(h_1^2 + k_1^2) \sin^2 \Theta_2 - (h_2^2 + k_2^2) \sin^2 \Theta_1}$$

where λ is the wavelength of X-rays. The tetragonality factor, c/a , is therefore

$$\frac{c}{a} = \frac{l_2^2 \sin^2 \Theta_1 - l_1^2 \sin^2 \Theta_2}{(h_1^2 + k_1^2) \sin^2 \Theta_2 - (h_2^2 + k_2^2) \sin^2 \Theta_1} \quad (\text{VIII.1.2})$$

The tetragonal distortion was determined from XRD GI experiments (Fig. VIII.1.3). Position of high-angular pair of peaks found from Gaussian fitting to the experimental data was taken. It can be seen that the c/a decreases with increasing concentration of doping elements.

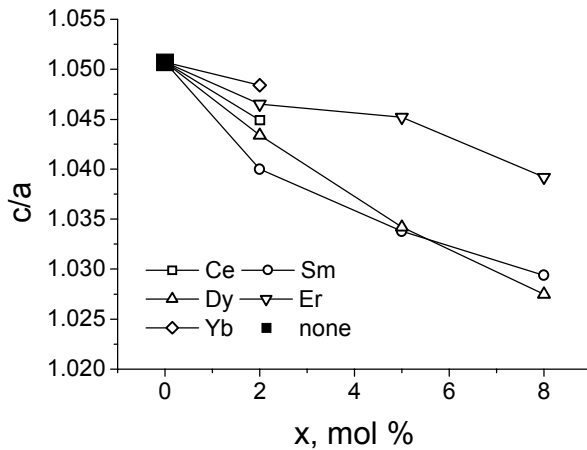


FIG.VIII.1.3. Tetragonal strain, c/a , calculated from GI scans of Ce, Sm, Dy, Er and Yb doped lead titanate thin films. The data are plotted vs. doping level (in mol %).

Fig.VIII.1.4 represents the (100) pole figures measured for pure (a) and doped PbTiO_3 thin films with 5 mol % of Er (b) and 8 mol % of Sm (c). The data demonstrate that doping with various RE's leads to specific effects on the orientation of the films. While Er (small ionic radius) practically has no effect on the texture of PbTiO_3 which shows as strong (100) out of plane orientation, as evidenced by the pole figure in Fig's VIII.1.4(a) and (b), the pole distribution density of Sm (ionic radius greater than that of Er) substituted PbTiO_3 thin film (Fig. VIII.1.4(c)) is found to be mainly concentrated in the ring at approximately $\text{Chi}=54^\circ$

which corresponds to the angle between the [100] and [111] directions of the pseudo-cubic perovskite lattice. No in-plane texture is revealed.

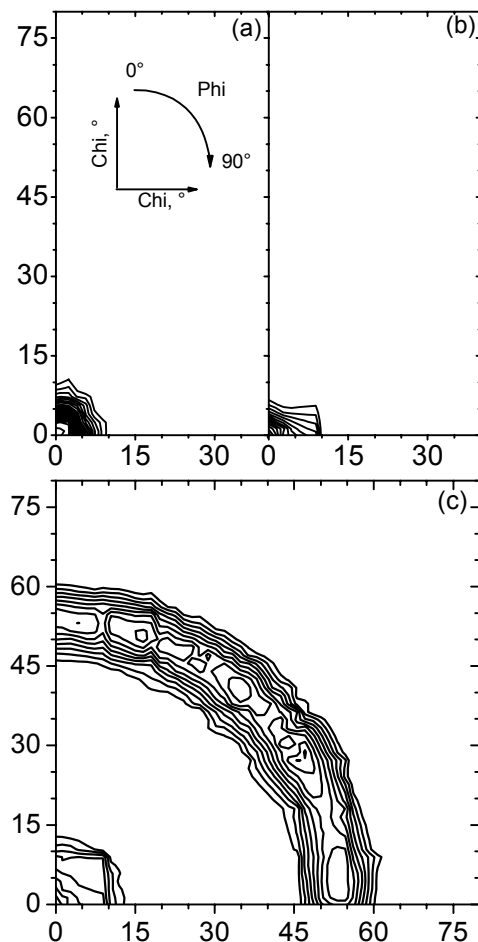


FIG.VIII.1.4. (100) Pole figures obtained for pure (a) and doped PbTiO_3 films: 5 mol % of Er (b) and 8 mol % of Sm (c).

Fig.VIII.1.4 shows that the present films crystallize with the formation of fibre texture, usually found for the majority of thin films deposited onto polycrystalline substrates via sol-gel (a uniform pole density distribution with respect to the azimuthal angle, Φ , indicates the fibre or uniaxial character of the texture). Fig.VIII.1.5 shows (100) FT plots of lead titanate thin films doped with various amounts of Sm and Er. The data obtained for the undoped film are also shown for comparison. It is important to note that already a relatively small concentration of 2 mol% of doping elements dramatically affects the texture of the films, and that a further increase of doping ions concentration did not affect noticeably the preferred orientation of the films (Fig.VIII.1.5).

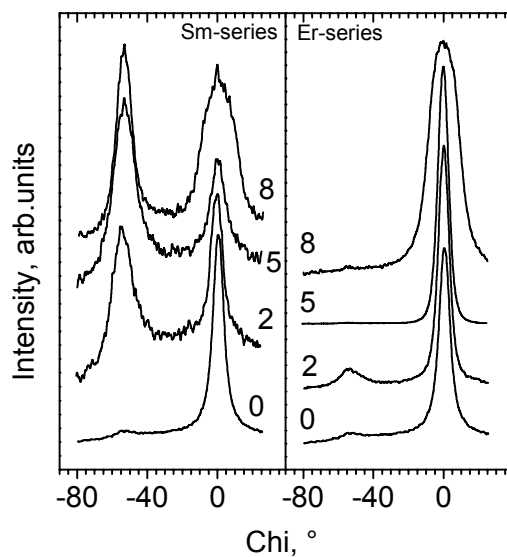


FIG.VIII.1.5. (100) Fibre texture plots obtained for Sm- and Er-substituted thin films. Numbers indicate the doping level (in mol %).

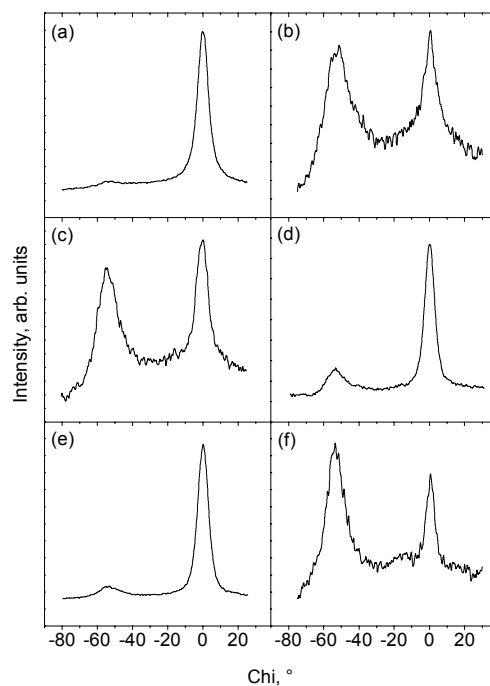


FIG.VIII.1.6. (100) Fibre texture plots obtained for pure PbTiO_3 (a) and 2 mol % of Ce (b), Sm (c), Dy (d), Er (e) and Yb (f) doped thin films.

Fig. VIII.1.6 illustrates the (100) FT plots of pure PbTiO_3 films and films doped with 2 mol % of RE's. The results reported in the present work demonstrate unambiguously that the development of preferred orientations of the films is very sensitive to the type of substituent RE and, to a lesser extent, to the doping level. At the same time, no apparent correlation

between preferred orientation formation and atomic numbers/ionic radii of doping ions (and hence lattice parameters) is found.

VIII.2. Raman scattering from pure and rare-earth substituted PbTiO_3 thin films.

Raman spectra of 2 mol % of RE substituted PbTiO_3 thin films are demonstrated in Fig. VIII.2.1. The modes were labelled according to the nomenclature proposed by Burns and Scott [81,82]. It can be seen that the Raman spectra contain all bands reported for PbTiO_3 bulk materials and thin films by other groups in the frequency range investigated (see paragraph V.3 and references sited therein). The results indicate that the films are well crystallized into the tetragonal perovskite phase.

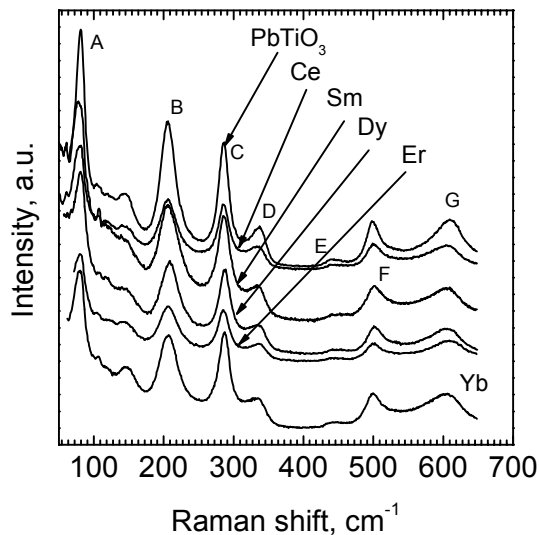


FIG.VIII.2.1. Room temperature Raman spectra of pure PbTiO_3 and doped with 2 mol % of Ce, Sm, Dy, Er and Yb thin films. Raman modes are indicated by letters: A - $E(1\text{TO})$, B - $A_1(1\text{LO})+E(2\text{TO})$, C - B_1+E (silent), D - $A_1(2\text{TO})$, E - $E(2\text{LO})+A_1(2\text{LO})$, F - $E(3\text{TO})$, G - $A_1(3\text{TO})$.

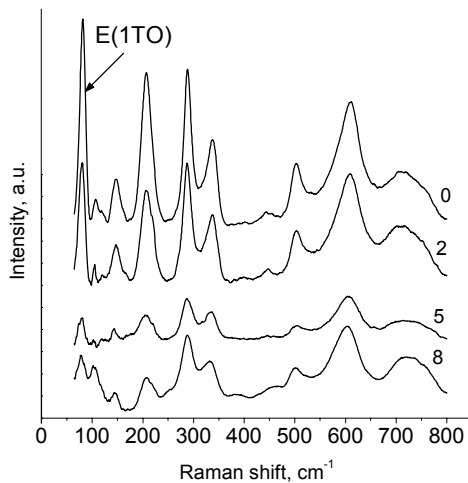


FIG.VIII.2.2. Room temperature Raman spectra of lead titanate thin films doped with various amounts of Er.

It was found that the Raman spectra of the films doped with the elements of lanthanide series are characterised with more feebly marked Raman bands in comparison to the undoped films. This is exemplified in Fig. VIII.2.2 where the Raman spectra obtained for the specimens substituted with 2, 5 and 8 mol % of Er are shown. It must be noted that with increasing Er concentration the lines become broader and their intensities decrease. Furthermore, it can be inferred from the lowering of $E(1TO)$ soft mode frequency that doping with the lanthanide elements leads to weakening of the ferroelectric order ($E(1TO)$ transverse optical phonon is known to be coupled with the displacement of cation within the oxygen octahedron). Fig.VIII.2.3. shows typical dependence of $E(1TO)$ soft modes on doping level found for Dy (a) and Er (b) modified films.

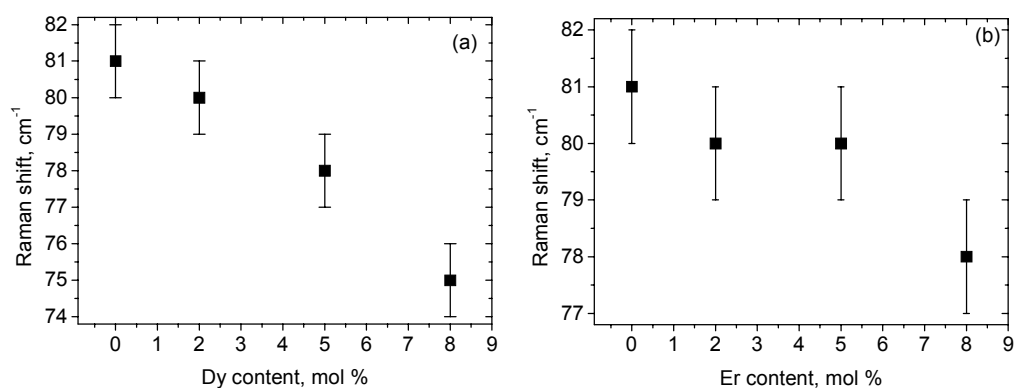


FIG.VIII.2.3. Position of $E(1TO)$ soft modes obtained for Dy (a) and Er (b) substituted $PbTiO_3$ films and plotted vs. doping level.

VIII.3. Refractive indices and extinction coefficients of lanthanide ions doped lead titanate thin films.

Fig.VIII.3.1 shows, how the refractive indices n (a) and the extinction coefficients k (b) of 2 mol % of Ln doped films change with respect to the nature of doping element in comparison to non-doped specimen. A high value of n (2.73 at $\lambda=632.8$ nm) was obtained for pure lead titanate thin film (compare to $n=2.66$ reported for $PbTiO_3$ bulk specimen at the same wavelength [150]). At the same time, the refractive index of our PT film is higher than that obtained by Wood *et al.* [70] (see Table V.1.1) for a film of nearly the same thickness deposited on sapphire substrate. For rare-earth doped $PbTiO_3$ films one can note some decrease in n . Moreover, with exception of Ce, the trend of n to decrease from 2.69 to 2.57 when the atomic number of the element changes from 62 (Sm) to 70 (Yb) can be observed. Furthermore, Ce and Sm doping lead to the reduction of k , whereas Dy, Er and Yb doped

specimens show an increase in the extinction coefficient, in comparison to pure PbTiO_3 . The smallest value of k (2.11×10^{-4}) was found for the film, doped with 2 mol % of Ce.

The refractive indices and extinction coefficients of Sm, Dy, Er and Yb doped films are plotted vs. doping level in Fig. VIII.3.2. For both Sm and Dy some decrease in the index of refraction is observed (Fig. VIII.3.2(a)) which is in contradiction to the results reported by

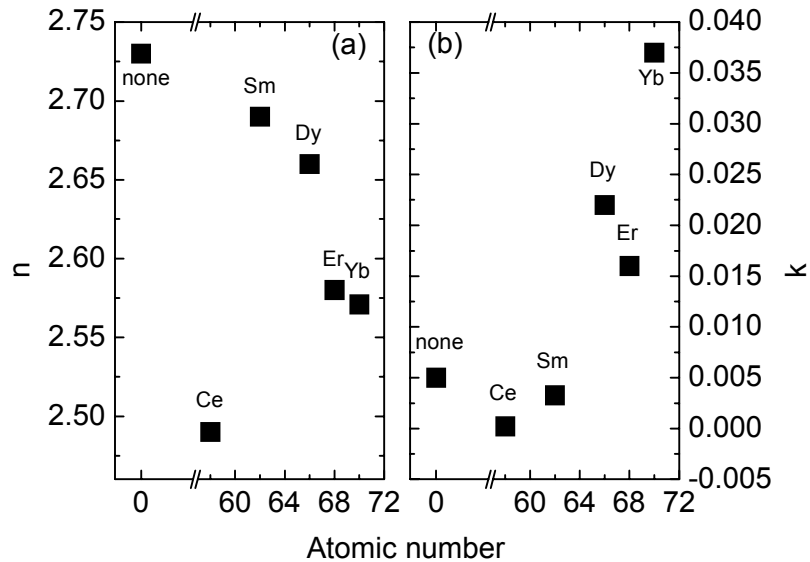


FIG. VIII.3.1. Values of the refractive index n (a), and the extinction coefficient k (b) for PbTiO_3 thin films doped with 2 mol % of lanthanide elements.

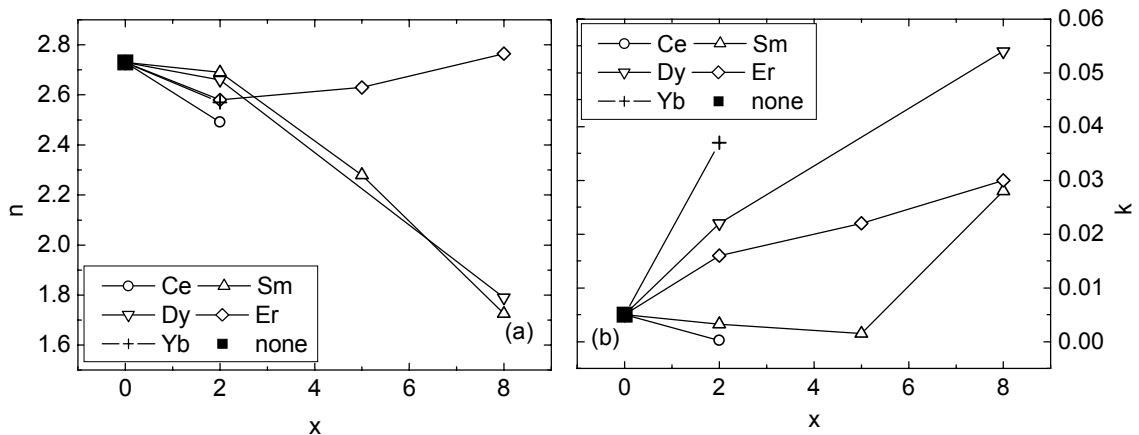


FIG. VIII.3.2. Values of refractive index n (a), and extinction coefficient k (b) of Sm, Dy, Er and Yb doped PbTiO_3 thin films plotted vs. concentration of the doping ions.

Chang and Desu [72] for La and Nd doped PZT thin films. In contrast, doping with 5 and 8 mol % of Er did not produce any noticeable effect. The imaginary part of the refractive index (the extinction coefficient) of Sm, Dy and Er doped films revealed a complex behaviour with

respect to the doping level. For all concentrations investigated, Dy and Er doped films show near linear increase of k when the doping level increases (Fig.VIII.3.2(b)), whereas doping with Sm leads to the opposite effect – the extinction coefficient, which describes damping of the light intensity, was slightly decreased for $x < 5$ mol 5 %. Further increase in Sm content caused an abrupt increase in k .

In order to elucidate the specific effect of Ce on the optical properties of lead titanate thin films, XPS spectra were obtained for lead titanate thin films substituted with 5 mol % of Ce. The results are presented in Fig. VIII.3.3(a,b). The spectra are obtained for as-deposited films and after Ar-ion cleaning of the surface. Fig.VIII.3.3(b) represents the detailed structure of the peak which can attributed to Ce in its oxidation state of +4. The results will be discussed in the following (see "Discussions").

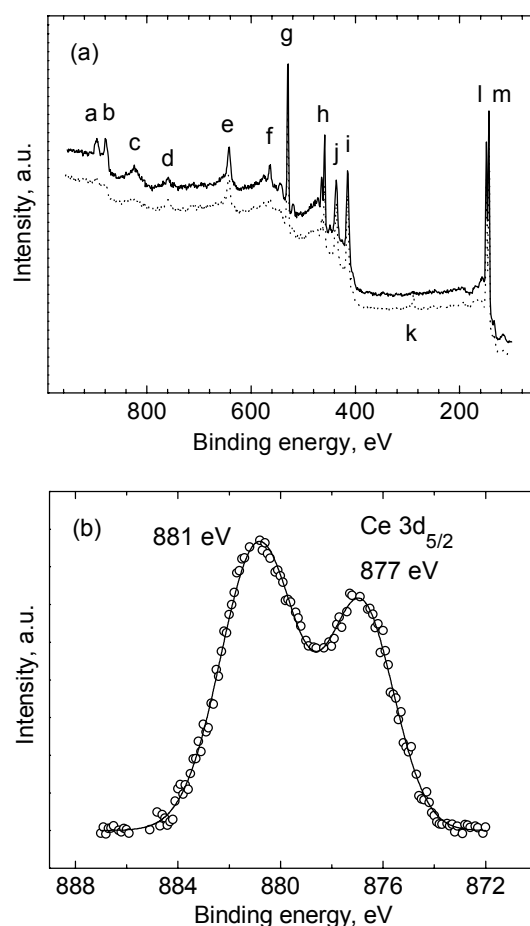


FIG.VIII.3.3. XPS spectra of PbTiO_3 thin film doped with 5 mol % of Ce (a). Here the peaks denoted as: a and b-Ce $3d_{5/2}$, c-Ce Auger, d-Pb $4p_{1/2}$, e-Pb $4p_{3/2}$, f-Ti $2s$, g-O $1s$, h-Ti $2p_{1/2}$, $2p_{3/2}$, i-Pb $4d_{3/2}$, j-Pb $4d_{5/2}$, k-C $1s$, l-Pb $4f_{5/2}$, and m-Pb $4f_{7/2}$. The spectrum of as-deposited film is shown by dashed line. Solid line represents the spectrum taken after cleaning of the surface with Ar ions at 1 kE v , 70 nA for 2 min. Detailed structure of the peak which attributed to $3d_{5/2}$ of Ce is shown separately (b). The experimental data are shown by circles; the result of the Gaussian fitting is represented by the solid line.

VIII.4. Room temperature dielectric properties of pure and doped lead titanate thin films.

The room temperature dielectric properties (ϵ' , $\tan\delta$) of lead titanate thin films doped with Ce, Sm, Dy, Er and Yb were investigated. To analyse doping effects on the dielectric properties, metal-ferroelectric-metal configuration was treated as a conventional plane capacitor, and the dielectric constant was obtained from the measured value of capacitance, C , using:

$$C = \frac{\epsilon_0 \epsilon' S}{d} \quad (\text{VIII.4.1})$$

ϵ_0 is the dielectric permittivity of free space, S the area of the pad and d the film thickness (ellipsometric). Ten pads were measured for each specimen in order to estimate the error. Fig.VIII.4.1 shows, how the dielectric properties of PbTiO_3 thin films correlate with the

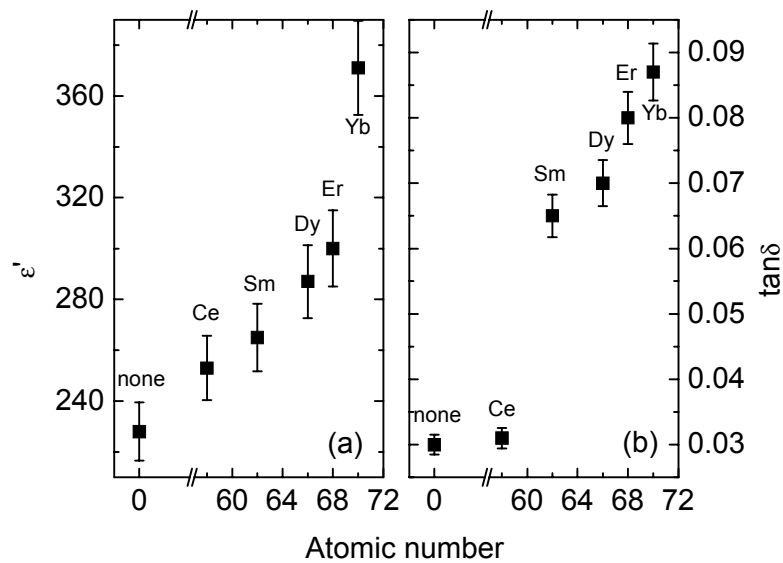


FIG.VIII.4.1. Room temperature dielectric constant, ϵ' (a), and $\tan\delta$ (b) of lead titanate thin films doped with 2 mol % of Ln-elements. Measurements were conducted at 1 kHz with the amplitude of ac signal 50 mV_{p-p}.

nature of dopant for a doping level of 2 mol%. We must note that irrespective of the atomic number of lanthanide element, both the dielectric constant and loss tangent increase in comparison to pure lead titanate thin film. Furthermore, the value of ϵ' and $\tan\delta$ correlate with the atomic number of dopant. It can be seen that both ϵ' and $\tan\delta$ increase smoothly from 228 and 0.03 respectively for pure PbTiO_3 up to 371 and 0.087 for the specimen doped with 2 mol % of Yb. The dielectric properties of Ce, Sm, Dy, Er and Yb doped specimens are plotted

vs. doping level in Fig.VIII.4.2 (see Fig.VIII.4.1 for the error bars). For doping element concentrations up to 5 mol % it can be noticed that ϵ' generally increases with increasing doping level. Higher concentrations lead for Sm and Er doped films to lower ϵ' whereas the values of Dy doped films continue to increase. The loss factor is found to increase in the case of Sm and Er doped samples for concentrations lower than 5 mol % and decrease for concentrations higher than 5 mol %. Dy substituted films show a maximum of $\tan\delta$ at $x = 0.02$ (2 mol %).

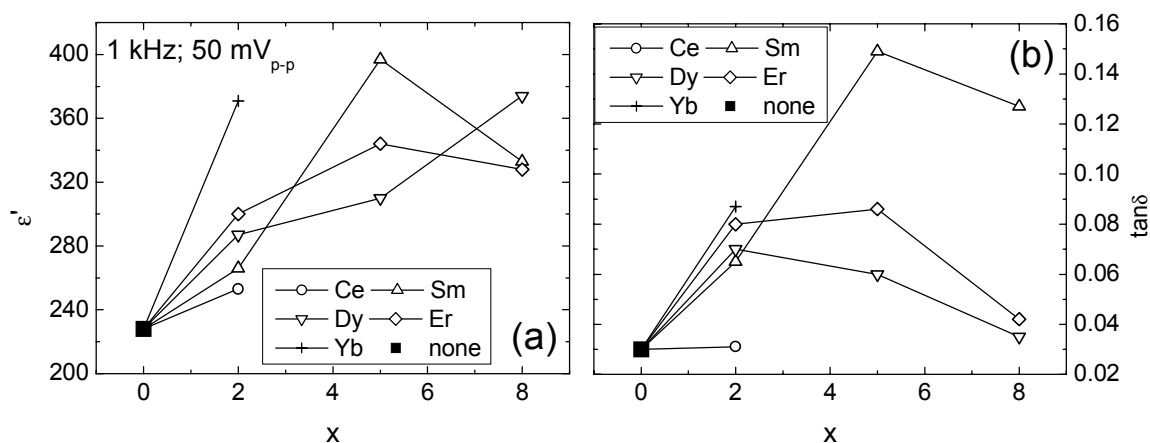


FIG.VIII.4.2. ϵ' (a) and $\tan\delta$ (b) of lead titanate thin films doped with Ce, Sm, Dy, Er and Yb plotted vs. doping level, x (given in mol %).

VIII.5. Effect of lanthanide ions doping on the ferroelectric-paraelectric phase transition temperature.

The temperature dependence of the small signal dielectric properties of pure and Ce, Sm, Dy and Er doped PbTiO_3 thin films were characterized on cooling at various frequencies and 50 mV_{p-p} driving signal. $\epsilon'(T)$ dependencies of all specimens investigated have shown characteristic maxima which are attributed to the paraelectric-to-ferroelectric phase transition. The experimental results are presented in Fig.VIII.5.1. The values of T_C were obtained from the positions of the maxima of the $\epsilon'(T)$ curves. No frequency dependence of T_C was found (nonrelaxor-type) for all doping elements and concentrations. Fig.VIII.5.2 shows that T_C correlates with the atomic number of doping elements (2 mol % doping level). It must be stressed firstly that non-doped PbTiO_3 thin films (Fig's.VIII.5.1 and VIII.5.2) revealed paraelectric-to-ferroelectric phase transition at a much lower temperature than that reported for bulk specimen (compare T_C (PbTiO_3 ceramics) = 490°C [p.12 in ref.8] vs. 450°C, found for our film). Generally, doping with lanthanide elements leads to a smooth decrease of T_C with increasing atomic number. The dependence of T_C on doping level is shown in

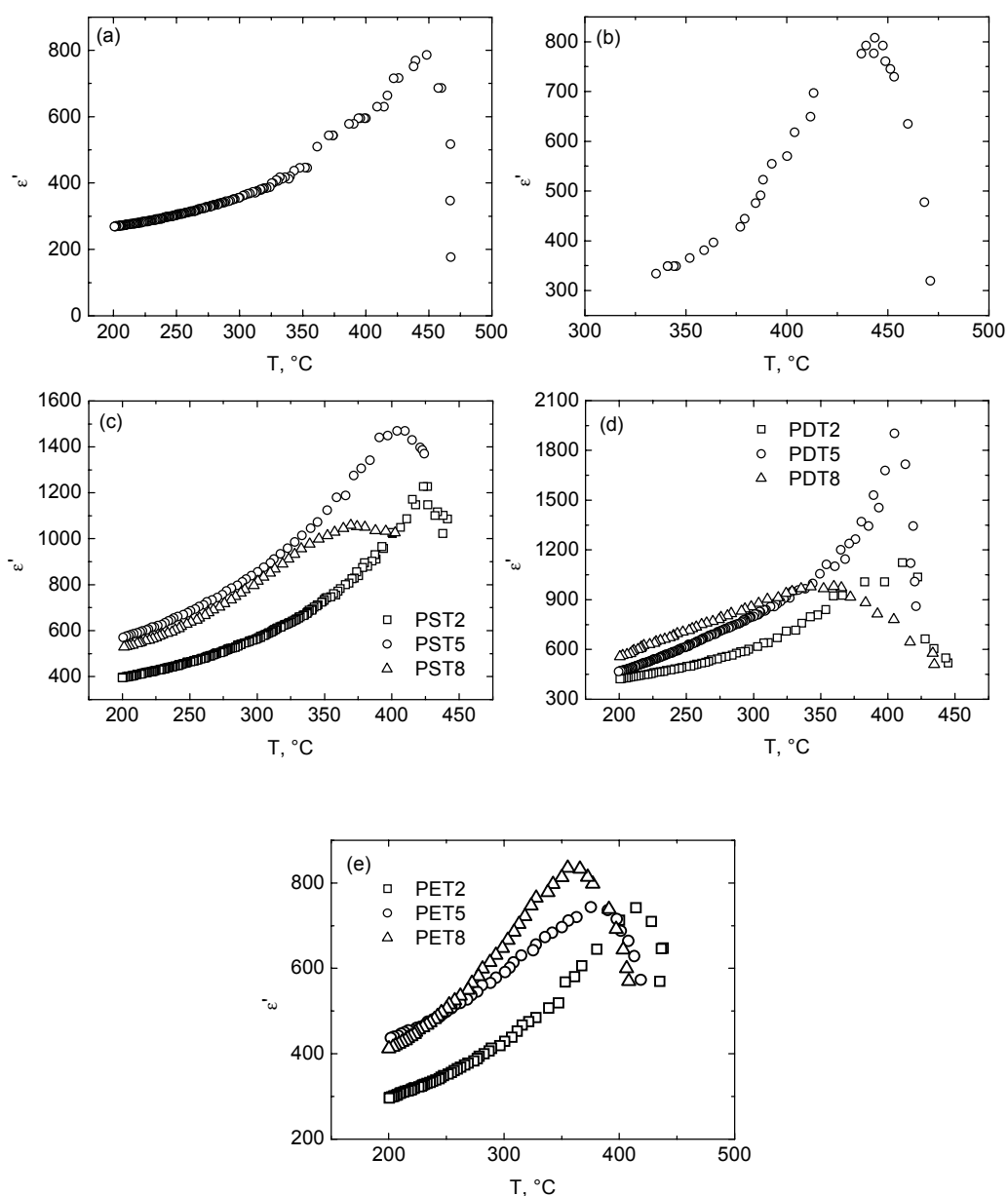


FIG.VIII.5.1. Temperature dependent dielectric constant of non-doped PbTiO_3 thin film (a), and doped with Ce (b) (2 mol %), Sm (c), Dy (d) and Er (e), measured on cooling with the amplitude of AC driving signal 50 $\text{mV}_{\text{p-p}}$ and frequency 1 kHz.

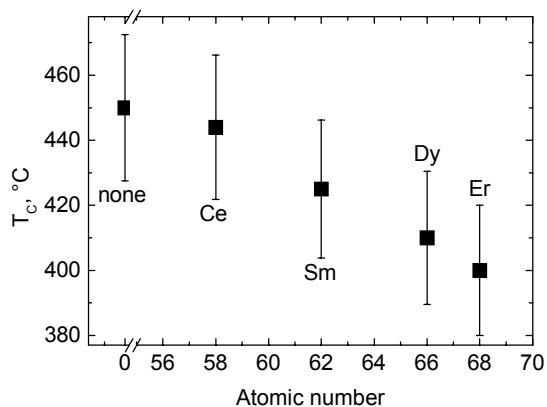


FIG.VIII.5.2. Curie transition temperature of lead titanate thin films, doped with 2 mol % of Ce, Sm, Dy and Er. Measurements were performed on cooling with the amplitude of driving signal 25 mV.

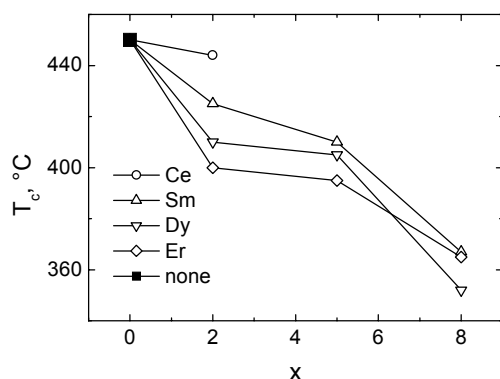


FIG.VIII.5.3. Curie transition temperature of Ln ions doped specimens, plotted vs. doping level.

Table VIII.5.1. Curie transition temperature of lanthanide elements doped PbTiO_3 thin films obtained from $\epsilon'(T)$ measurements.

dopant	none	Ce	Sm	Dy	Er
concentration, mol %					
0	450	-	-	-	-
2	-	444	425	410	400
5	-	-	410	405	395
8	-	-	367	352	365

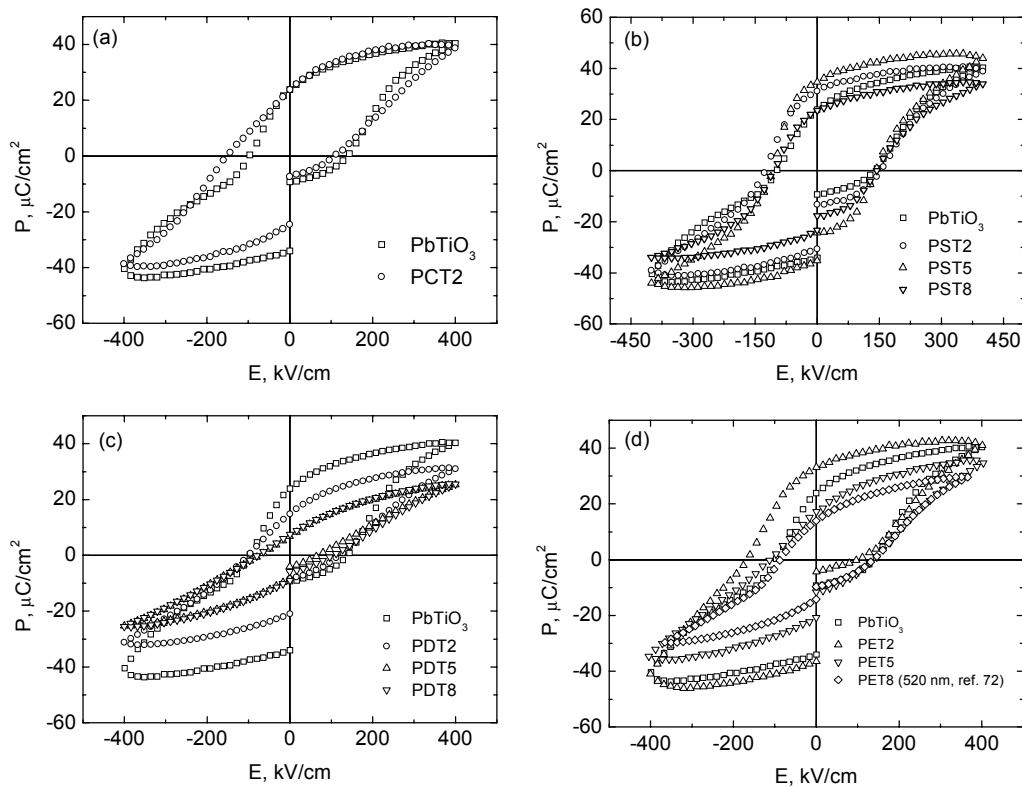


FIG.VIII.6.1. P - E hysteresis loops measured for PbTiO_3 thin films doped with 2 mol % of Ce (a) and 2, 5 and 8 mol % of Sm (b), Dy (c) and Er (d). The hysteresis characteristics were acquired at room temperature with square pulses modulated with time 0.13 ms.

Fig.VIII.5.3. A continuous decrease in T_C can be seen for the doping elements Sm, Dy, and Er. The values of T_C are summarized in Table VIII.5.1.

VIII.6. Ferroelectric properties of PbTiO₃ films doped with lanthanide ions.

The ferroelectric hysteresis loops of pure and rare-earth substituted PbTiO₃ thin films, obtained at room temperature with a puls time of 0.13 ms are illustrated in Fig. VIII.6.1. In the case of PbTiO₃ thin films the analysis of the results of ferroelectric characterization is more complicated as to compare to PZT thin film, due to high DC conductivity of the former. Conductivity can cause overestimation of the values of the remnant polarization as can be seen on Fig. VIII.6.1. In fact, the ferroelectric hysteresis loop of PbTiO₃ films is strongly misshapen [63,64]. Doping with lanthanide elements leads to compensation of conductivity, i.e. higher resistivity of the films. Furthermore, the remnant polarization mainly decreases with increasing concentration of the lanthanide elements. The values of remnant polarization and coercive field obtained from hysteresis measurements for the specimens investigated are collected in Tables VIII.6.1 and VIII.6.2, respectively.

Table VIII.6.1. Remnant polarization ($P_r^+/-P_r^-$, $\mu\text{C}/\text{cm}^2$) of PbTiO₃ thin films doped with various amounts of Ce, Sm, Dy and Er.

Doping element Concentration	None	Ce	Sm	Dy	Er
0	23.5/NM	-	-	-	-
2	-	23.7/-24.9	31.3/-30.3	15/-21	NM
5	-	-	34.7/-35.4	6.8/-8.7	16.7/-20.7
8	-	-	23.6/-23.7	7.5/-9.1	14/-14.2

Table VIII.6.2. Coercive field (E_C^+ / E_C^- , kV/cm) of PbTiO₃ thin films doped with various amounts of Ce, Sm, Dy and Er.

Doping element Concentration	None	Ce	Sm	Dy	Er
0	136.9/-100.1	-	-	-	-
2	-	111.4/-149.6	155.7/-125.9	121/-101	NM
5	-	-	143.8/-107.0	68/-72	140.3/-110.5
8	-	-	145.5/-103.6	106/-78	138/-87.2

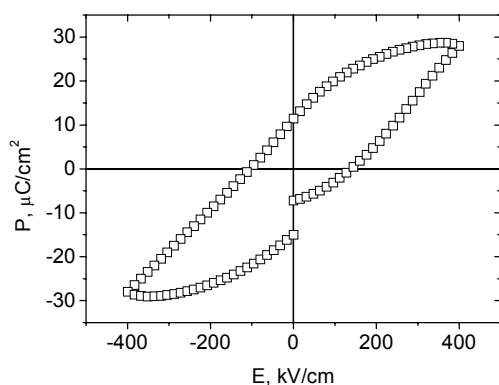


FIG.VIII.6.2. Ferroelectric hysteresis loop of PbTiO_3+5 mol % Er thin film (195 nm thickness) deposited on LNO bottom electrode.

Fig.VIII.6.2 exemplifies the room temperature P - E characteristic obtained for lead titanate thin film doped with 5 mol % of Er and deposited onto LNO bottom electrode. Utilization of lanthanum nickel oxide as the bottom electrode material lead to poorly saturated ferroelectric hysteresis loop (as to compare to that measured for the film of the same composition deposited on Pt, Fig.VIII.6.1(d), and low remnant polarization. The results obtained will be discussed in details in the next chapter.

VIII.7. Thickness effects and contribution of interfacial bottom electrode-thin film layer into small signal dielectric properties of doped lead titanate thin films.

The capacity of PET5 thin films was investigated systematically as a function of film thickness and type of the electrode. Correlation of the dielectric constant with the film thickness is a particular feature of dielectric thin films. As already mentioned, various factors, such as stress which could be developed during high temperature treatment of thin films and subsequent cooling through Curie temperature, chemical interaction between film and electrode material may lead to the formation of interfacial zones characterized by dielectric properties different from those of the interior parts of the film (see paragraph V.4 and references sited therein). According to the widely accepted model of metal-ferroelectric-metal structure, the whole structure is treated as a ferroelectric bulk capacitor with a capacity C_b in series with an interfacial capacitor between the electrode and ferroelectric bulk with a capacity C_i . It is assumed that (i) interfacial (disturbed) layer is characterized with smaller dielectric constant compared to that of the interior part of the film and (ii) the interfacial layer is thin compared to the whole thickness of the capacitor. The measured capacity C of the MFM structure can be expressed as follows [93]:

$$\frac{1}{C} = \frac{1}{C_b} + \frac{1}{C_i} = \frac{d}{\epsilon_{\text{apparent}} \epsilon_0 S} + \frac{1}{C_i} \quad (\text{VIII.7.1})$$

According to this model, the thickness dependence of the reciprocal of the measured capacity must show a linear behaviour. The experimental of the reciprocal of the capacity of PET5 thin films deposited on Pt and LNO bottom electrodes vs. thickness shown in Fig.VIII.7.1.reveal that the model has only a limited applicability.

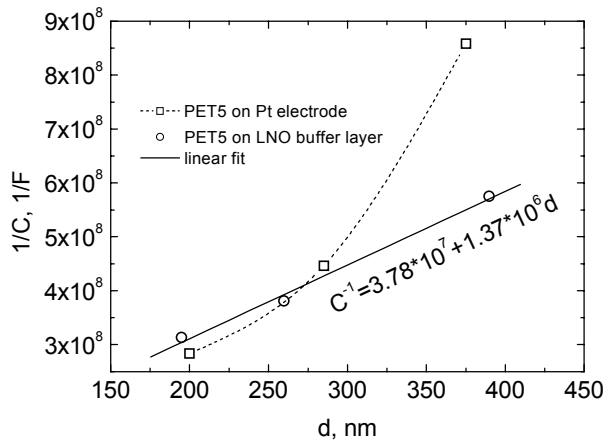


FIG.VIII.7.1. Reciprocal of capacitance of PET5 thin films deposited on platinum (squares) and LNO (circles) bottom electrodes (1 kHz, 50 mV_{p-p}). Data plotted vs. film thickness.

VIII.8. Field-dependent dielectric properties of pure and doped lead titanate thin films.

The room temperature ϵ' - E characteristics obtained for pure and Sm and Er doped thin films are shown in Fig's VIII.8.1 and VIII.8.2. The directions of the DC bias sweep are indicated by arrows.

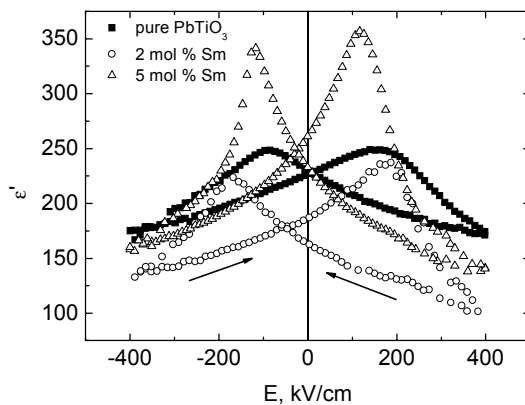


FIG.VIII.8.1. ϵ' - E characteristics, obtained at room temperature for pure and Sm (2 and 5 mol %) substituted film. Frequency and amplitude of ac measuring signal were 5 kHz and 50 mV_{p-p}, respectively.

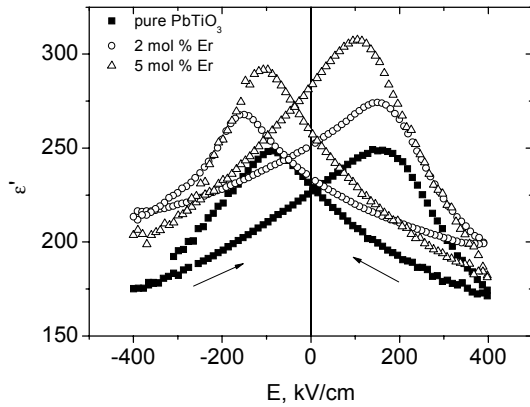


FIG.VIII.8.2. ϵ' - E characteristics, obtained at room temperature for pure and Er (2 and 5 mol %) substituted film. Frequency and amplitude of ac measuring signal were 5 kHz and 50 mV_{p-p}, respectively.

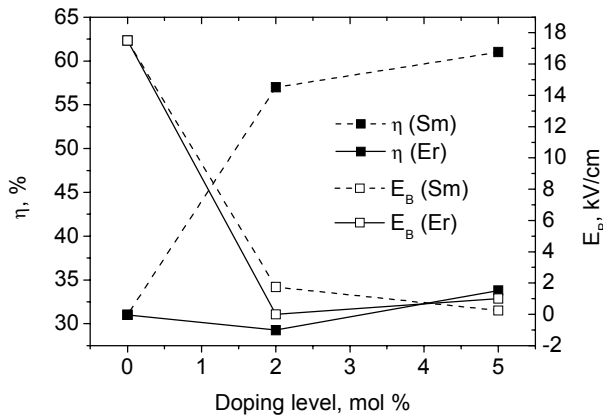


FIG.VIII.8.3. Contribution of domain walls oscillation, η , into the dielectric constant and built-in field, E_B , calculated from data presented in Fig's VIII.8.1 and VIII.8.2.

The “butterfly”-like shape of ϵ' - E plots is the characteristic of ferroelectric material where the relative permittivity reaches its maximum in the vicinity of the coercive field. One can note that the ϵ' - E curves are non-symmetric both with respect to ϵ' and E axes. As mentioned above, non-linear response of ϵ' with respect to the applied DC bias reflects the contribution of domain walls oscillation to the value of the dielectric constant. Considering the crystallites are being in monodomain state at high DC bias (higher than the coercive field), it is possible to estimate the contribution of domains to the measured value of ϵ' in percentage ratio. Assuming the monodomain state of the grains at $E=400$ kV/cm (corresponds to maximum applied field during the experiment), we estimated contribution of domains, η , to ϵ' as $[(\epsilon'_{\max} - \epsilon'_{400}) / \epsilon'_{\max}] \cdot 100\%$ (ϵ'_{\max} was obtained from the part of ϵ' - E curve corresponding to positive DC bias sweep). Furthermore, the value of the built-in field (shift of ϵ' - E along E -axis), E_B , was calculated as $E_B = (E_c^+ + E_c^-) / 2$, where E_c^+ and E_c^- are positive and negative coercive fields, found from the positions of corresponding peaks (Fig's VIII.8.1 and VIII.8.2). The values of η and E_b calculated from ϵ' - E curves of pure and doped (2 and 5 mol % of Sm

and Er) films are represented in Fig.VIII.8.3. A general trend to reduce the built-in field was found for both Sm and Er. At the same time, the contribution of domain walls to the dielectric constant, η , increased for Sm substituted specimens and remained unaffected in Er substituted specimens (Fig.VIII.8.3).

Fig.VIII.8.4 demonstrates the room temperature $\epsilon'-E$ characteristics obtained for 5 mol% of Er substituted films deposited on Pt and LNO bottom electrodes. The positive and the negative coercive fields, the built in field, the maximum values of the dielectric constant (corresponding to E_C) and the contribution of domain structure to the measured value of the dielectric constant obtained from $\epsilon'-E$ characteristics are summarized in Table VIII.8.1. It can be seen that the use of LNO as bottom electrode caused, on one hand, development of a built-in field and, on the other hand noticeable broadening of the peaks.

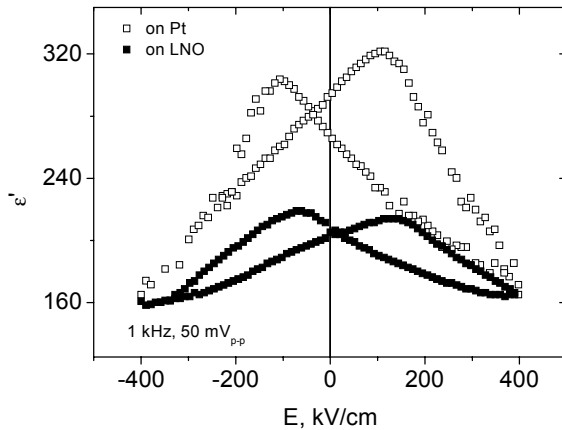


FIG.VIII.8.4. Comparison of $\epsilon'-E$ characteristics of PET5 thin films, deposited on Pt and LNO bottom electrodes. Dielectric constant was measured at room temperature with the frequency of AC signal 1 kHz and the amplitude 50 mV_{p-p}.

Table VIII.8.1. Ferroelectric and dielectric properties, obtained from $\epsilon'-E$ characteristics, shown in Fig.VIII.8.4.

Measured structure	E_c^- , kV/cm	E_c^+ , kV/cm	E_b , kV/cm	ϵ'_m^+	ϵ'_m^-	η , %
Pt/PET5/Pt	-107	108	0.5	304	322	49
Pt/PET5/LNO/Pt	-68	128	30	220	214	26

VIII.9. Voltage-, temperature- and thickness-dependent leakage currents in pure and doped lead titanate thin films.

As already mentioned analysis of the mechanisms responsible for charge transport in dielectric thin films is rather difficult, since different processes can contribute to the measured value of current density in the same range of temperatures or applied voltages. A

comprehensive study including analysis of effects due to temperature, film thickness, doping and nature of electrode can help shed light on the operating conduction mechanisms. In this paragraph the results of the leakage current analysis of pure and doped lead titanate thin are presented. The leakage current density vs. DC bias field are acquired in the temperature range from 40°C to 120°C for films of different thickness deposited on commercial platinized substrates and LNO bottom electrode. Possible mechanisms operating DC conductivity in our specimens are discussed. During the experiment, the DC voltage was applied to the bottom electrode. To facilitate further analysis, absolute values of the leakage current density are taken.

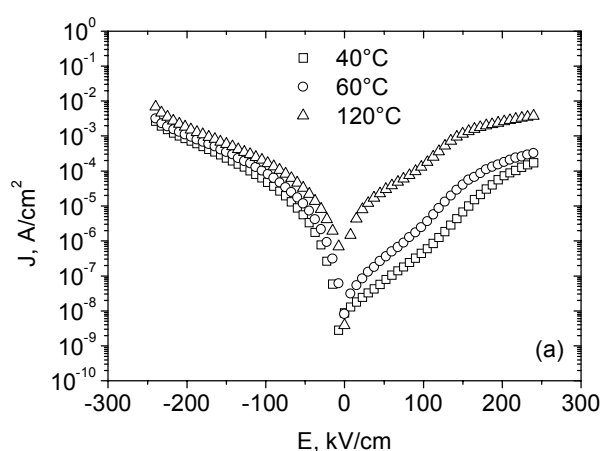


FIG.VIII.9.1 J - E characteristics measured at various temperatures for sol-gel deposited undoped lead titanate thin film ($d=267$ nm).

A. Leakage currents in non-doped lead titanate thin films on Pt bottom electrode.

Fig.VIII.9.1 shows J - E characteristics measured at various temperatures for PbTiO_3 thin film, having a thickness of 267 nm. The leakage current generally increases with increasing temperature. Semi-logarithmic plots of the current density show the rectifying nature of the contact which is observed at lower temperature (difference between positive and negative branches of J - E characteristics is up to two orders of magnitude at 40°C). Moreover, we can see in Fig.VIII.9.1 that the rectifying behaviour of the film disappears as the temperature increases. Aspects related to the asymmetry of current-field characteristics will be considered in the next chapter.

B. Effects of doping on leakage current in PbTiO_3 thin films.

Very similar J - E curves to those, of pure lead titanate (Fig.VIII.9.1) film were obtained for specimens doped with various amounts of Ce, Sm, Dy and Er, Fig.VIII.9.2. The J - E curves of pure PbTiO_3 film is also presented for comparison. In the case of Ce, Sm, Dy and Er doped specimens a lowering of the leakage current density is noted. The films doped with 2 mol % of Yb constitute an exception, and revealed a drastic increase of conductivity.

The leakage current in this specimen could not be characterized due to device limitation. The films substituted with 2 mol % of Ce demonstrated some degradation of the resistance at a positive bias (applied to the bottom electrode) of approximately 200 kV/cm (Fig.VIII.9.2(a)). Furthermore, a rather complex dependence of the leakage current density on the doping level was revealed for the positive branches of the J - E curves obtained for Er substituted films (Fig.VIII.9.2.(c)).

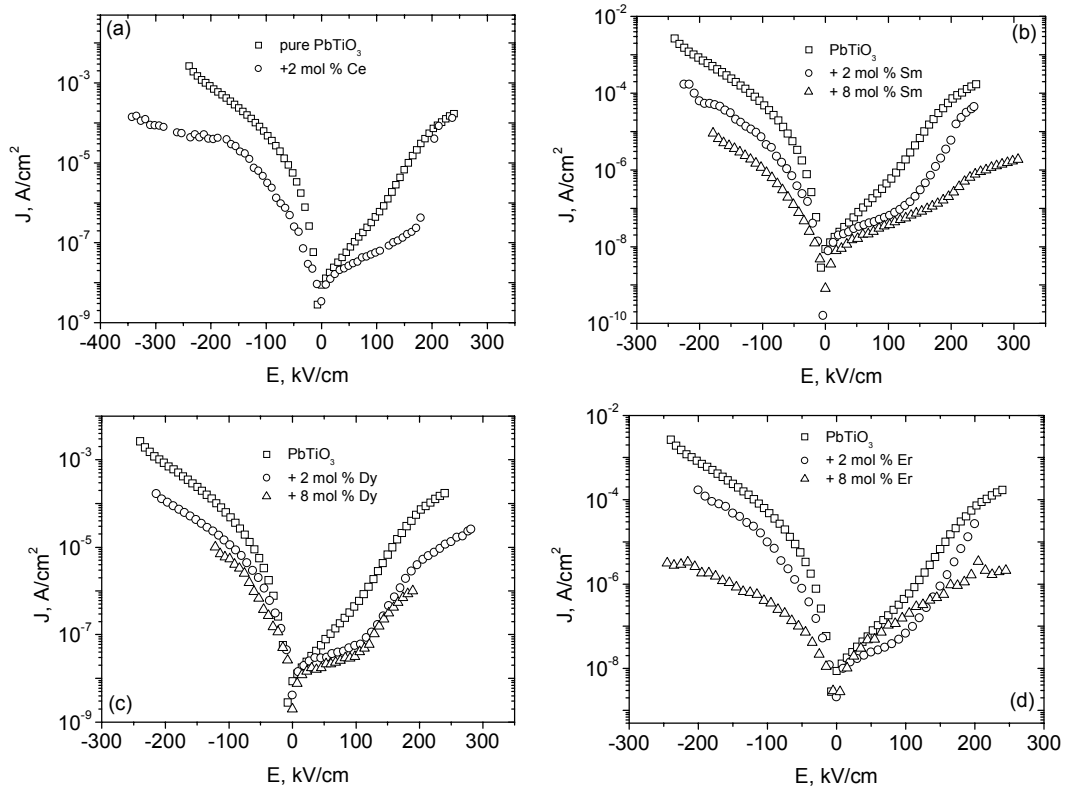


FIG.VIII.9.2. J - E characteristics obtained at 40°C for the films substituted with various amounts of Ce (a), Sm (b), Dy (c) and Er (d).

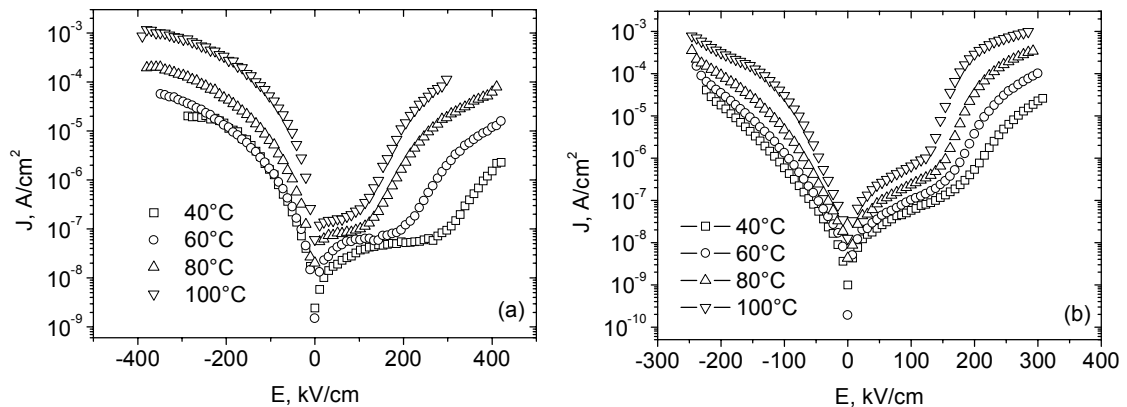


FIG.VIII.9.3. J - E characteristics, obtained at various temperatures for PET5 thin films, deposited on LNO (a) and Pt (b) bottom electrodes.

C. Influence of the electrode material on leakage current of lead titanate films.

For the purpose of investigating the contribution of the nature of the bottom electrode and interfacial properties to the conductivity of ferroelectric thin films, the J - E characteristics of films fabricated on platinum and lanthanum nickel oxide bottom electrodes were compared. Fig's VIII.9.3 (a) and (b) show the J - E curves obtained at various temperatures for lead titanate thin films doped with 5 mol % of deposited on LNO and Pt, respectively. It can be seen that the use of conductive oxide (in particular, LNO) as bottom electrode did not produce noticeable effects on the value of leakage current density, J (see also next section).

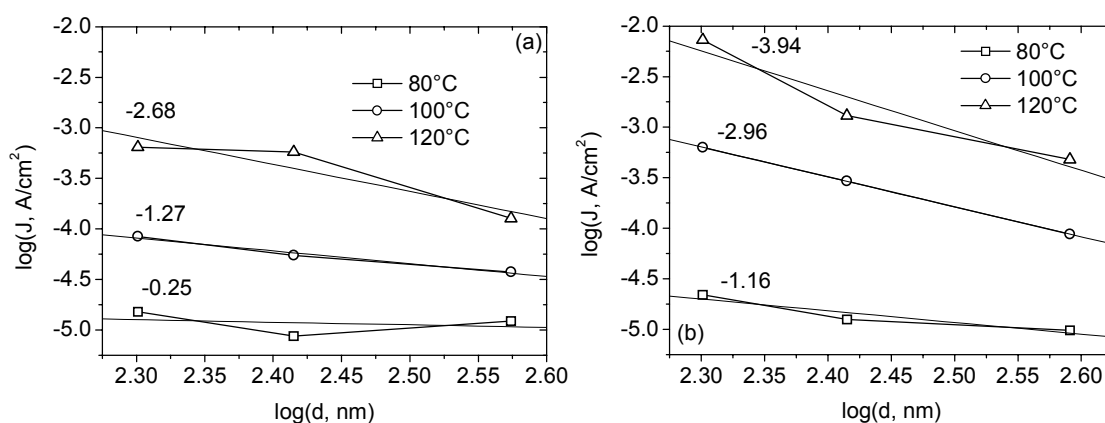


FIG.VIII.9.4. Thickness dependent leakage current density of PET5 thin films measured for films deposited on Pt (a) and LNO (b) bottom electrodes. The data are selected for applied DC bias corresponding to 3V. Experimental results are represented by symbols. Results of linear fitting are shown by straight lines and slopes are indicated by the numbers.

D. Effect of film thickness on leakage current in doped lead titanate thin films, deposited on Pt and LNO bottom electrodes.

The leakage current densities were measured at various temperatures for PET5 films of thicknesses from 200 to 390 nm. Both Pt and LNO bottom electrodes were considered. The results are presented in Fig.VIII.9.4 in log-log plots for an applied DC bias of 3 V. As we already mentioned in the paragraph V.8, the SCLC mechanism is characterized by the specific $J \sim d^m$ relation. The Thickness exponent m can be determined from the slope of J - d double logarithmic plots. It must be noted firstly that for thinner films (200 nm) and lower temperature (data selected for 80, 100 and 120°C are shown) the effect of the nature of bottom electrode can be neglected (see also Fig.VIII.9.3). However, in the case of thicker films the leakage current density is lowered by the use of Pt. The log-log plot of J as function of thickness shows a quasi-linear behaviour for both specimens (solid lines on Fig.VIII.9.4

represent the results of the linear fit), and allows the determination of the thickness exponents, m , from the slopes as shown in the figure.

In the present part of the thesis a brief overview of the experimental results is given and the reader is referred to the next chapter for the discussions.

IX. Discussions

IX.1. Structural properties, phase content and preferred orientation of PbTiO_3 thin films doped with the elements of lanthanide series.

A. Microstructure.

As already mentioned, doping with lanthanide elements lead, generally, to the reduction of the grain size and, as a consequence, surface roughness (Fig.VII.1.6, Table VII.1.1). The effects of doping on grain size in ceramic materials are usually discussed in terms of dopant solubility and/or distribution of doping ions between surface and interior parts of the grain (segregation) [151]. In particular, segregation of impurity ions at grain boundaries can impede grain growth. Although processes responsible for impurity segregation in sol-gel thin films are expected to be impeded due to substantially lower temperatures required for thin film crystallization, impurity segregation may nevertheless takes place because of the small mean diffusion paths involved when the perovskite grains crystallize from the nanocrystalline metastable pyrochlore phase. This explanation may hold for the results found for the films with Sm contents of 2, 5 and 8 mol % and with Er contents of 2 and 5 mol % substituted films (compared to undoped film). In this regard our results agree with those reported by Shannigrahi *et al.* [127] who observed decreasing grain size in Er substituted PZT 60/40 ceramics with increasing Er content (7-8 mol %). Further increase of doping element concentration (8 mol %) leads to an increase of the grain size and surface roughness (Fig.VII.1.6 (d), Table VII.1.1). This specific behaviour of Er doped films is not well understood and has to be investigated in more detail. It may however be speculated that the grain size might have been affected by changes in the morphology of the parent metastable pyrochlore phase due to the higher Er content. In fact, the unstable pyrochlore $\text{Pb}_2\text{Ti}_2\text{O}_6\Box$, where \Box denotes an oxygen vacancy, evolves to the more stable cubic pyrochlore $\text{Ln}_2\text{Ti}_2\text{O}_7$ with increasing Ln content which may cause the morphology change mentioned above.

B. Crystallisation and phase formation.

Fig's VIII.1.1 and VIII.1.2 represent the results of Θ - 2Θ and GI XRD characterization of the specimens prepared, respectively. It was already mentioned that while Θ - 2Θ scans showed only the existence of the perovskite phase for pure and Ce, Dy, Er and Yb (2 mol %) and Sm (2-8 mol %) modified specimens, GI experiment revealed second phases (pyrochlore and, presumably, lead oxide) along with the perovskite phase for all film compositions investigated. The discrepancy in XRD data obtained using different geometries lies in the fundamental difference between GI and Θ - 2Θ X-ray experiments. Due to the relatively high X-ray absorption, GI XRD is surface-sensitive while Θ - 2Θ scan gives an "averaged" through thickness information.

It was reported by many authors [152-155] that the formation of the perovskite phase during sol-gel thin film processing does not occur directly from the amorphous film but via the formation of an intermediate nonferroelectric phase which then transforms to perovskite at elevated temperature. In PbTiO_3 thin film processing, the formation of pyrochlore occurs at approximately 400°C . At temperatures higher than 500°C pyrochlore starts to transform into the perovskite phase. It was shown for tetragonal PZT(20/80) thin films deposited via a sol-gel method on MgO substrates that perovskite grains start to nucleate heterogeneously and isotropically at film/substrate interface [156]. This mechanism of perovskite phase formation usually causes columnar morphology of films (Fig's V.2.1 and V.2.2). At the same time, forming of the nuclei of perovskite phase in the interior parts of the films is also possible. In this case coarse morphology of the specimen is observed (Fig.V.2.3). Exhaustive review of oxygen pyrochlores can be found elsewhere [157]. Kwok and Desu [152] investigated phase transformation in PZT thin films deposited on sapphire substrates by means of X-ray diffraction and transmission electron microscopy (TEM). X-ray diffraction analysis revealed complete phase transformation after annealing at 650°C while TEM revealed the presence of traces of the intermediate phase up to 700°C . In contrast, Seraphin *et al.* [153] showed that PZT film annealed at 450°C consists in perovskite phase. Although TEM observation evidenced that the grains were decorated with second phase particles. Klissurska *et al.* [154] investigated Nb doped PZT thin films annealed at 600 - 700°C . Residual second phase was revealed by means of XRD in the films, doped with 8 mol % of Nb and annealed at a temperature as high as 700°C . There is some discrepancy in the identification of intermediate phase. For example, Calzada *et al.* [155] and Seraphin *et al.* [153] identified this phase as being of fluorite structure and having the stoichiometry PbTi_3O_7 while Klissurska *et al.* [154] report defect pyrochlore of stoichiometry $\text{Pb}_2\text{Ti}_2\text{O}_6$ or $\text{Pb}_2(\text{Zr,Ti})\text{O}_{7-x}$. There is no agreement

about transient phase identification since a standard diffraction file of the pyrochlore phase has not been established [152]. At the same time analysis of literature shows that the temperature range at which complete crystallization of perovskite phase occurs is also not well defined, and depends on processing methods, substrate type, film stoichiometry and presence of impurities.

The appearance of peaks attributed to residual pyrochlore and lead oxide in GI XRD data can thus be explained if we assume that these phases form a thin layer in the near-surface region. This assumption is in agreement with literature data. Vasco *et al.* [158] reported the presence of PbO enriched layer in the near-surface region in PLD (Pb,La)TiO₃ thin films, detected by means of GI XRD while Θ -2 Θ experiment did not show any phases except perovskite. The same authors report PbO enriched surface layers of 10-15 nm obtained by means of Rutherford backscattering and X-ray photoelectron spectroscopy (XPS) investigations. Segregation of PbO in near-surface regions was also confirmed by TEM (transmission electron microscopy) for sputtered Pb(Zr,Ti)O₃ thin films [159]. Li *et al.* [160] reported successful *in situ* preparation of Pb(Zr,Ti)O₃ thin films by reactive sputtering at a temperature as low as 250°. It is important to note that PbO peak in their work was found in Θ -2 Θ configuration. Therefore, it is straightforward to suppose that displacement of Pb during perovskite phase crystallization, its segregation in near-surface region (and to some extent at the grain boundaries) and subsequent oxidation occur in thin films during annealing at elevated (600-700°C) temperatures. In the particular case of Sm doped specimens (see Fig. VIII.1.2(c)), creation of cation vacancies in order to preserve electroneutrality of lattice can cause segregation of lead. At the same time, small peak found for PbTiO₃ thin films substituted with 5 and 8 mol % of Sm in the vicinity of 28° (2 Θ) could also originate from segregation of Sm in near-surface region and its subsequent oxidation and formation of Sm₂O₃, although the low peak intensity did not allow for precise identification of this phases.

C. Domain orientation.

Furthermore, GI XRD spectra reveal peak splitting for all investigated films (in contrast to Θ -2 Θ where no splitting is observed for the Ln-doped films). The peak intensity ratio of the split pair provides information about the abundance of c- or/and a-domains in the films. For example, the results presented in Fig's VIII.1.1(b,c,d,e and f) unambiguously prove that domains in the doped films are mainly aligned in the plane of the substrate [161] due to tensile stress. GI XRD analysis also shows increased intensity diffracted in (00 l) directions in comparison to that in (l 00) directions. This can be explained if we suppose extensive growth

of c-domains (aligned perpendicular to the plane of the substrate) in near-surface region, probably due to stress relaxation. The formation of domains in tetragonal ferroelectric thin films and ceramics of perovskite structure have been extensively discussed in literature [162-169]. Demczyk *et al.* [162] and Ren *et al.* [165] showed that domain configuration is sensitive to grain size and lattice tetragonality. In general, grains with diameters in the range of 300 nm exist mainly in monodomain state. Difference in XRD spectra obtained in Θ - 2Θ and GI geometries can originate from a non-uniform distribution of a- and c- domains and/or preferential orientation (in case of the monodomain state of the grains) through the film thickness.

The results presented here agree with the observation of Choi *et al.* [167] who demonstrated that the abundance of a- or c-domains varies through film thickness, and attributed this to stress relaxation.

D. Preferred orientation.

The results of texture characterization presented in Fig's VIII.1.4-VIII.1.6 demonstrate unambiguously that the development of preferred orientations of the films is very sensitive to the type of substituent RE and, to a lesser extent, to the doping level. At the same time, no apparent correlation between preferred orientation formation and atomic numbers/ionic radii of doping ions (and hence lattice parameters) is found. Therefore, our data cannot be explained from the standpoint of simplified crystallographic orientation relationships between substrate and film similar to those reported by Yamada *et al.* [170]. In their work, they discuss the formation of preferred orientation in chemical solution deposited, RE ions doped bismuth titanate thin films in terms of lattice parameter modification by doping. Increased mismatch between the (111) plane of the Pt bottom electrode and the (00l) plane of the bismuth titanate lattice with decreasing ionic radius of substituent ion is made responsible for specific texture development. Obviously, more complex processes are involved in the development of preferred orientation in sol-gel PbTiO₃ films. In fact crystallization of sol-gel processed films can be influenced by many factors, e.g. sol chemistry, concentration of nucleation agents (dust particles, substrate surface topography and chemistry, etc.) and thermal history, so that microstructure control is difficult to achieve. Because we were aware of all these factors, the different films and corresponding measurements were repeated, and the results obtained were reproducible in the range of experimental accuracy. The present work shows that the (100) fibre texture of PbTiO₃ is little, if at all, affected by elements of small ionic radii, and that elements with high ionic radii affect the PbTiO₃ film texture. Furthermore, the fact that the

PbTiO₃ film obtained is (100) textured, and not the expected (111) which has a better matching with (111)-Pt, suggests the formation of template layers at the film/electrode interface which then control the microstructure during crystallization. The existence of such template layers and their chemistry are difficult to investigate because of competing complex thermodynamic and kinetic processes that take place during the different stages of coating, pyrolysis and annealing. There have been some attempts to investigate these processes but the results are still the subject of controversy [78]: either the investigation methods are not suited [171] or the results cannot be reproduced [78,172]. As an example, Huang *et al.* [172] explain the (111) texture of PZT on (111)-Pt by the formation of PbPt₃ template layer at the interface during early stages of pyrolysis. It is however well known that (100) PZT films also form on (111)-Pt [78,173,174]. Nevertheless, it appears plausible that template layers form during sol-gel processing of lead-titanate based perovskite thin films. Their chemistry and structure seem however to be dominated rather by kinetic than thermodynamic aspects, and this may explain why a variety of microstructures can be obtained for the same or similar film stoichiometries. An example of such microstructures may be found in the work of Es-Souni *et al.* [78, 173] and Brooks *et al.* [174]. Returning to the present work we can try to explain the results by speculating that Er and Yb might have no effects on the chemistry of a purportedly formed template layer, whereas Sm, Ce and Yb might have been affecting its chemistry and structure which would explain the formation of specific textures. Another possible explanation can be proposed considering peculiarities of the sol-gel method. Since this method is not an *in situ* deposition technique, the crystallization of the final perovskite occurs by the nucleation and growth on intermediate metastable phases [173 and discussion above]. In the particular case of lanthanide substituted lead titanate thin films, the lanthanide-based Ln₂Ti₂O₇ and defect lead-based Pb₂Ti₂O₆ pyrochlores crystallize from the amorphous matrix prior to (Pb,Ln)TiO₃ perovskite formation [175]. Therefore, it is reasonable to suppose that the orientation of the perovskite nuclei and final preferred orientation of the film are determined by the chemistry and crystallographic properties of specific intermediate compounds. Unfortunately, in the case of sub-micron thick films, precise phase identification (especially for multi-phase systems) is very difficult to perform. Nevertheless, the combination of appropriate techniques like X-ray photoelectron spectroscopy and GI XRD in the early stages of coating and film formation may help in elucidating factors responsible for texture formation in sol-gel processed films, and until these experiments have been done, the explanations above remain questionable.

IX.2. Raman scattering from pure and lanthanide ions doped PbTiO₃ thin films.

Results of Raman characterization of the specimens prepared are shown in Fig.'s VIII.2.1-VIII.2.3. As already mentioned, the Raman spectra presented in Fig.'s VIII.2.1 and VIII.2.2 show that the films crystallize in the tetragonal perovskite phase and that all Raman active modes presented in the frequency range investigated are found in the spectra. At the same time, some features peculiar to perovskite-type thin films are noted.

A. Undoped PbTiO₃ thin film.

The Raman spectrum measured for pure PbTiO₃ thin films is characterized by some broadening of the bands compared to those of single crystal (see paragraph V.3 and references therein). This effect is attributed to a high degree of disorder due to the presence of point defect (presumably near grain boundaries). Stress and incorporation of ions of differing radius result also in phonon lifetime broadening [84]. The shift of the phonon frequency of the films to lower values is thought to be similar to the effect of hydrostatic pressure in bulk ceramics. Taguchi *et al.* [84] compared Raman mode positions obtained for bulk ceramics under hydrostatic pressure and radio-frequency magnetron sputtered PbTiO₃ thin films. The position of the soft mode reported for their film (80 cm⁻¹) corresponds to that found for ceramic under a hydrostatic pressure of approximately 1.4 GPa. A very close value is obtained in the present work for undoped film.

B. PbTiO₃ thin films doped with rare-earth elements.

Qualitatively, the Raman bands become broader and more feebly marked for doped films (Fig.'s VIII.2.1 and VIII.2.2) indicating weakening of ferroelectric order. Additionally, doping with RE's was found to reduce slightly the frequency of the soft mode. Fig.IX.2.1 shows squared frequency of *E*(1TO) transverse optical phonon obtained for Dy and Er doped films and plotted vs. doping level. The data reported for (Pb,La)TiO₃ ceramics [176] are also shown for comparison. We can see that the softening effect is weaker for elements having smaller ionic radii (1.36 Å, 1.187 Å and 1.159 Å are 12 coordination number ionic radii of La³⁺, Dy³⁺ and Er³⁺, respectively [125,177]). From XRD data, the dependence of *c/a* on Er concentration found for Er doped films [76] enabled us to predict the appearance of the cubic phase at room temperature for doping levels corresponding to 15-20 mol %. Considering the dependence of soft phonon squared frequency on Er content as plotted below does not allow to make such predictions, probably because of a complex dependence and/or insufficient data points.

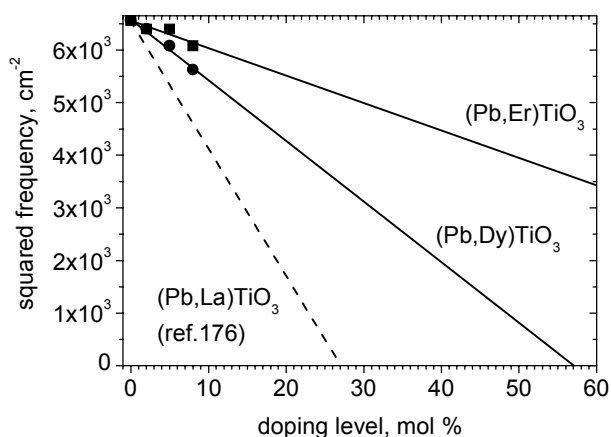


FIG.IX.2.1. Squared frequency of $E(1TO)$ transverse optical phonon of Dy and Er substituted films. Least square linear fit results to the experimental data are shown by the solid lines. Results reported by Tavares *et al.* [176] for $(Pb,La)TiO_3$ ceramics are given for comparison (dashed line).

IX.3. Refractive indices and extinction coefficients of lanthanide ions doped lead titanate thin films.

It is known that visible light interacts with matter via the polarizability of the valence electrons [178]. Following Hench and West [179], the index of refraction depends on the polarizability of the material, which in turn, is determined by the sum of ionic refractions R_i . In crystal compounds, the value of R_i depends upon: i) the electronic polarizability which correlates in a complicated manner with electronic configuration, ionic radii and amount of valence electrons; ii) the coordination number of the ion; iii) the polarizability of the first neighbour ions; iv) the field intensity z/l^2 where z is the oxidation state of the ion and l the distance of separation. Very probably, considering the effect of rare-earth elements doped lead titanate some of the factors may be neglected. In fact, partially filled $4f$ valence levels of Ln-elements are shielded from the external field by $5p^2$ and $5p^6$ states. In this case it is assumed that rare-earth elements will affect the optical properties of the films investigated mainly through the polarizability of the valence shells and the field intensity (z/l^2). Therefore, it is expected that the index of refraction would change smoothly while the electronic configuration changes from $[Xe]4f^15d^16s^2$ (Ce) to $[Xe]4f^{14}6s^2$ (Yb). Moreover, it is known that the polarizability, α , of Ln^{+3} ions decreases linearly with increasing atomic number. Polarizabilities and radii of lanthanide (Ln^{+3}) ions are shown in Fig.IX.3.1 [180]. In the present investigations it is dealt with Pb^{2+} , an ion with high polarizability ($\alpha=6.8 \text{ \AA}^3$) being substituted with ions having smaller polarizability (it is assumed that lanthanide ions replace lead in A-sublattice; the validity of the assumption will be discussed in the following

paragraphs). The dielectric constant of crystals can be expressed in terms of polarizability of its constituent ions [180], α_i , through:

$$\varepsilon = 1 + \left[\frac{(\sum N_i \alpha_i / \varepsilon_0)}{(1 - \gamma \sum N_i \alpha_i / \varepsilon_0)} \right] \quad (\text{IX.3.1})$$

where N_i is the number of atoms of species i per unit volume and γ is the Lorentz factor. In the optical frequency range, the dielectric constant is equal to the squared index of refraction

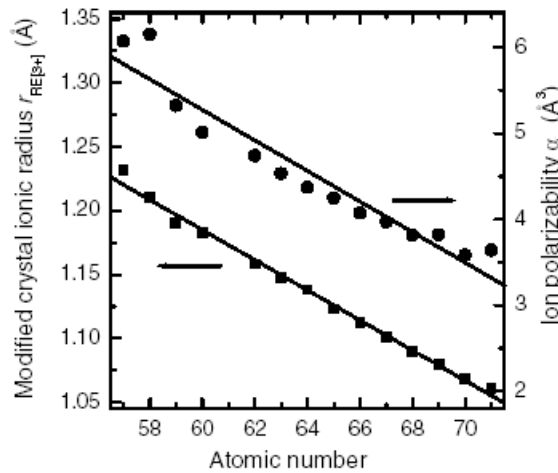


FIG.IX.3.1. Radii and polarizabilities for +3 rare-earth ions, plotted vs. atomic number [180]

($n^2 = \varepsilon$). Therefore, it is reasonable to expect a decrease in the refractive index of lanthanide ions doped films with increasing dopant atomic number. This assumption is to some extent consistent with the experimental results presented in paragraph VIII.3. The particular behaviour of Ce doped films (Fig.VIII.3.1(a)) requires, however, some additional discussion. A possible explanation of such behaviour can be proposed from the point of view of specific oxidized state of Ce. It is well known that unlike the usual +3 oxidation state, peculiar to the elements of Ln-series, Ce may also appear in the oxidation state +4. To our knowledge, the experimental investigation of the oxidation state of Ce in Ce-substituted lead titanate thin films is still lacking. In the present work, Ce doped PbTiO_3 film is investigated by means of X-ray Photoelectron Spectroscopy (XPS) since the position of XPS peaks is sensitive to oxidized states of ions via peak position shifts. Fig.VIII.3.3(a) shows XPS spectra of PbTiO_3 thin film doped with 5 mol % of Ce. The dashed line represents the spectra taken for as-deposited film. The XPS spectra of the same sample measured after Ar ion cleaning at 1 keV, 70 nA for 2 min is shown by solid line. The Ar ion cleaning has not produced noticeable modification of the spectra. Only the 1s peak of C, attributed to surface contamination, disappeared. The detailed structure of the peak designated Ce $3d_{5/2}$ is shown separately in

Fig.VIII.3.3(b). The values of binding energy obtained by Gaussian fitting (881 and 877 eV) indicate the presence of Ce in +4 oxidation state [181]. As discussed by Majumder *et al.*, [129], it is very probable to find Ce in both +4 and +3 oxidation states in the case of PZT thin films. Thus Ce ions can be distributed between A- and B-sites of the perovskite lattice: Ce³⁺ substitutes lead and imparts donor-type properties to the host material while Ce⁴⁺ substitutes titanium due to smaller ionic radius and acts as isovalent impurity. However, the XPS peaks corresponding to 4+ oxidation state of Ce may also arise from surface and grain boundary segregation of CeO₂, and XPS induced modification of Ce oxidation state have been also considered [124]. Although these considerations make an interpretation of the XPS results difficult, the optical and leakage current properties (the latter will be discussed in the following) rather militate in favour of the presence Ce ions in Ce³⁺ and Ce⁴⁺ oxidation states, and being distributed between A and B sublattices, respectively.

IX.4. Room temperature dielectric properties of pure and doped lead titanate thin films.

The results of the room temperature dielectric characterization (paragraph VIII.4.) can be discussed from the point of view of doping effects on domain wall mobility. It is well known that the dielectric properties of ferroelectric materials are mainly determined by domain wall oscillation under applied AC signal and oscillating domain walls are responsible for unusually high dielectric constant peculiar to ferroelectric materials below their Curie temperature. It was shown [182,183] that dielectric constant ϵ' of ferroelectric thin film can be expressed in terms of Rayleigh equation as:

$$\epsilon' = \epsilon_R + \epsilon_{IR}E \quad (\text{IX.4.1})$$

where ϵ_R and ϵ_{IR} are reversible and irreversible Rayleigh parameters, respectively and E is weak alternating electric field (smaller than E_c). Here the ϵ_R term is due to reversible domain walls oscillation around some equilibrium position while the term $E\epsilon_{IR}$ is responsible for irreversible domain walls movement.

As already discussed, doping with donor elements is compensated by cation vacancies in order to preserve electroneutrality. Donor-cation vacancy combinations are thought to be stable and so not to impede domain wall motion. Furthermore, donor doping compensates for the p -type conductivity inherent to lead containing perovskites through the reduction of oxygen vacancies, and this leads to higher domain wall mobility. Donor elements doped perovskite ferroelectric materials are therefore known to have higher permittivity and loss

tangent than non-doped materials, and the results obtained in the present work (Fig.VIII.4.1) are well in this trend. The increase of the dielectric constants and loss tangents of doped specimens with respect to pure PbTiO_3 can thus be explained in terms of contribution of domain walls oscillation to the small signal dielectric properties, and the observed dependence of ϵ' and $\tan\delta$ on the atomic number of doping element is opaque.

The decrease in ϵ' and $\tan\delta$ for doping levels higher than 5 mol % (Fig.VIII.4.2) may be explained in terms of the appearance (in the case of Er doping) of second pyrochlore phase, which is non-ferroelectric, or (in the case of Sm doping) to segregation effects/formation of second phases at grain boundaries and/or film surface which may act as pinning centres.

IX.5. Effect of lanthanide ions doping on the ferroelectric-paraelectric phase transition temperature.

A. Pure PbTiO_3 .

The dielectric constant and ferroelectric phase transition temperature of ferroelectric thin films are influenced by many factors. First of all, solvent evaporation during thin film deposition and difference in thermal expansion coefficients of the film and substrate can cause the development of stress in the films [97,98]. Value and sign of stress are strongly dependent on thin film deposition condition and type of substrate. Si has rather low value of thermal expansion coefficient ($\text{CTE}(\text{Si})=2.6 \cdot 10^{-1} \text{ }^\circ\text{C}^{-1}$). In turn, thermal expansion properties of lead titanate are very sensitive to the temperature and may vary in wide range (Fig.IX.5.1 [185]) due to presence of structural phase transition. It is widely accepted in the literature [97,98,118] that using Si as the substrate material mainly causes the development of tensile biaxial stress in the ferroelectric film (Pt bottom electrode does not make significant contribution into the resulting stress due to very small thickness (100-150 nm)). Depending on the type of stress, the Curie point can be lowered or increased. In comparison to “stress-free” ferroelectrics, it was predicted that two-dimensional compressive stresses oriented orthogonal to the c polar axis result in an increase in the Curie point, while three-dimensional (hydrostatic) compressive stresses lead to a decrease in the Curie temperature [119]. While two-dimensional stresses can be developed due to difference in the thermal expansion coefficients of the film and the substrate materials, in nano-sized structures, however, compressive hydrostatic stresses can appear during cooling through the Curie temperature owing to the clamping of the individual grain by neighbouring grains. The stress cannot be relaxed by the 90° domain formation probably because of the monodomain state of the grains

[165,184] or the preponderance of 180° domains. Another factor affecting Curie transition temperature of the films is grain size. In particular, Shaw *et al.* [115] showed that $(\text{Ba,Sr})\text{TiO}_3$ (BST) thin films deposited on Si substrates undergo ferroelectric-to-paraelectric phase transition at lower temperature in comparison to BST ceramics. Chattopadhyay *et al.* [121] investigated phase transition in nanocrystalline PbTiO_3 by dielectric measurements, variable temperature X-ray diffractometry and differential scanning calorimetry (DSC). The same effect (lowering of Curie temperature with decreasing particle size) was observed. A pronounced effect was revealed when the particle size was below 100 nm. The results of the present work show that the curie transition temperature of pure lead-titanate thin films is much lower than that reported for lead-titanate ceramics (450°C for PbTiO_3 thin film in comparison to 490°C of PbTiO_3 ceramics [8]). This result can be explained both in terms of stress state and grain size effects (see Fig.VII.1.6 and Table VII.1.1). The results described above show that the mean grain size of lead titanate is approximately 100-140 nm. Therefore it is straightforward to suppose that resulting stress in ferroelectric thin films depends in a complicated manner on structural properties of the films (grain size, preferred orientation), film thickness and deposition conditions.

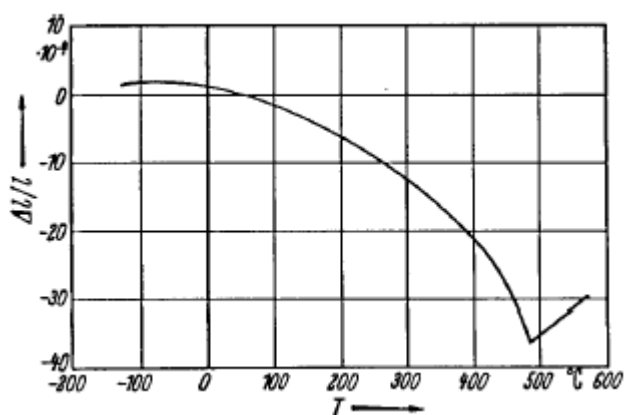


FIG. IX.5.1. Temperature dependence of thermal expansion of lead titanate ceramics [185].

B. Ln-doped PbTiO_3 .

The Curie transition temperature, T_C , was found to depend on the atomic number of the Ln elements, i.e. on the ionic radius. The results show (Fig's VIII.5.2, VIII.5.3 and Table VIII.5.1) that T_C decreases with the atomic number of Ln and concentration which suggest that Ln-doping leads to the weakening of the ferroelectric order (in this regard the data of dielectric measurements agree with the results of structural and Raman characterization), e.g. by decreasing in the tetragonal distortion of the lattice (c/a) (see also Fig. VIII.1.3).

In the previous discussion the lanthanide ions were supposed to replace lead in A-sublattice. In fact, The distribution of Ln-elements between A and B sites in the perovskite

lattice is subject of controversy. The results of dielectric characterization presented here are to some extent in contradiction to those reported by Tan *et al.* [122] and Park *et al.* [125] on Ln-doped PZT ceramics, where T_C was found to increase with decreasing ionic radius of lanthanides in comparison to undoped PZT (Fig.V.7.1). They explained their results in terms of the site occupancy of Ln-ions being changed from A to B with decreasing ionic radius of doping ion. The results of the dielectric characterization, obtained in the present work rather suggest A-site substitution by the elements of Ln-series, although further experiments with rare-earth doped PbTiO_3 ceramics and volume cell calculation are required. Additionally, it can be seen that the Curie point found for doped films does not correlate in a simple manner with the grain size (as expected considering the results reported in [115,121], see above). In fact, T_C was found to decrease continuously for all concentrations investigated, although the 8% Er doped film shows a mean grain size similar to that of the undoped film (Table VII.1.1). Therefore we speculate that the Curie temperature of our specimens is mainly controlled by doping level and that the effect of grain size, in the range of grain sizes obtained, can be neglected.

IX.6. Ferroelectric properties of PbTiO_3 thin films doped with the elements of lanthanide series.

The effects of doping on the P - E characteristics of PbTiO_3 thin films have been described in paragraph VIII.6. Ce, Sm, Dy and Er improve to some extent the shape of hysteresis loops. This demonstrates that lanthanide elements doping leads to reduced DC conductivity of the films especially at higher values of applied field (up to 400 kV/cm, see Fig.VIII.6.1). With respect to technological applications of the films such effect (lowering of conductivity) is rather advantageous because high DC conductivity peculiar to undoped lead titanate complicates poling and increases the risk of break-down. Furthermore, as depicted above, the ferroelectric parameters (remnant polarization and coercive field) correlate, to some extent, with doping level. The data summarized in Tables VIII.6.1 and VIII.6.2 show that with increasing doping level (case of Sm, Dy and Er substituted films) the ferroelectric hysteresis loops become slimmer. The results can be explained in terms of the tetragonality factor modification by doping. As shown above (Fig.VIII.1.3), doping with lanthanide ions results in a significant lowering of c/a factor that is accompanied by the reduction of the resulting dipole moment of the lattice. This can explain the decrease of remnant polarization observed for doped films. Values of remnant polarization obtained for films doped with 5 and

8 mol % of Ln can be considered as the most reliable since contribution of DC conductivity in *P-E* characteristics is minimized for these specimens.

The results of ferroelectric testing obtained for PET5 thin films deposited on LNO electrodes (Fig.VIII.6.2) agree in general with the results reported by other groups for lead based perovskite thin films of various compositions. Chen *et al.* [112] investigated the effect of top and bottom electrode materials on the ferroelectric and fatigue properties of lead zirconate titanate thin films. It is reported that while films deposited on LNO/Pt hybrid electrodes are characterized by higher fatigue resistance, compared to those fabricated on Pt electrode, the latter are reported to have higher values of the remnant polarization. Similar effect of LNO buffer layer between film and Pt bottom electrode was demonstrated by Es-Souni *et al.* [106] for sol-gel fabricated PLZT films with various La contents. It is supposed by many authors (see paragraph V.5 and references therein) that the ferroelectric properties of polycrystalline ferroelectric thin films are to a great extent determined by their morphologies which, in turn, are affected by the substrate structure. However, the results of AFM characterization reported in the present work unambiguously demonstrate that the microstructure of the films of the same composition (PET5) was not crucially affected by the type of bottom electrode (compare Fig's VII.1.6(c) and (h)). Further investigations are required in order to understand the mechanisms responsible for the deterioration of ferroelectric properties of the films fabricated on LNO bottom electrode material.

IX.7. Thickness- and field-dependent dielectric properties of pure and doped lead titanate thin films.

A. Dimensional effects on capacitance.

Reciprocal capacitance of PET5 thin films of different thickness deposited on Pt and LNO bottom electrodes is plotted vs. film thickness in Fig.VIII.7.1. Agreement with the proposed two-layers model can be noted for PET5 thin films deposited on LNO buffer layer. The value of the interfacial capacity was determined for this set of specimens as 26.4 nF from the intercept with the capacity axis. If we assume the thickness of the interfacial layer to be about 10 nm, the dielectric constant of this layer is then about 10 (calculated using (VIII.4.1)). Apparent dielectric constant (bulk value) of the films deposited on LNO bottom electrode was found from the slope of C^{-1} vs. d (Fig.VIII.7.1) as 294. This value is higher than those calculated from the measured capacitances using (VIII.4.1): 251, 276 and 273 for the films of thickness 195 nm, 260 nm and 390 nm, respectively. Comparison of measured values of

dielectric constant with the apparent one clearly demonstrates the deteriorative role of the film-electrode interfacial layer.

At the same time, we must note that the thickness dependence of the reciprocal capacity of the thin films deposited onto platinized Si substrate deviates from the linear behaviour, and rather shows a parabolic dependence. These results imply that the Pt/PET5/Pt/ structure can not be treated as two capacitors connected in series. We speculate that besides the interfacial layer formation, the thickness dependence of the thin film capacitance is determined by the stress state (which is also thickness dependent and relaxes with increasing d) developed during film crystallization. The stress is considered to relax in the films deposited on LNO/Pt electrode probably due to the perovskite structure of LNO, in agreement with the result reported in [113] while in Pt/PET5/Pt structure it remains almost unchanged. It must also be noted that the parabolic behaviour of $C^{-1}(d)$ was found only for lead titanate thin films, where the stress is particularly high due to relatively high room temperature tetragonality factor. A linear $C^{-1}(d)$ dependence was reported for Er doped tetragonal PZT [95].

B. C-V characteristics.

The voltage-dependent dielectric properties were investigated systematically with regard to doping and bottom electrode material effects. Fig's VIII.8.1 and VIII.8.2 exemplify the room temperature $\epsilon'-E$ curves measured for films substituted with various amounts of Sm and Er. The experimental results depicted above show the asymmetrical behaviour with respect to both ϵ' and E axes. The data demonstrate the presence of built-in fields in the films investigated which are found to correlate with the type of dopant and doping level. Values of built-in field, E_b and contribution of domain walls, η , to the measured dielectric constant were obtained from the experimental $\epsilon'-E$ data and plotted in Fig. VIII.8.3 vs. doping level. The increase of the contribution of domain walls to the dielectric response found for Sm substituted films is in consistence with the concept of enhanced domain wall mobility in donor ions doped materials [6,8]. Contrary to Sm, Er doping did not produce a significant effect on η . The specific properties of Er doped films can be attributed to the role of secondary phases (such as pyrochlore) in domain wall pinning processes. In fact, particles of residual second phases can be considered as effective pinning centres for domain walls. The existence of such particles is demonstrated using XRD analysis which revealed an enhanced tendency to stabilize the pyrochlore phase for films doped with lanthanide of smaller ionic radii (Dy and Er).

We must note further, that the value of E_B correlates with the amount of lanthanide ions added. Asymmetry of capacitance-voltage characteristics was extensively discussed by Vorotilov *et al.* [103]. It was suggested that asymmetry of $C-V$ curve and presence of the built-in field originate from a disturbed layer near the bottom electrode-film interface. This layer is characterized by a high density of point defects which serve as effective trap centers for charge carriers, causing non-uniform distribution of net charge density through film thickness (presence of the disturbed layer was also inferred from thickness dependent capacitance of our specimens). Although the explanation of $C-V$ curves asymmetry is plausible, it does not explain the effects of doping on the value of built-in field. Internal bias field formation in bulk ferroelectrics have been investigated by many groups (see references [186-188]). Takahashi [186] discussed the effects of various (donor and acceptor) additives on the internal bias in lead zirconate ceramics. It was demonstrated that acceptor-type doping strengthens the internal bias while the opposite tendency was revealed for donor doped materials. It was suggested that acceptor impurity-oxygen vacancy defect dipoles are responsible for this phenomena. Arlt and Neumann [187] analysed quantitatively the interplaying between bias field and defect dipoles in Ni-doped (up to 1%) BaTiO_3 . Based on calculation of dipole energies they conclude that while in the paraelectric phase all three directions are equivalent, below the Curie point acceptor ion-oxygen vacancy dipoles are inclined to be oriented along the polarization direction. Warren *et al.* [188] investigated processes of defect-dipole alignment in various ceramic materials by means of electron paramagnetic resonance (EPR). In agreement with earlier work of Arlt and Neumann [187], it was shown that alignment of defect-dipole complexes is possible only in tetragonal lattices. Alignment was not observed in non-ferroelectric SrTiO_3 and in $\text{Pb}(\text{Zr,Ti})\text{O}_3$ and BaTiO_3 above their Curie temperatures.

The results of the present work show that with increasing Sm content the built-in field vanishes. Three possible mechanisms can be proposed to explain this result: i) as discussed by Arlt and Neumann [187] and Warren *et al.* [188], oxygen vacancies are involved in defect-dipole complexes, and, due to the fact that they are considered as the most mobile defects in perovskite lattices, are responsible for dipole reorientation processes. At the same time, donor doping is known to reduce the concentration of oxygen vacancies. Therefore, it is expected to observe the reduction of E_B in donor impurities modified ceramic materials. The results presented here are in agreement with this mechanism and with the data reported by Takahashi [186]; ii) it was also demonstrated that alignment of defect complexes occurs along the c -axis of the tetragonal lattice [187,188]. Due to the fact that doping with lanthanide ions leads to a

noticeable decrease in the tetragonal strain (Fig.VIII.1.3), it is straightforward to suppose that the reduction in the built-in field is a consequence of the decrease of the role of lattice tetragonality as a "driving force" for defect-dipole alignment processes.

As shown above, the ϵ' - E characteristics were significantly affected by the nature of bottom electrode. The LNO bottom electrode leads to lower values of dielectric constant (compared to films on Pt) and broadening of the peaks near the coercive field. This result indicate that in the case of the film deposited on LNO electrode, the polarization switching process is significantly hampered either by pinning centres which may arise from film-electrode reaction layers or from the drop in the electric field at the low permittivity interfacial layer (see above).

IX.8. Voltage-, temperature- and thickness-dependent leakage currents in pure and doped lead titanate thin films.

The J - E curves measured at various temperatures for PbTiO_3 thin film deposited on platinized silicon substrate are shown in Fig.VIII.9.1. The rectifying nature of Pt- PbTiO_3

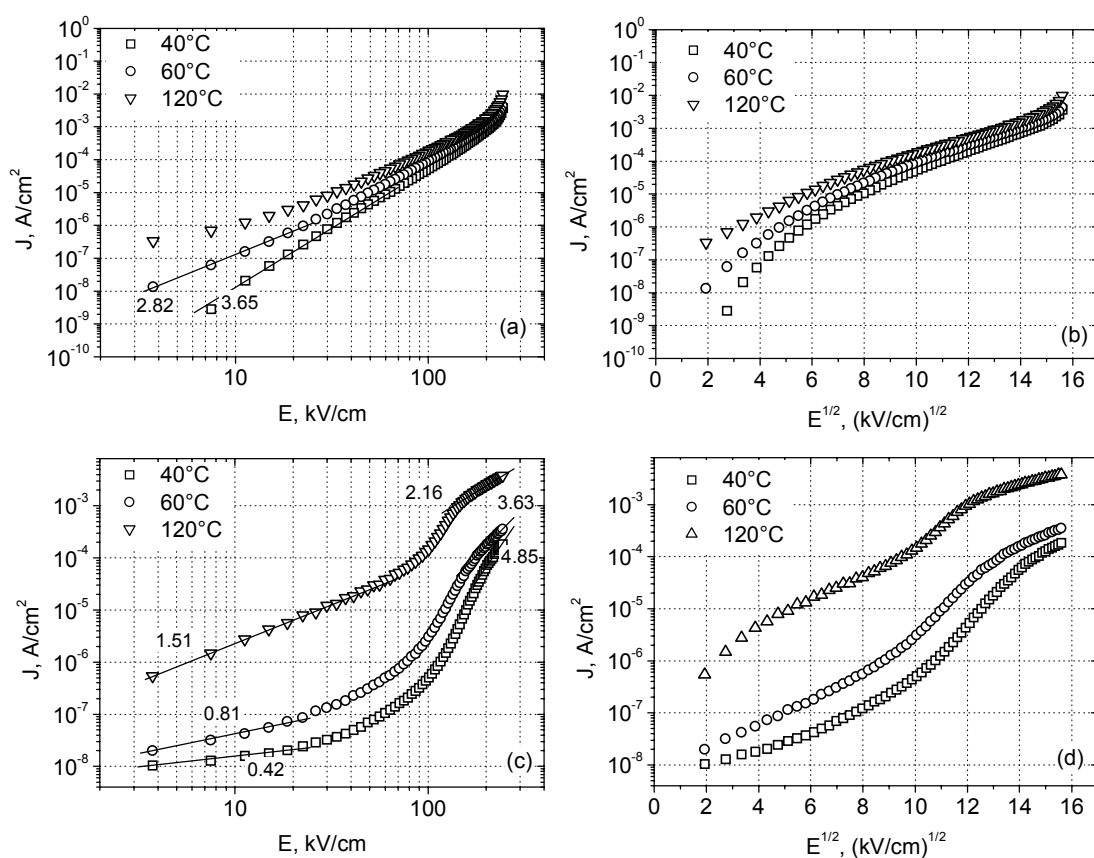


FIG.IX.8.1. Representation of leakage current data, obtained for non-doped lead titanate thin film (corresponding to Fig.VIII.9.1) in full logarithmic form (a – negative and c – positive parts) and vs. square root of applied bias field (b - negative and d – positive parts). Absolute values of field and current are taken.

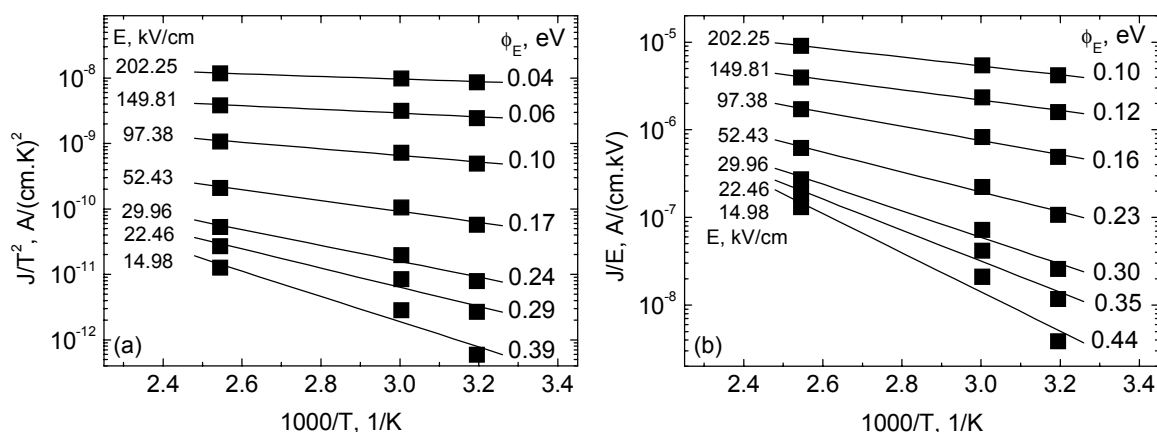


FIG.IX.8.2. Leakage current density in non-doped lead titanate thin film of thickness 267 nm (negative potential is applied to the bottom electrode) selected for different field and plotted in Schottky (a) and Poole-Frenkel (b) coordinates.

contact indicates the presence of Schottky-type barrier (see paragraph V.8 and ref 139). The weakening of rectifying ability of the contact at elevated temperature can be explained by barrier lowering (will be analyzed in the following).

Schottky type emission (interface limited) and SCLC (bulk limited) mechanisms (see paragraph V.8 and references therein) were claimed by many research groups as the operating conduction processes in ferroelectric thin films. Conclusions about the conduction mechanism prevailing under certain conditions (temperature and DC bias voltage) are usually done based on the analysis of the shape and the character of J - E dependences. In case of Schottky mechanism linear plots of $\log J$ vs. $E^{1/2}$ should be obtained (see equation (V.8.8)). The SCLC mechanism should lead to linear $\log J$ - $\log E$ plots (see equation (V.8.11)). Fig.IX.8.1 represents the leakage current data, obtained for non-doped lead titanate thin films (corresponding to Fig.VIII.9.1) as double logarithmic plots (a – negative and c – positive parts), and as $\log J$ vs. $E^{1/2}$ (b - negative and d – positive parts). It can be seen that the negative side of $\log J$ - $\log E$ plots (a) can be linearly fitted with decreased slope for data acquired at higher temperatures. With increasing temperature (see data for 120°C) deviation from linear behaviour is observed. The $\log J$ - $E^{1/2}$ plot (b) shows a linear behaviour at higher fields (higher than 50 kV/cm) and a more complex behaviour at lower values of the bias fields. An even more complex J - E dependence is revealed for the case when positive potential was applied to the bottom electrode (forward biased metal-dielectric contact, Fig's IX.8.1(c) and,(d)). $\log J$ - $\log E$ plots (c) can be divided in three regions. The low field part shows a linear dependence with increasing slope as the temperature increases. Such behaviour and the values

of slope (in the vicinity of unit) let us treat the metal-ferroelectric-metal contact as ohmic in the range of the field under consideration. Another linear region on $\log J$ - $\log E$ plots can be recognized at high field (higher than 150 kV/cm). This region is characterized by a slope which is found to decrease when the temperature increases. Similar observations on PZT thin film were attributed by Shin *et al.* [96] to the onset of the SCLC mechanism. Overlapping of several conducting mechanisms may be responsible for more complex $\log J$ - $\log E$ dependences in the intermediate field range. The positive part of the J - E curve plotted in $\log J$ - $E^{1/2}$ form (Fig. VIII.8.1(d)) reveals that the linear behaviour can be observed only in the high field region. Thus, it can be seen that in the case of non-doped PbTiO_3 thin film it is very difficult to state which mechanism is responsible for the conduction in the field and temperature ranges investigated.

Fig.IX.8.2 shows leakage current densities of non-doped lead titanate thin films selected for different fields and plotted in Schottky (a) and Poole-Frenkel (b) coordinates. Irrespective of the mechanism supposed, temperature and field activated processes are observed. It is important to note that the slopes of the plots decrease with increasing applied bias field indicating field induced barrier lowering. The barrier height, measured at fixed applied bias and found from $\log J/T^2$ - $1/T$ or $\log J/E$ - $1/T$ plots is designated ϕ_E (eV). It is obvious from equations (V.8.8) and (V.8.9) that $\phi_B = -q(\phi_B - \sqrt{qE/4\pi\epsilon_i})$ (Schottky) and $\phi_B = -q(\phi_B - \sqrt{qE/\pi\epsilon_i})$ (Poole-Frenkel) and that ϕ_E vs. $E^{1/2}$ plot must yield straight lines. Contrary to what is expected, ϕ_E shows rather complex behaviour for both Schottky and Poole-Frenkel models with respect to $E^{1/2}$, as illustrated in Fig.IX.8.3. It means that the data of leakage currents acquired for the non-doped lead titanate thin film arise from the superposition of many processes, and that conduction is controlled by different mechanisms operating simultaneously in the high field region.

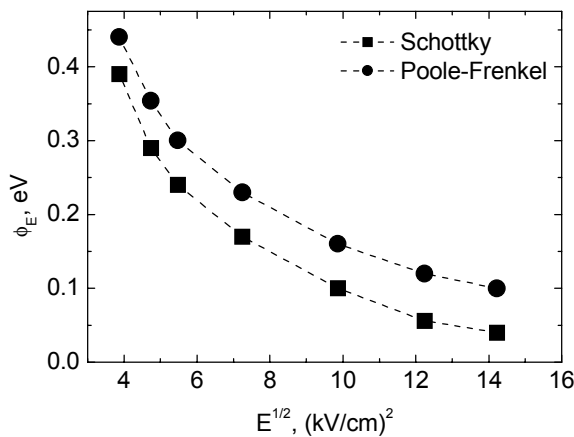


FIG.IX.8.3. Field-dependent barrier height for non-doped PbTiO_3 thin film.

Doping with either donor or acceptor elements can stabilize the defect structure of the thin films and compensate the influence of unintentional and uncontrollable impurities on the electrical properties of the ferroelectric capacitor [131]. The results of the present work show that, additionally to a noticeable decrease of leakage current density (Fig's VIII.9.2), doping with donor elements also affects the character of $\phi_E-E^{1/2}$ dependence. The most reliable results were obtained for Sm substituted films because Sm modifies phase content of the films to the least extent. The values of field-dependent barrier height calculated for film, substituted with 2 mol % of Sm are represented in Fig. IX.8.4. The data plotted in $\phi_E-E^{1/2}$ form can be well fitted with a straight lines and zero-field barrier height ϕ_B can be obtained from the intercept with the ordinate axis. Considering Schottky and Poole-Frenkel models, values of ϕ_B were determined as 1.52 eV and 1.61 eV, respectively. Barrier height $\phi_B=0.8$ eV (assuming Schottky model) was reported for sol-gel PZT films having Pt top and bottom electrodes by Stolichnov and Tagantsev [134]. The value was obtained at the field of 250 kV/cm and zero-field barrier height was not reported for those specimens. Extrapolation of our results (Fig. IX.8.4) to $E^{1/2}=15.81$ (kV/cm) $^{1/2}$ ($250^{1/2}=15.81$ (kV/cm) $^{1/2}$) gives the value of Schottky barrier of approximately 0.4 eV which is two time less than reported in [134]. Blom *et al.* [133] give the barrier height of 2 eV for Au-PbTiO₃ (PLD) contact. The value was deduced from metal-ferroelectric band structure consideration assuming ferroelectric to be of *p*-type. Taking into an account the fact, that Pt electrode has higher work function (5.7 eV) compared to that of Au (5.2 eV) [139, p.251], barrier height of Pt-PbTiO₃ structure might be even higher. It is obviously that ϕ_B is very sensitive to factors determining the quality of metal-ferroelectric interface such as deposition method, film composition and fabrication parameters.

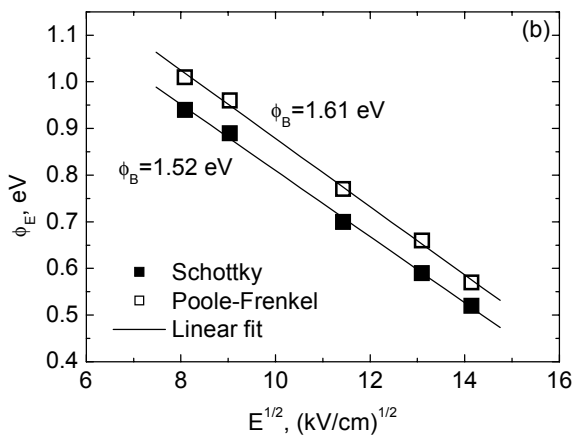


FIG. IX.8.4. Field-dependent barrier height for 2 mol % of Sm doped lead titanate thin films ($d=245$ nm).

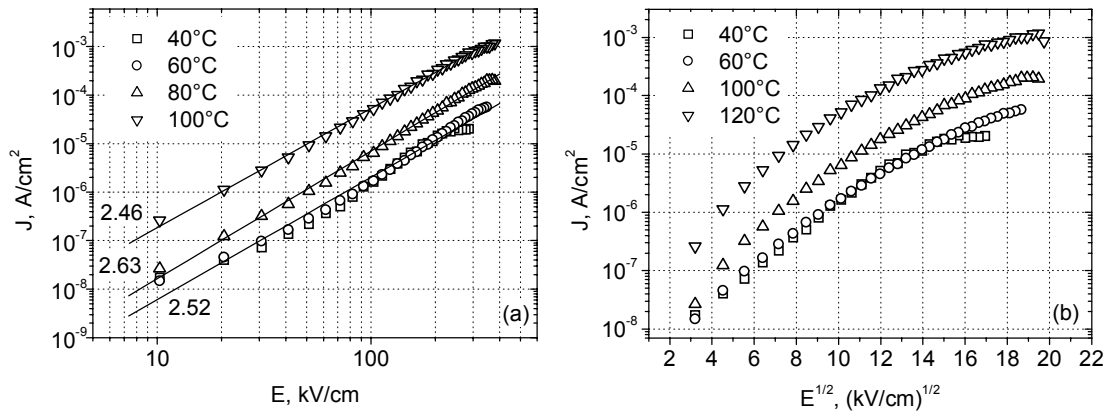


FIG.IX.8.5. Representation of leakage current data (negative part), obtained for PET5 thin film deposited on lanthanum nickel oxide bottom electrode (corresponding to Fig.VIII.9.3(a)) in full logarithmic form (a) and vs. square root of applied bias field (b). Absolute values of field and current are taken. Results of linear fit to the experimental data are represented by solid lines. Numbers indicate the slopes found for linear regions of the $\log J$ - $\log E$ and $\log J$ - $E^{1/2}$ characteristics.

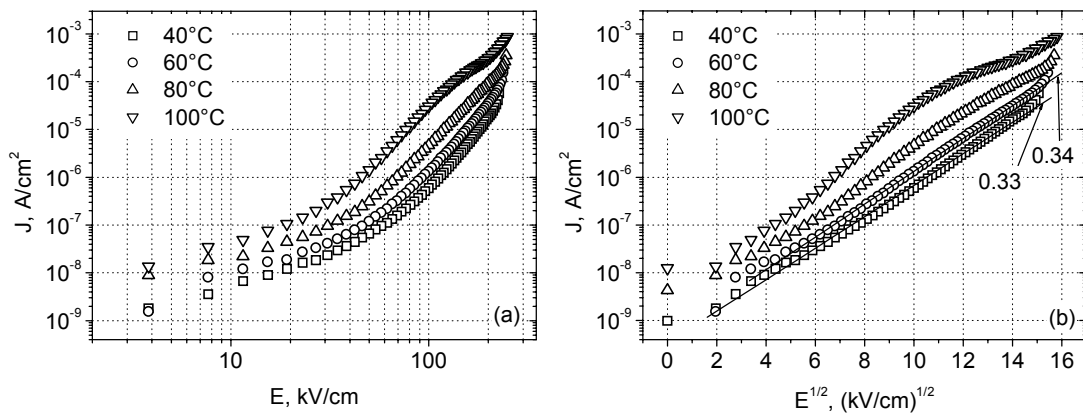


FIG.IX.8.6. Representation of leakage current data (negative part), obtained for PET5 thin film deposited on platinumized substrate (corresponding to Fig.VIII.9.3(b)) in full logarithmic form (a) and vs. square root of applied bias field (b). Absolute values of field and current are taken. Results of linear fit to the experimental data are represented by solid lines. Numbers indicate the slopes found for linear regions of the $\log J$ - $\log E$ and $\log J$ - $E^{1/2}$ characteristics.

The negative parts of the J - E characteristics obtained at various temperatures for the film fabricated on LNO and Pt bottom electrodes (corresponding to Fig's VIII.9.3(a) and (b)) are illustrated in Fig's IX.8.5 and IX.8.6, respectively, in full logarithmic (a) and $\log J$ - $E^{1/2}$ (b) forms. Data obtained for PET5/LNO/Pt structure (Fig VIII.9.3.(a)) and presented in the log-log plot (Fig.IX.8.5(a)) can be well fitted with straight lines in the range of temperature and DC bias field investigated with nearly constant slope, while a more complex dependence of

$\log J$ vs. $E^{1/2}$ is found (Fig.IX.8.5(b)) for this structure. The data represented for PET5 films deposited on Pt electrode can be well fitted to Schottky model at lower temperature (Fig.IX.8.6(b)) (Schottky and Poole-Frenkel models yield zero-field barrier height 0.53 eV and 0.6 eV, respectively) and demonstrate a more complex behaviour at elevated temperatures. We suppose that in the films fabricated on LNO bottom electrodes, the conductivity processes are mainly operated by the SCLC mechanism in the ranges of temperatures and fields investigated, whereas interface-limited Schottky mechanism is responsible for conductivity in the films fabricated on platinized Si substrates at lower temperature (in agreement with earlier papers, see references cited in paragraph V.8). At higher temperatures (100-120°C) the presence of both Schottky and SCLC mechanisms is supposed. Investigations of the leakage current density as a function of thickness of our samples (Fig.VIII.9.4) confirm this supposition. The dependence of leakage current density on film thickness was found to be more pronounced for specimens deposited on LNO electrode. For a set of specimens fabricated on Pt bottom electrode, the leakage current density was found to be practically thickness independent at lower temperature (slope m is less than unit).

X. Choice of application: doped PbTiO_3 thin films for pyroelectric and piezoelectric detectors

A. Results of pyroelectric and piezoelectric measurements.

The pyroelectric and piezoelectric properties were determined exemplarily for PbTiO_3 films substituted with 5 mol % of Sm and Er. The thin films consisted of 12 layers (see paragraph VII.1 for the details on specimen preparation). For the pyroelectric coefficient determination, the specimen temperature was sinusoidally varied in the frequency range from 0.03 to 0.2 Hz using a thermoelectric element (Peltier element) operated with a function generator. The temperature of the specimen was controlled via the measurements of the top electrode resistance (bolometric effect). Two diagonal contacts of the electrode structure illustrated in Fig. VII.1.7 were used. The electrode was calibrated prior to the experiment using commercial thermal sensor placed on the sample surface. Fig.X.1 exemplifies temperature dependence of Pt top electrode resistance. Peak values of the resistance and temperature were used to obtain calibration coefficient. The pyroelectric current measured with a digital lock-in amplifier was used to calculate the pyroelectric coefficient of the specimens (see paragraph VII.2 for more details). The values of the pyroelectric coefficients are found to be $63 \mu\text{C}/\text{m}^2\text{K}$ and $122 \mu\text{C}/\text{m}^2\text{K}$ for as-prepared (unpoled) PST5 and PET5 thin films, respectively.

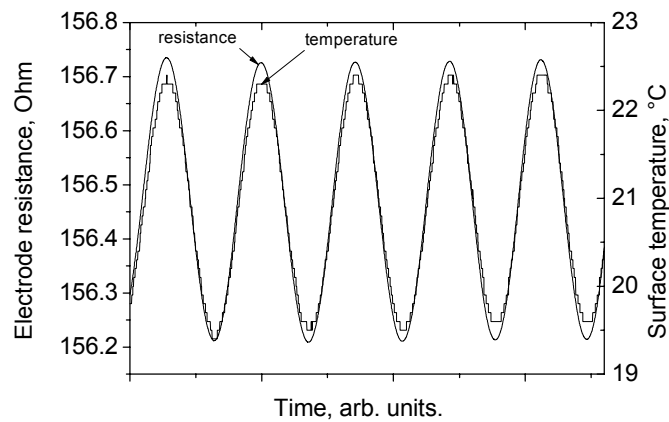


FIG.X.1. Data used for Pt top electrode calibration: dependence of electrode resistance on the temperature of the specimen surface.

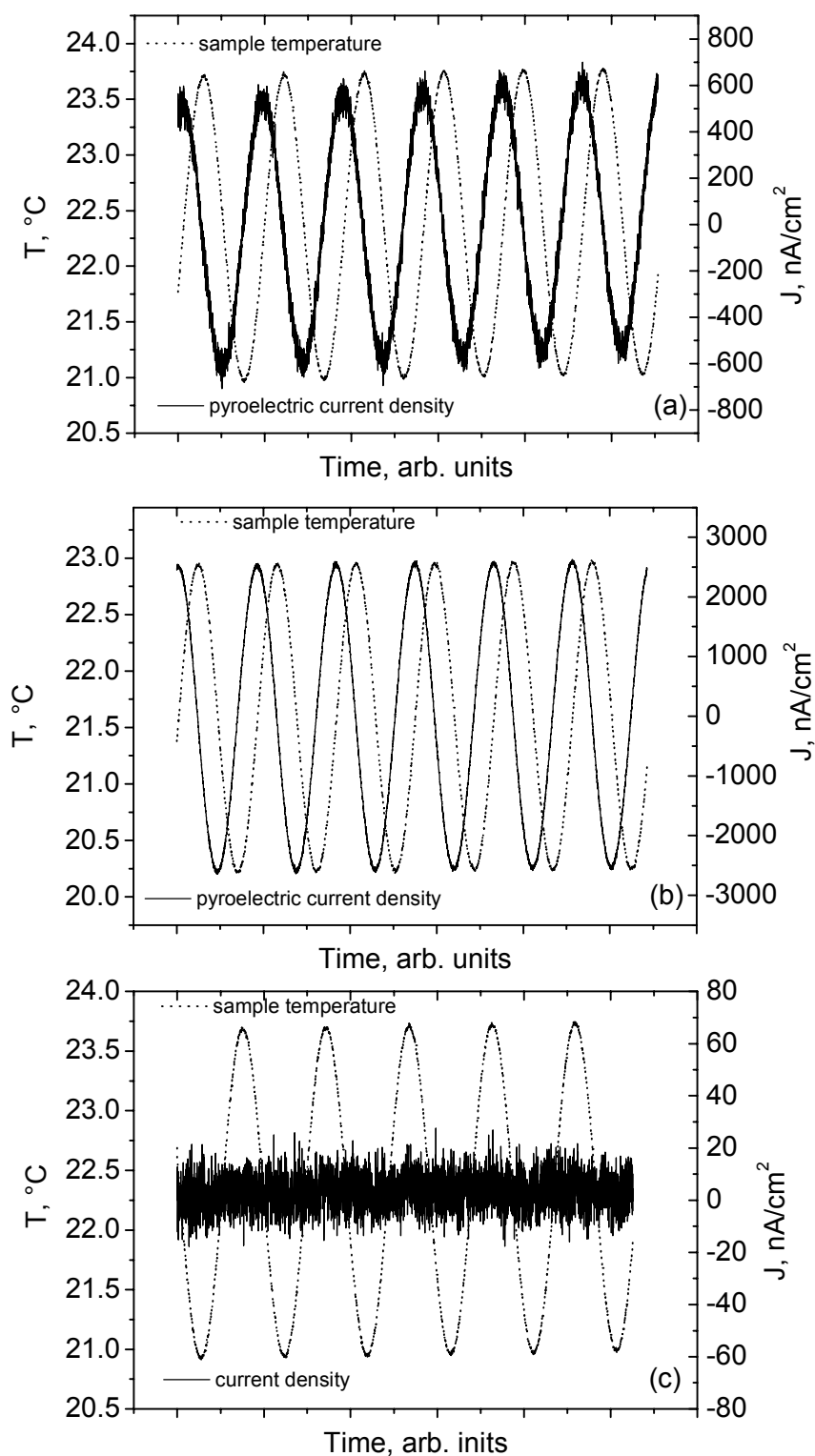


FIG.X.2. Surface temperature variation and pyrodynamic response (pyroelectric current density) measured for unpoled PST5 (a) and PET5 (b) thin films. Background level is also presented for comparison (c). Thermal cycling was done at a frequency of 0.01 Hz using the Peltier element.

Detectivity figure of merit, F_D , was calculated for PET5 and PST5 samples as 7.82 and 3.04 [$\times 10^{-6}$, $(\text{m}^3\text{J}^{-1})^{1/2}$], respectively, using (III.3.17). Volume specific heat of PZT, $c' = 2.5 \cdot 10^6 \text{ J/m}^3\text{K}$ [45] was taken.

In order to demonstrate the applicability of the films in real pyroelectric detectors, thermal cycling (Peltier element, frequency 0.01 Hz) was applied to the specimens and pyroelectric current was monitored. The experimental data are presented in Fig.X.2 (a) and (b) for PST5 and PET5 films, respectively. The level of background is also shown for comparison (c). Maximum pyroelectric current density of approximately $2.500 \mu\text{A/cm}^2$ was obtained for Er modified specimen. Significantly lower pyroelectric response (about 600 nA/cm^2) was found for Sm substituted film.

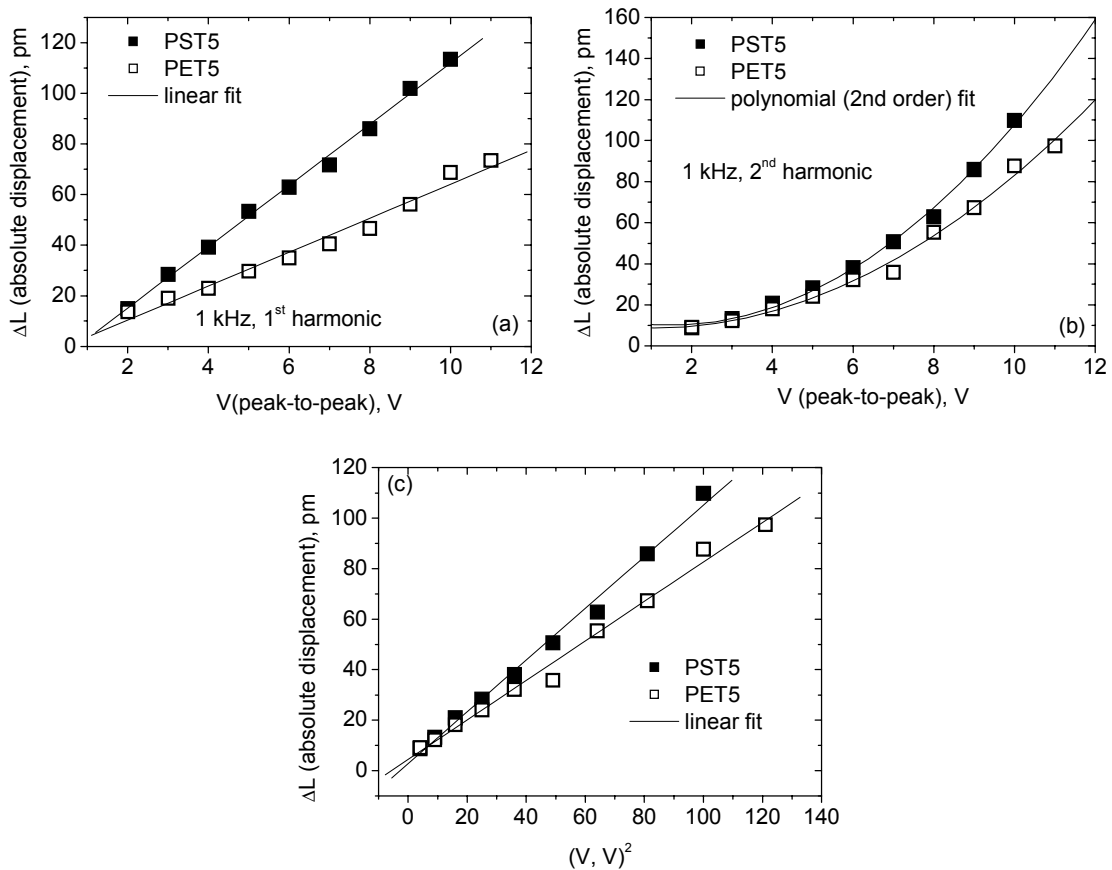


FIG.X.3. Displacement amplitude (1st (a) and 2nd (b) harmonics) measured for PST5 and PET5 thin films at 1 kHz and various voltage amplitudes; 2nd harmonic is also shown vs. squared voltage amplitude (c). Results of linear or polynomial fit are represented by lines.

For the piezoelectric (interferometric) measurements, the laser beam was collimated onto the central electrode of the structure (Fig.VII.1.7). One of the additional electrodes was used to apply the AC bias from the function generator. The interferometrically measured

piezoelectric response from the films investigated is presented in Fig.X.3 as function of applied AC voltage amplitude (absolute value of sample surface displacement is shown). A linear dependences of the displacement amplitude found for both specimens allows the field independent effective piezoelectric coefficients, d_{eff} , to be obtained in the range of the fields investigated (Fig.X.3(a), 1st harmonic). Fig's X.3 (b) and (c) show 2nd harmonic generated due to electrostriction effect. ΔL plotted vs. squared voltage amplitude (Fig.X.3(c)) can be well fitted to the straight line and electrostriction coefficients of the specimens to be found. The results of the pyroelectric and piezoelectric characterization of selected specimens are summarized in Table X.1. Room temperature dielectric properties (dielectric constant and loss tangent) are also given.

Table X.1. Pyroelectric and piezoelectric properties of 5 mol % of Sm and Er substituted PbTiO_3 thin films.

	PST5	PET5
p , $\mu\text{C}/\text{m}^2\text{K}$	63	122
d_{eff} , pm/V	48.4	26.8
$m_{\text{eff}} \times 10^{-6}$, $(\text{cm}/\text{kV})^2$	4.308	3.292
ϵ' (1 kHz)	310	220
$\tan\delta$ (1 kHz)	0.025	0.02
$F_D \times 10^{-6}$, $(\text{m}^3\text{J}^{-1})^{1/2}$	3.04	7.82

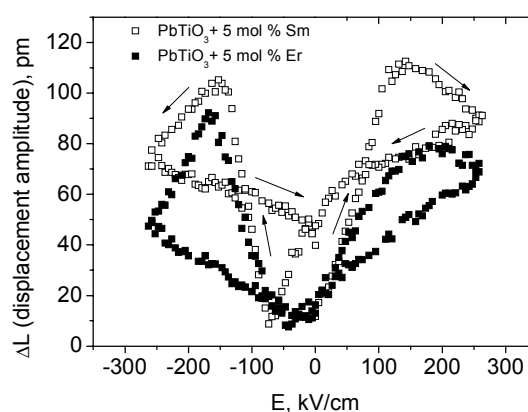


FIG.X.4. DC bias field-dependent piezoelectric response from Sm and Er substituted thin films.

Additionally, DC field-dependent piezoelectric response from the films was investigated. For this purpose, DC voltage was applied across the capacitor of interest and oscillation of the sample surface was excited by the application of an AC signal from the function generator. Frequency and amplitude of the AC voltage were 1 kHz and $1V_{\text{p-p}}$,

respectively. The DC bias amplitude was 25 V that corresponds to a field of approximately 260 kV/cm. The piezoelectric hysteresis loops obtained for PST5 and PET5 films are shown in Fig.X.4. DC bias sweep starts at zero voltage. The directions of voltage change are indicated by arrows in the figure. It can be seen that (similarly to ϵ' - E data, paragraph VIII.8) maximum displacements are reached at DC biases corresponding to the coercive fields of the films due to ferroelectric switching.

B. Discussions.

We must note first that unlike bulk ceramics, the pyroelectric and piezoelectric responses were measured for the as-deposited (unpoled) specimens. The fact that despite unpoling pyroelectric and piezoelectric responses were detected can be explained in terms of self-polarization of the films, probably due to the stress developed during crystallization and cooling through the Curie temperature. Self-polarized states of the films could be very useful from the point of view of the potential applications in different integrated devices (IR imaging devices, MEMS) where poling is difficult to achieve. Moreover, the self-polarized state in our films is very stable, and poling did not produce a noticeable effect on the pyroelectric and piezoelectric responses. It is known that in the PbZrO_3 - PbTiO_3 system of solid solutions, the effect of poling is maximum for compositions close to the MPB (corresponds to PZT (52/48)) whereas in Ti-rich compounds (especially in PbTiO_3) it is marginal. In this respect, the results presented here agree with early published data ([44] and Table III.3.1).

The nature of the doping element affects the value of the pyroelectric coefficient. Doping with 5 mol % of Er increases substantially the pyroelectric coefficient (compared to 5 mol % of Sm substituted film). The explanation to this result can be given in terms of the effect of doping on the preferred orientation of the crystallites. As already discussed, the films doped with Er are characterized by a pronounced (100) out-of-plane fibre texture (see paragraph VIII.1) whereas for Sm doped films [100] axis of the fibre texture was found to form an angle of approximately 54° with the normal to the sample plane (Fig's VIII.1.4 and VIII.1.5). Obviously, higher pyroelectric coefficients are expected for films containing larger amount of domains/grains aligned with their polar axis perpendicular to the plane of the specimen. The (100)-out-of-plane preferentially oriented Er doped films are abundant in the grains which can be polarized in the perpendicular (to the specimen plane) direction. Roughly (neglecting the effect of ionic radius on the lattice tetragonality and hence on the value of the spontaneous polarization), $p(\text{PST5})$ shall be equal to $p(\text{PET5})\cos 54^\circ$. The experimental results obtained (Table X.1) are in general agreement with this assumption. These results

unambiguously show the decisive influence of preferred orientations on the pyroelectric response of unpoled sol-gel fabricated PbTiO_3 thin films. Furthermore, it is known that the maximum of the pyroelectric coefficient of ferroelectric materials lies in the vicinity of their Curie point, and the reduction of the Curie temperature therefore can cause some increase in the pyroelectric coefficient. The temperature dependent dielectric properties of lanthanide doped PbTiO_3 thin films investigated above (see paragraph VIII.5) show that films substituted with Er undergo ferroelectric-to-paraelectric phase transition at temperatures somewhat lower than those of Sm substituted films. Therefore the results of pyroelectric characterization of our films can also be explained in terms of the lanthanide doping on the Curie temperature of the films.

The values of p measured for both specimens (Table X.1) are substantially lower than those found for poled pyroelectric ceramics ($p=380 \mu\text{C}/\text{m}^2\text{K}$, modified PZT ceramics [45] and PT based thin films ($p=250\text{-}1500 \mu\text{C}/\text{m}^2\text{K}$ [44, Wersing and Bruchhaus, p.186]) deposited on single crystalline MgO, LNO and sapphire substrates, but exceed those known for polymer pyroelectric materials ($p=27 \mu\text{C}/\text{m}^2\text{K}$, PVDF) [45]. However, it must be noted that in the case of ferroelectric thin films, method of deposition, material of substrate and even technique utilized for pyroelectric coefficient determination could play a decisive role and must be taken into an account.

The results of piezoelectric characterization of PbTiO_3 films modified with 5 mol % of Sm and Er (Fig. X.3 and Table X.1) contradict the observations of Lefki and Dormans [189] who reported the absence of piezoelectric activity for as-deposited (unpoled) sol-gel PZT films. At the same time, the effective piezoelectric coefficients obtained for PST5 and PET5 thin films were by a factor of two higher than those reported by these authors for unpoled OMCVD PZT films [189]. Piezoelectric coefficients of *lead titanate thin films* were not found in the literature. The data are lacking probably due to difficulties in preparation and piezoelectric properties characterization (due to high risk of cracking and conductivity of lead titanate films) and high conductivity of undoped films. The first harmonic of the displacement amplitude was found to be linear with respect to the amplitude of applied AC signal for both specimens and piezoelectric coefficient d_{eff} is constant in the entire range of driving fields investigated (from 0 to 11 $V_{\text{p-p}}$ or from 0 to approximately 58 kV/cm field amplitude). Apparently, the range of linearity of piezoelectric properties of our specimens is larger compared to PZT thin films and ceramics of various compositions [190,191]. It is known that both 180°- and 90°-domain walls contribute to the dielectric properties of tetragonal thin films (extrinsic response) while only 90° domains are responsible for piezoelectric activity of the

films and ceramics [145,192] (neighbour 180°-domains displace in the antiparallel directions compensating each other; in the case of 90°-domains this compensation does not occur). The non-linear piezoelectric activity is attributed to domain contribution while the "linear portion" of the field-dependent piezoelectric properties corresponds to the lattice contribution (intrinsic contribution). The results of piezoelectric measurements (Fig.X.3(a)) suggest rather monodomain state of the grains and/or preponderance of 180°-domains. It is useful to consider the results of piezoelectric characterization together with those of ϵ' - E measurements. In particular, Fig.VIII.8.3 compares the contribution of domains, η , to the measured dielectric constant obtained for Sm and Er substituted films. One can see that doping with Sm resulted in an increase of domain wall mobility or concentration while the effect of Er can be neglected. Thereby, the increase of domain wall mobility and/or concentration in Sm substituted films is confirmed only by means of dielectric characterization. Therefore it is straightforward to suppose that doping with Sm rather creates 180°-domains while crystallites of Er substituted film remain in monodomain state. Furthermore, we can see that doping with Sm results in a higher value of linear (field-independent) d_{eff} compared to that of Er doped films. Increase of measured value of piezoelectric coefficient (Table X.1) can be attributed to higher lattice (intrinsic) contribution to the apparent piezoelectric response of Sm substituted film (in comparison to Er substituted specimen).

In conclusion, as demonstrated for dielectric and pyroelectric properties, the piezoelectric coefficient of PbTiO₃ thin films can also be influenced, viz. tailored, by varying the ionic radius/atomic number of doping lanthanides.

IX. Summary and conclusions

Structural, electrophysical and functional properties of lead titanate thin films substituted with elements of the lanthanide series were systematically investigated and discussed in this thesis. The sol-gel method was adopted for specimen preparation. Ce, Sm, Dy, Er and Yb were chosen as doping elements. The experimental conditions were optimized so as to allow deposition of crack-free thin films with homogeneous morphology. Various characterization methods were used to investigate correlation between ionic radius, concentration of doping ions and properties of the films. The structural properties (texture and phase composition) of the specimens were investigated by means of X-ray diffractometry and Raman spectroscopy. Low and high frequency (optical) dielectric, ferroelectric and leakage properties were characterized as a function of temperature. Additionally, the effects of the bottom electrode material and film thickness were investigated for a set of selected specimens. In order to investigate the applicability of lanthanide ions substituted films in IR and piezoelectric sensors, pyroelectric and effective piezoelectric coefficients of some selected samples were measured and compared with those reported for thin films and ceramics by other research groups. The results are discussed in terms of doping effects, the combined effects of stress development, influence of the grain size and film thickness. Based on the results of the present work the following conclusions can be drawn:

- The optimized processing conditions lead to the crystallization of the tetragonal perovskite phase. Very fine polycrystalline (grain size was found to be in the range of 100-140 nm) homogeneous microstructures of the films were obtained. Residual pyrochlore (paraelectric) was found to form thin (presumably of approximately 10 nm thickness) layer in the near surface region. The amount this phase increased with decreasing ionic radius of doping ion (case of Dy and Er).
- Θ - 2Θ and grazing incidence XRD characterization of the films revealed the decrease of lattice tetragonality for all doping elements investigated.

- Pole figure and fibre texture plot analysis of the films deposited on (111) textured Pt bottom electrode showed (100) out-of-plane texture for pure and Dy and Er substituted films. Ce, Sm and Yb substituted films were found to be characterized by (100)+(111) preferred orientation with no in-plane alignment.
- Raman spectroscopy confirmed the tetragonal perovskite structure of the thin films. The softening of the $E(1TO)$ soft mode was found for pure and doped films. The results were attributed to grain size effects and stress development for the undoped film. Doping with rare-earth ions caused further decrease of the soft phonon frequency indicating the decrease of the ferroelectric order in the films. These results agree also with the observed decrease of Curie transition temperature and lattice tetragonality of pure and doped films.
- The effects of lanthanide ions substitution on the low and high (optical) frequency dielectric properties of lead titanate thin films were systematically investigated. It is shown that the index of refraction and the small signal dielectric properties (dielectric constant and loss tangent) correlate not only with doping level, but are also with the atomic number/ionic radius of dopant. With the exception of Ce, the indices of refraction of the films are shown to decrease with decreasing ionic radius of doping ion. The results are explained in terms of substitution of lead with ions of smaller polarizability. The specific behaviour of Ce is attributed to the 4+ oxidation state revealed by means of XPS analysis. The Curie phase transition temperature of pure lead titanate thin films was found to be lower than that of bulk ceramics and, on the other hand, was found to correlate with the atomic number and concentration of dopant, viz. T_C decreases with increasing atomic number of doping element. T_C was also found to decrease with increasing doping level for all elements investigated. Comparison of the results of electrical characterization reported in the present work with those published by other research groups for thin films and ceramics of various compositions enable us to suppose A-site substitution (donor-type) for all Ln elements investigated.
- Ferroelectric and field-dependent dielectric properties of doped specimens were investigated with respect to bottom electrode material and type of doping ions. Doping of lead titanate thin films fabricated on Pt electrode with Sm, Ce, Dy and Er was found to improve the shape of the ferroelectric hysteresis loop due to compensation of conductivity. The use of lanthanum nickel oxide

(LNO) as a bottom electrode material caused poor ferroelectric properties. Analysis of ϵ' - E characteristics obtained for lanthanide elements doped films revealed increased contribution of domain walls and their mobility in Sm substituted films. Much smaller effect was found for Er-doped films.

- Analysis of the results of leakage current properties characterizations shows that conduction in the films fabricated on LNO bottom electrodes is mainly operated by the space charge limited current (SCLC) mechanism in the ranges of temperature and field investigated. Interface-limited Schottky mechanism is found to be responsible for conductivity at lower temperature in the films fabricated on platinized Si substrates. At higher temperatures (100-120°C) the presence of both Schottky and SCLC mechanisms is supposed.
- 5 mol % of Sm and Er doped thin films demonstrated pyroelectric and piezoelectric activity in the as-deposited (unpoled) state due to self-polarization. The pyroelectric and piezoelectric properties of the films are found to be sensitive to the ionic radius/atomic number of lanthanide ions. Sm substituted films are characterized by better piezoelectric and poor pyroelectric properties, while the reverse was found for Er substituted films.

List of references.

- [1] J. Valasek, Phys. Rev. **15**, 537 (1920).
- [2] W. Känzig, Ferroelectrics, **74**, 285 (1987).
- [3] G. Busch, Ferroelectrics, **71**, 43 (1987).
- [4] J. Fousek, Ferroelectrics, **113**, 3 (1991).
- [5] G. Busch, Ferroelectrics, **74**, 267 (1987).
- [6] G.H. Haertling, J. Am. Ceram. Soc. **82**, 797 (1999).
- [7] C. Kittel, *Introduction to Solid State Physics* (John Wiley and Sons, New York, 1996) pp.393-394.
- [8] Y. Xu, *Ferroelectric Materials and Their Applications* (North-Holland, Amsterdam, 1991) p.3.
- [9] A.F. Wells, *Structural Inorganic Chemistry* (Clarendon Press, Oxford, 1995), pp. 584-588.
- [10] S. Iakovlev, unpublished.
- [11] A.F. Devonshire, Adv. Phys. **3**, 85 (1954).
- [12] C. Brennan, Integr. Ferroelectr. **8**, 335 (1995).
- [13] R. Blinc, B. Žekš, *Soft Modes in Ferroelectrics and Antiferroelectrics* (North-Holland, Amsterdam, 1974) pp. 36-45.
- [14] A. von Hippel *et al.*, N.D.R.C. Rep. No. 300, August 1944, cited in Tech. Rep. 51 (1950) Massachusetts Institute of Technology.
- [15] J.F. Scott, *Ferroelectric Memories* (Springer, Berlin, 2000) pp.79-94.
- [16] *Ferroelectric Thin Films: Synthesis and Basic Properties*, ed. C.P. de Araujo, J.F. Scott, G.W. Taylor (Gordon and Breach, Amsterdam, 1996).
- [17] R.L. Sandstrom, W.J. Gallagher, T.R. Dinger, R.H. Koch, R.B. Laibowitz, A.W. Kleinsasser, R.G. Gambino, B. Bumble, M.F. Chisholm, Appl. Phys. Lett. **53**, 444 (1988).
- [18] R.B. Laibowitz, R.H. Koch, P. Chaudari, R.J. Gambino, Phys. Rev. B, **35**, 8821 (1987).

- [19] D. Dijkkamp, T. Venkatesan, X.D. Wu, S.A. Shaheen, N. Jisrawi, Y.H. Min-Lee, W.L. McLean, M. Croft, *Appl. Phys. Lett.* **51**, 619 (1987).
- [20] J. Narayan, N. Buinno, R. Singh, O.W. Holland, O. Auciello, *Appl. Phys. Lett.* **51**, 1845 (1988).
- [21] J.S. Horwitz, K.S. Grabowski, D.B. Chrisey, R.E. Leuchtner, *Appl. Phys. Lett.* **59**, 1565 (1991).
- [22] C.M. Cotell, K.S. Grabowski, *MRS Bull.* **17**, 44 (1992).
- [23] H.M. Manasevit, W.I. Simpson, *J. Electrochem. Soc.* **116**, 1725 (1969).
- [24] *Sol-gel Technology for Thin Films, Fibers, Preforms, Electronics, and Specialty Shapes*, ed. L.C. Klein (Noyes Publications, Park Ridge, New Jersey, U.S.A., 1988).
- [25] K.D Budd, S.K. Dey, D.A. Payne, *Brit. Ceram. Proc.* **36**, 107 (1985).
- [26] B.A. Tuttle, R.W. Schwartz, *MRS Bullet.* **21**, 49 (1996).
- [27] Z. Kighelman, D. Damjanovic, A. Seifert, S. Gentil, S. Hiboux, N. Setter, *Mater. Res. Soc. Symp. Proc.* **596**, 523 (2000).
- [28] J.-G. Cheng, J. Tang, X.-J. Meng, S.-L. Guo, J.-H. Chu, M. Wang, H. Wang, Z. Wang, *J. Amer. Ceram. Soc.* **84**, 1421 (2001).
- [29] V. Joshi, D. Roy, M.L. Mecarthey, *Appl. Phys. Lett.* **63**, 1331 (1993).
- [30] A. Montenero, M. Canali, H. Gnappi, D. Bersani, P.P. Lottici, P. Nunziante, E. Traversa, *Appl. Organometal. Chem.* **11**, 137 (1997).
- [31] A. Li, C. Ge, P. Lü, D. Wu, S. Xiong, N. Ming, *Appl. Phys. Lett.* **70**, 1616 (1997).
- [32] P.F. Baude, C. Ye, D.L. Polla, *Mater. Res. Soc. Symp. Proc.* **310**, 139 (1993).
- [33] D.L. Segal, *J. Non-Crystalline Solids*, **63**, 183-191 (1984).
- [34] A.C. Pierre, *Introduction to Sol-Gel Processing* (Kluwer Academic Publishers, Boston, 1998) p. 4.
- [35] C.J. Brinker, *Sol-Gel Science: the Physics and Chemistry of Sol-Gel Processing* (Academic Press, London, 1990) p. 29.
- [36] R.W. Schwartz, R.A. Assink, D. Dimos, M.B. Sinclair, T.J. Boyle, C.D. Buchheit, *Mater. Res. Soc. Symp. Proc.* **361**, 377 (1995).
- [37] G. Yi, M. Sayer, *J. Sol-Gel Sci. Technol.* **6**, 65 (1996).
- [38] Y.T. Kwon, I.-M. Lee, W.I. Lee, C.J. Kim, I.K. Yoo, *Mater. Res. Bull.* **34**, 749 (1999).
- [39] M. Sayer, C.V.R. Vasant Kumar, D. Barrow, L. Zou, D.T. Amm, *Mater. Res. Soc. Symp. Proc.* **243**, 39 (1992).

- [40] M. Daglish, T. Kemmitt, IPENZ Trans. **27**, 21 (2000).
- [41] L.J. Schwee, S. Spring, US Patent 5 038 323 (1991).
- [42] R. Ramesh, S. Aggarwal, O. Auciello, Mater. Sci. Eng. **32**, 191 (2001).
- [43] D.L. Polla, L.F. Francis, MRS Bull. **21**, 59 (1996).
- [44] W. Wersing, R. Bruchhaus: *Handbook of Thin Film Devices*, ed. M.H. Francombe (Academic Press, New York, 2000) Vol. 5; S.B. Lang, D.K. Das-Gupta, in *Handbook of Advanced Electronic and Photonic Devices*, ed. H.S. Nalwa (Academic Press, San Diego, 2001), pp.18-19.
- [45] A.J. Moulson, J.M. Herbert, *Electroceramics* (Chapman and Hall, London, 1990) pp.318-337.
- [46] R. Jenkins, R.L. Snyder, *Introduction to X-ray Powder Diffractometry* (John Wiley and Sons, New York, 1996).
- [47] R.P. Goehner, M.O. Eatough, Powder Diffraction, **7**, 2 (1992).
- [48] K. Aoki, Y. Fukuda, K. Numata, A. Nishimura, Jpn. J. Appl. Phys., Part I, **33**, 5155 (1994).
- [49] Q.F. Zhou, E. Hong, R. Wolf, S. Trolrier-McKinstry, Mater. Res. Soc. Symp. Proc. **655**, CC11.7.1 (2001).
- [50] V. Bornard, S. Trolrier-McKinstry, K. Takemura, C.A. Randall, J. Appl. Phys. **87**, 3965 (2000).
- [51] R. Ramesh, T. Sands, V.G. Keramidas, Appl. Phys. Lett. **63**, 731 (1993).
- [52] U.F. Kocks, C.N. Tomé, H.R. Wenk, *Texture and Anisotropy* (Cambridge University Press, 1998).
- [53] V. Randle, O. Engler, *Introduction to Texture Analysis* (Gordon and Breach Science Publishers, 2000).
- [54] H.-J. Bunge, *Texture Analysis in Materials Science* (Cuvillier Verlag, Göttingen, 1993).
- [55] C.V. Raman, K.S. Krishnan, Nature, **121**, 501 (1928).
- [56] H. Ibach, H. Lüth, *Solid-State Physics*, 2nd edition (Springer, Berlin, 1996).
- [57] A.B. Christie in *Methods of Surface Analysis*, ed. J.M. Walls (Cambridge University Press, 1989) pp. 127-168.
- [58] S. Iakovlev, C.-H. Solterbeck, A. Piorra, V. Zaporojtchenko, M. Es-Souni, J. Mater. Sci.: Mater. Electr. **14**, 143 (2003).
- [59] K. Wetzig in *In situ Scanning Electron Microscopy in Materials Research*, ed. K. Wetzig, D. Schulze (Academie Verlag, Berlin, 1995) p.19.

- [60] H. Schönherr, PhD Theses, University of Twente (1999).
- [61] Multi Mode Scanning Probe Microscope, Digital Instruments, Instruction manual (1997).
- [62] H.G. Tompkins, *A User's Guide to Ellipsometry* (Academic Press, Boston, 1993) p.10.
- [63] H. Diamant, K. Drenck, R. Pepinsky, *Rev. Sci. Instrum.* **28**, 30 (1957).
- [64] Radiant Technologies, Inc., RT6000S Operating Manual.
- [65] M. Schumacher, G.W. Dietz, R. Waser. *Integr. Ferroelectr.* **10**, 231 (1995); G.W. Dietz, R. Waser, *ibid.* **9**, 317 (1995).
- [66] S.B. Lang, *Sourcebook of Pyroelectricity* (Gordon and Breach Science Publishers, London, 1974) p.32.
- [67] L. Lian, N.R. Sottos, *J. Appl. Phys.* **87**, 3941 (2000).
- [68] M.D. Glinchuk, E.A. Eliseev, A. Deineka, L. Jastrabik, G. Suchaneck, T. Sandner, G. Gerlach, M. Hrabovsky, *Integr. Ferroelectr.* **38**, 101 (2001).
- [69] A. Deineka, M.D. Glinchuk, L. Jastrabik, G. Suchaneck, T. Sandner, G. Gerlach, *Ferroelectrics*, **254**, 205 (2001).
- [70] V.E. Wood, J.R. Busch, S.D. Ramamurthi, S.L. Swartz, *J. Appl. Phys.* **71**, 4557 (1992).
- [71] *MRS Bull.* **24**(9), 1999.
- [72] J.-F. Chang, S.B. Desu, *J. Mater. Res.* **9**, 955 (1994).
- [73] J. Lee, A. Safari, R.L. Pfeffer, *Appl. Phys. Lett.* **61**, 1643 (1992).
- [74] W. Braun, B.S. Kwak, A. Erbil, D.J. Dubai, B.J. Wilkens, *Appl. Phys. Lett.* **63**, 467 (1993).
- [75] M.B. Kelman, L.F. Schloss, P.C. McIntyre, B.C. Hendrix, S.M. Bilodeau, J.F. Roeder, *Appl. Phys. Lett.* **80**, 1258 (2002).
- [76] S. Iakovlev, M. Avdeev, C.-H. Solterbeck, M. Es-Souni, *Phys. Stat. Sol.(a)* **198**, 121 (2003).
- [77] S. Iakovlev, C.-H. Solterbeck, A. Piorra, M. Es-Souni, *Thin Solid Films*, **414**, 216 (2002).
- [78] M. Es-Souni, A. Piorra, C.-H. Solterbeck, S. Iakovlev, M. Abed, *J. Electroceram.* **9** 125 (2002).
- [79] B. Lewis, J.C. Anderson, *Nucleation and Growth of Thin Films* (Academic Press, New York, 1978).

- [80] M. Es-Souni, A. Piorra, C.-H. Solterbeck, M. Abed, *Mater. Sci. Eng.* **B86**, 237 (2001).
- [81] G. Burns, B.A. Scott, *Phys. Rev. Lett.* **25**, 167 (1970).
- [82] G. Burns, B.A. Scott, *Phys. Rev.* **B7**, 3088 (1973).
- [83] K. Ishikawa, K. Yoshikawa, N. Okada, *Phys. Rev.* **B37**, 5852 (1988).
- [84] I. Taguchi, A. Pignolet, L. Wang, M. Proctor, F. Lévy, P.E. Schmid, *J. Appl. Phys.* **73**, 394 (1993).
- [85] I. Taguchi, A. Pignolet, L. Wang, M. Proctor, F. Lévy, P.E. Schmid, *J. Appl. Phys.* **74**, 6625 (1993).
- [86] E. Ching-Prado, A. Reynés-Figueroa, R.S. Katiyar, S.B. Majumder, D.C. Agrawal, *J. Appl. Phys.* **78**, 1920.
- [87] W.L. Zhong, B. Jiang, P.L. Zhang, J.M. Ma, H.M. Cheng, Z.H. Yang, L.X. Li, *J. Phys.: Condens. Matter.* **5**, 2619 (1993).
- [88] J. Meng, G. Zou, J. Li, Q. Cui, X. Wang, Z. Wang, M. Zhao, *Sol. State Commun.* **90**, 643 (1994).
- [89] S. Iakovlev, C.-H. Solterbeck, M. Es-Souni, *J. Electroceram.* **10**, 103 (2003).
- [90] P.S. Dobal, S. Bhaskar, S.B. Majumder, R.S. Katiyar, *J. Appl. Phys.* **86**, 828 (1999).
- [91] S.-H. Paek, J. Won, K.-S. Lee, J.-S. Choi, C.-H. Park, *Jpn. J. Appl. Phys.* **35**, 5757 (1996).
- [92] C.S. Hwang, B.T. Lee, C.S. Kang, K.H. Lee, H.-J. Cho, H. Hideki, W.D. Kim, S.I. Lee, M.Y. Lee, *J. Appl. Phys.* **85**, 287 (1999).
- [93] K. Amanuma, T. Mori, T. Hase, T. Sakuma, A. Ochi, Y. Miyasaka, *Jpn. J. Appl. Phys.* **32**, 4150 (1993).
- [94] Y. Sakashita, H. Segawa, K. Tominaga, M. Okada, *J. Appl. Phys.* **73**, 7857 (1993).
- [95] M. Es-Souni, N. Zhang, S. Iakovlev, C.-H. Solterbeck, A. Piorra, *Thin Solid Films*, **440**, 26 (2003).
- [96] J.C. Shin, C.S. Hwang, H.J. Kim, S.O. Park, *Appl. Phys. Lett.* **75**, 3411 (1999).
- [97] G.A.C.M. Spierings, G.J.M. Dormans, W.G.J. Moors, M.J.E. Ulenaers, P.K. Larsen, *J. Appl. Phys.* **78**, 1926 (1995).
- [98] S.S. Sengupta, S.M. Park, D.A. Payne, L.H. Allen, *J. Appl. Phys.* **83**, 2291 (1998).
- [99] S.-O. Chung, J.W. Kim, G.H. Kim, C.O. Park, W.J. Lee, *Jpn. J. Appl. Phys.* **36**, 4386 (1997).
- [100] M. Sayer, A. Mansingh, A.K. Arora, A. Lo, *Integr. Ferroelectr.* **1**, 129 (1992).

- [101] C.J. Brennan, *Integr. Ferroelectr.* **2**, 73 (1992).
- [102] F.K. Chai, J.R. Brews, R.D Schrimpf, D.P. Birnie III, *J. Appl. Phys.* **82**, 2505 (1997).
- [103] K.A. Vorotilov, M.I. Yanovskaya, O.A. Dorokhova, *Integr. Ferroelectr.* **3**, 33 (1993).
- [104] M. Algueró, M.L. Calzada, L. Pardo, E. Snoeck, *J. Mater. Res.* **14**, 4570 (1999).
- [105] B.H. Mah, N.W. Jang, J.H. Park, D.S. Paik, C.Y. Park, *Mater. Res. Bull.* **35**, 1113 (2000).
- [106] M. Es-Souni, M. Abed, A. Piorra, S. Malinowski, V. Zaporojtchenko, *Thin Solid Films*, **389**, 99 (2001).
- [107] R. Kurchania, S.J. Milne, *J. Mater. Sci.* **33**, 659 (1998).
- [108] P.S. Dobal, R.R. Das, B. Roy, R.S. Katiyar, S. Jain, D.C. Agrawal, *Mater. Res. Soc. Symp. Proc.* **596**, 357 (2000).
- [109] T. Matsuzaki, H. Funakubo, *J. Appl. Phys.* **86**, 4559 (1999).
- [110] G. Teowee, E.L. Quackenbush, C.D. Baertlein, J. M. Boulton, E.A. Kneer, D.R. Uhlmann, *Mater. Res. Soc, Symp. Proc.* **361**, 433 (1995).
- [111] Q. Zou, H.E. Ruda, B.G. Yacobi, *Appl. Phys. Lett.* **78**, 1282 (2001).
- [112] M.-S. Chen, T.-B. Wu, J.-M. Wu, *Appl. Phys. Lett.* **68**, 1430 (1996).
- [113] C.H. Lin, B.M. Yen, H.C. Kuo, H. Chen, T.B. Wu, G.E. Stillman, *J. Mater. Res.* **15**, 115 (2000).
- [114] Z. Zhang, J.H. Park, S. Trolier-McKinstry, *Mater. Res. Soc. Symp. Proc.* **596**, 73 (2000).
- [115] T.M. Shaw, Z. Suo, M. Huang, E. Liniger, R.B. Laibowitz, J.D. Baniecki, *Appl. Phys. Lett.* **75**, 2129 (1999).
- [116] S. Chattopadhyay, A.R. Teren, J.-H. Hwang, T.O. Mason, B.W. Wessels, *J. Mater. Res.* **17**, 669 (2002).
- [117] G.A. Samara, *Phys. Rev.* **151**, 378 (1966).
- [118] D.E. Dausch, G.H. Haertling, *J. Mater. Sci.* **31**, 3409 (1996).
- [119] G.A. Rossetti, Jr., L.E. Cross, K. Kushida, *Appl. Phys. Lett.* **59**, 2524 (1991).
- [120] K. Okazaki, K. Nagata, *J. Am. Ceram. Soc.* **56**, 82 (1973).
- [121] S. Chattopadhyay, P. Ayyub, V.R. Palkar, M. Multani, *Phys. Rev.* **B52**, 13177 (1995).
- [122] Q. Tan, Z. Xu, D. Viehland, *Phil. Mag.* **80**, 1585 (2000).

- [123] H.D. Sharma, A. Govindan, T.C. Goel, P.K.C. Pillai, C. Pramila, *J. Mater. Sci. Lett.* **15**, 1424 (1996).
- [124] T.J. Boyle, P.G. Clem, B.A. Tuttle, G.L. Brennecka, J.T. Dawley, M.A. Rodriguez, T.D. Dunbar, W.F. Hammetter, *J. Mater. Res.* **17**, 871 (2002).
- [125] H.-B. Park, C.Y. Park, Y.-S. Hong, K. Kim, S.-J. Kim, *J. Am. Ceram. Soc.* **82**, 94 (1999).
- [126] P. Gonnard, M. Troccaz, *J. Sol. State Chem.* **23**, 321 (1978).
- [127] S.R. Shannigrahi, R.N.P. Choudhary, H.N. Acharya, *Mater. Res. Bull.* **34**, 1875 (1999).
- [128] C. Pramila, T.C. Goel, P.K.C. Pillai, *J. Mater. Sci. Lett.* **12**, 1657 (1993).
- [129] S.B. Majumder, Y.N. Mohapatra, D.C. Agrawal, *Appl. Phys. Lett.* **70**, 138 (1997).
- [130] B. Nagaraj, T. Sawhney, S. Perusse, S. Aggarwal, V.S. Kaushik, S. Zafar, R.E. Jones, J.-H. Lee, V. Balu, J. Lee, *Appl. Phys. Lett.* **74**, 3194 (1999).
- [131] G.W. Dietz, W. Antpöhler, M. Klee, R. Waser, *J. Appl. Phys.* **78**, 6113 (1995).
- [132] B.H. Park, S.J. Hyun, C.R. Moon, B.-D. Choe, J. Lee, C.Y. Kim, W. Jo, T.W. Noh, *J. Appl. Phys.* **84**, 4428 (1998).
- [133] P.W.M. Blom, R.M. Wolf, J.F.M. Cillessen, M.P.C.M. Krijn, *Phys. Rev. Lett.* **73**, 2107 (1994).
- [134] I. Stolichnov, A. Tagantsev, *J. Appl. Phys.* **84**, 3216 (1998).
- [135] S.M. Cho, D.Y. Jeon, *Thin Solid Films*, **338**, 149 (1999).
- [136] I. Stolichnov, A. Tagantsev, N. Setter, J.S. Cross, M. Tsukada, *Appl. Phys. Lett.* **75**, 1790 (1999).
- [137] H. N. Al-Shareef, D. Dimos, *J. Am. Ceram. Soc.* **80**, 3127 (1997).
- [138] W.S. Kim, S.-M. Ha, H.-H. Park, C.E. Kim, *Thin Solid Films*, **355**, 531 (1999).
- [139] S.M. Sze, *Physics of Semiconductor Devices* (John Wiley and Sons, New York, 1981) pp. 402-405.
- [140] K.K. Deb, K.W. Bennett, P.S. Brody, *Integr. Ferroelectr.* **6**, 253 (1995).
- [141] A. Pignolet, L. Wang, P.E. Schmid, J. Pavel, F. Lévi, *Ferroelectrics*, **128**, 37 (1992).
- [142] Y.-K. Tseng, K.-S. Liu, J.-D. Jiang, I.-N. Lin, *Appl. Phys. Lett.* **72**, 3285 (1998)
- [143] T. Kamada, R. Takayama, A. Tomozawa, S. Fujii, K. Iijuma, T. Hirao, *Mater. Res. Soc. Symp. Proc.* **433**, 377 (1996).
- [144] A.L. Kholkin, K.G. Brooks, D.V. Taylor, S. Hiboux, N. Setter, *Integr. Ferroelectr.* **22**, 525 (1998).

- [145] S. Trolier-McKinstry, J.F. Shepard, Jr., J.L. Lacey, T. Su, G. Zavala, J. Fendler, *Ferroelectrics*, **206-207**, 381 (1998).
- [146] S. Aggarwal, S. Madhukar, B. Nagaraj, I.G. Jenkins, R. Ramesh, L. Boyer, J.T. Evans, Jr., *Appl. Phys. Lett.* **75**, 716 (1999).
- [147] K.-H. Solterbeck, M. Es-Souni, unpublished.
- [148] MathCAD 2001i Professional, Mathsoft Engineering and Education, Inc.
- [149] A.M. Glazer S.A. Mabud, *Acta Crystallogr. Sec. B*, **34**, 1035 (1978).
- [150] K. Bammou, D. Khatib, F. Bensamka, *Moroccan J. Condens. Matter.* **2(1)**, (1999).
- [151] G.P. Kostikova, Yu.P. Kostikov, *Chemical Processes at Doping of Oxides*, St. Petersburg University, 1997 (*in Russian*).
- [152] C.K. Kwok, S.B. Desu, *Appl. Phys. Lett.* **60**, 1430 (1992).
- [153] S. Seraphin, S. Zhou, G. Teowee, J.M. Boulton, D.R. Uhlmann, *Mater. Res. Soc. Symp. Proc.* **310**, 369 (1993).
- [154] R.D. Klissurska, K.D. Brooks, I.M. Reaney, C. Pawlaczyk, M. Kosec, N. Setter, *J. Am. Ceram. Soc.* **78**, 1513 (1995).
- [155] M.L. Calzada, J. Ricote, R. Jiménez, J. Mendiola, submitted to *Thin Solid Films*.
- [156] J.A. Voigt, B.A. Tuttle, T.J. Headley, D.L. Lamppa, *Mater. Res. Soc. Symp. Proc.* **361**, 395 (1995).
- [157] M.A. Subramanian, G. Aravamudan, G.V. Subba Rao, *Prog. Solid St. Chem.* **15**, 55 (1983).
- [158] E. Vasco, O. Böhme, E. Román. C. Zaldo, *Appl. Phys. Lett.* **78**, 2037 (2001).
- [159] V.P. Afanas'ev, G.N. Mosina, A.A. Petrov, I.P. Pronin, L.M. Sorokin, E.A. Tarakanov, *Tech. Phys. Lett.* **27**, 467 (2001).
- [160] X. Li, J. Liu, Y. Zeng, J. Liang, *Appl. Phys. Lett.* **63** (1993) 2345.
- [161] A.L. Kholkin, S. Iakovlev, E. Fortunato, R. Martins, I. Ferreira, V. Shvartsman, J.L. Baptista, *Key Eng. Mater.* **230-232**, 563 (2002).
- [162] B.G. Demczyk, A.G. Khachatryan, G. Thomas, *Scripta Metallurgica*, **21**, 967 (1987).
- [163] C.E. Zybilla, H. Boubekour, P. Radojkovic, M. Schwartzkopff, E. Hartmann, F. Koch, G. Groos, B. Rezek, B. Bruchhaus, W. Wersing, *Mat. Res. Soc. Symp. Proc.* **541**, 449 (1999).
- [164] J.S. Speck, W. Pompe, *J. Appl. Phys.* **76**, 466 (1994).
- [165] S.B. Ren, C.J. Lu, H.M. Shen, Y.N. Wang, *Phys. Rev. B*, **55**, 3485 (1997).
- [166] K.S. Lee, S. Baik, *J. Appl. Phys.* **87**, 8035 (2000).

- [167] W.K. Choi, S.K. Choi, H.M. Lee, *J. Mater. Res.* **14**, 4677 (1999).
- [168] L.D. Madsen, E.M. Griswold, L. Wever, *J. Mater. Res.* **12**, 2612 (1997).
- [169] S. Pamir Alpay, A.L. Roytburd, *J. Appl. Phys.* **83**, 4714 (1998).
- [170] M. Yamada, N. Iizawa, T. Yamaguchi, W. Sakamoto, K. Kikuta, T. Yogo, T. Hayashi, S. Hirano, *Jpn. J. Appl. Phys. Part 1*, **42**, 5222 (2003).
- [171] S.-Y. Chen, I-W. Chen, *J. Am. Ceram. Soc.* **81**, 97 (1998).
- [172] Z. Huang, Q. Zhang, R.W. Whatmore, *J. Appl. Phys.* **86**, 1662 (1999).
- [173] M. Es-Souni, A. Piorra, *Mater. Res. Bull.* **36**, 2563 (2001).
- [174] K.G. Brooks, R.D. Klissurska, P. Moeckli, N. Setter, *J. Mater. Res.* **12**, 531 (1997).
- [175] R. Sirera, M.L. Calzada, *Mater. Res. Bull.* **30**, 11 (1995).
- [176] E.C.S. Tavares, P.S. Pizani, J.A. Eiras, *Appl. Phys. Lett.* **72**, 897 (1998).
- [177] R.D. Shannon, *Acta Crystallogh.* **A32**, 751 (1976).
- [178] H. Ibach, H. Lüth, *Solid-State Physics* (Springer, Berlin, 1995) p.79.
- [179] L.L. Hench, J.K. West, *Principles of Electronic Ceramics* (John Wiley and Sons, New York, 1990) p. 346.
- [180] D. Xue, K. Betzler, H. Hesse, *J. Phys.: Condens. Matter.* **12**, 3113 (2000).
- [181] B.V. Crist, *Handbook of Monochromatic XPS Spectra: The Elements and Native Oxides* (John Wiley and Sons, New York, 2000) p. 58.
- [182] D.V. Taylor, D. Damjanovic, *J. Appl. Phys.* **82**, 1973 (1997).
- [183] S. Iakovlev, C.-H. Solterbeck, M. Es-Souni, *Appl. Phys. Lett.* **81**, 1854 (2002).
- [184] G. King, E.G. Goo, *J. Am. Ceram. Soc.* **73**, 1534 (1990).
- [185] G. Shirane, S. Hoshino, *J. Phys. Soc. Jpn.* **6**, 265 (1951).
- [186] S. Takahashi, *Ferroelectrics*, **41**, 143 (1982).
- [187] G. Arlt, H. Neumann, *Ferroelectrics*, **87**, 109 (1988).
- [188] W.L. Warren, G.E. Pike, K. Vanheusden, D. Dimos, B.A. Tuttle, J. Robertson, *J. Appl. Phys.* **79**, 9250 (1996).
- [189] K. Lefki, G.J.M. Dormans, *J. Appl. Phys.* **76**, 1764 (1994).
- [190] A. Kholkin, *Ferroelectrics*, **238**, 235 (2000).
- [191] V. Mueller, Q.M. Zhang, *Appl. Phys. Lett.* **72**, 2692 (1998).
- [192] V. Mueller, Q.M. Zhang, *J. Appl. Phys.* **83**, 3754 (1998).

Appendix

- A. List of symbols
- B. Physical constants
- C. Radii of Pb^{2+} , Ti^{4+} , Zr^{4+} , O^{2-} and lanthanide ions
- D. Important quasi-chemical reactions in PZT
- E. Definition of domain types in films
- F. List of abbreviations

A. List of symbols.

Parameters		Units
A	work	J
A^*	effective Richardson coefficient	$\text{A}/(\text{T}\cdot\text{cm})^2$
a	lattice parameter	Å
c	lattice parameter	Å
c'	volume specific heat	$\text{MJ}/(\text{m}^3\cdot\text{K})$
$C; C_m$	measured value of capacitance	F
C_C	Curie constant	$^\circ\text{C}$; K
C_f	capacitance of a film	F
C_i	interfacial capacitance	F
C_b	bulk capacitance	F
C_0	capacitance of empty cell	F
C_T	capacitance of a pyroelectric detector circuit	F
$D; \mathbf{D}$	dielectric displacement	C/m^2
	grain size	nm
d	film thickness	nm
	piezoelectric coefficient	m/V ; C/N
d_{eff}	effective piezoelectric coefficient	m/V ; C/N

e	root mean square error	-
$E; \mathbf{E}$	electric field	V/m
E_b	binding energy	eV
E_B	built-in field	kV/cm
E_c	coercive field	kV/cm
E_k	kinetic energy	eV
E_p, E_s	parallel and perpendicular components of electric field	V/m
f	frequency	Hz
F	free energy	J
F_d	detectivity figure of merit	$(\text{m}^3/\text{J})^{1/2}$
F_I	current figure of merit	$\mu\text{C}\cdot\text{m}/\text{J}$
F_v	voltage figure of merit	m^2/C
G	image force	N
	thermal conductance	W/K
H	thermal capacity	J/K
I, i	current	A
I	intensity of the light	W/m^2
I_0	intensity of the light on the surface of the medium	W/m^2
I_p	pyroelectric current	A
I_r	intensity of a reference beam	W/m^2
I_s	sample beam	W/m^2
j	imaginary operator	-
J	current density	A/cm^2
k	imaginary part of refractive index (extinction coefficient)	-
l	distance of ions separation in crystal lattice	Å
L	displacement of the film surface	pm
m	electrostrictive coefficient	m^2/V^2
	thickness exponent	-
n	crystallization rate exponent	-
	real part of refractive index	-
	voltage exponent	-
$n_0; n_e$	0° and 90° components of the refractive index	-
N^*	complex refractive index	-
N_i	number of species (atoms or ions)	-

$\mathbf{p}; p$	pyroelectric coefficient	$C/(m^2K)$
$\mathbf{p}_g; p_g$	generalized pyroelectric coefficient	$C/(m^2K)$
$P; \mathbf{P}$	polarization	C/m^2
P_r	remnant polarization	C/m^2
P_s	spontaneous polarization	C/m^2
Q	electrostrictive coefficient	m^5/C^2
\mathbf{q}	wave vector	rad/m
r	Fresnel reflection coefficient	-
R_A, R_B, R_O	ionic radii of the ions in A-, B- and O-sites of the perovskite lattice	Å
R_{el}	electrode resistance	ohm
R_f	film resistance	ohm
R_i	ionic refraction	cm^3
R_I	current responsivity of a pyroelectric detector	Am^3/W
R_C	leakage resistance of a specimen	ohm
R_M	input resistance of an amplifier	ohm
$R^P; R^S$	perpendicular and parallel components of total reflection coefficient	-
R_T	resistance of a pyroelectric detector circuit	ohm
R_V	voltage responsivity of a pyroelectric detector	Vm^3/W
s	material compliance	m^2/N
S	area of plane capacitor	cm^2
	strain	-
t	tolerance (Goldschmidt) factor	-
	time	s
T	Temperature	$^{\circ}C ; K$
	Stress	Pa
T_C	Curie temperature	$^{\circ}C ; K$
v	velocity of the light in medium	m/s
	surface velocity	m/s
V	voltage	V
V_p	pyroelectric voltage	V
W	power density	W/m^3

x	molar ratio of components/composition	$\frac{\text{mol \%}}{100}$
	crystallized fraction	-
z	length	m
	ionic oxidation state;	-
	<i>Greek symbols</i>	
α	absorption coefficient	-
	ionic polarizability	\AA^3
	Landau coefficient	$\text{V}\cdot\text{m}/\text{C}$
β	Landau coefficient	$\text{V}\cdot\text{m}^5/\text{C}^3$
	phase film thickness	-
χ	dielectric susceptibility	F/m
ϵ	dielectric permittivity	F/m
ϵ^*	complex dielectric constant or complex relative permittivity	-
ϵ'	real part of dielectric constant	-
ϵ''	imaginary part of dielectric constant	-
ϵ_R	reversible Rayleigh parameters	-
ϵ_{IR}	irreversible Rayleigh parameters	cm/kV
ϕ_B	Schottky barrier height	eV
ϕ_m	metal work function	eV
φ	angle	$^\circ$, rad
Θ	Curie-Weiss temperature	$^\circ\text{C}$; K
	Diffraction angle	$^\circ$
η	emissivity	-
γ	Landau coefficient	$\text{V}\cdot\text{m}^9/\text{C}^5$
	Lorentz factor	-
γ^T	twinning shear	-
ω	angular frequency	Hz
λ	vacuum wavelength of the light	nm
μ_e	mobility of electrons	$\text{cm}^2/(\text{V}\cdot\text{s})$
μ_p	mobility of holes	$\text{cm}^2/(\text{V}\cdot\text{s})$
$\tan\delta$	loss tangent	-

ρ	charge density	1/cm
	complex ratio of total reflection coefficients	-
σ_i	i-component of elastic stress	Pa
τ_E	electric time constant of pyroelectric detector	s
τ_T	thermal time constant of pyroelectric detector	s
ζ_1	phase difference between the parallel and perpendicular components of the incoming waves	°, rad
ζ_2	phase difference between the parallel and perpendicular components of the outgoing waves	°, rad

B. Physical constants.

		value	units
c	velocity of the light in vacuum	$2.998 \cdot 10^8$	m/s
ϵ_0	dielectric permittivity of vacuum	$8.854 \cdot 10^{-12}$	F/m
q	charge of electron	$1.6 \cdot 10^{-19}$	C
k_B	boltsman constant	$1.38066 \cdot 10^{-23}$	J/K
h	Plank constant	$6.62617 \cdot 10^{-34}$	Js
\hbar	Reduced Plank constant	$1.05458 \cdot 10^{-34}$	Js

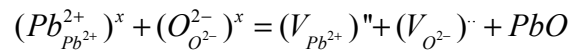
C. Radii of Pb^{2+} , Ti^{4+} , Zr^{4+} , O^{2-} and lanthanide ions [125, 177]

Ion	Ionic radius, Å	
	6-CN	12-CN
Pb^{2+}		1.49
Ti^{4+}	0.61	
Zr^{4+}	0.72	
O^{2-}	1.40	
La^{3+}	1.032	1.36
Ce^{4+}	0.87	1.14
Ce^{3+}	1.01	1.34
Sm^{3+}	0.958	1.24
Dy^{3+}	0.912	1.187*
Er^{3+}	0.89	1.159*
Yb^{3+}	0.868	1.13*

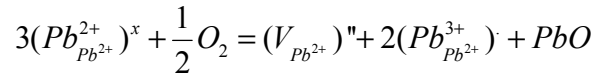
* These 12-coordinated ionic radii were calculated by multiplying the known 6-coordinate radii by the average $R_{Ln(12-CN)}/R_{Ln(6-CN)}$ ratio for La^{3+} , Nd^{3+} and Sm^{3+} ions, both $R_{Ln(12-CN)}$ and $R_{Ln(6-CN)}$ of which were known [125]

D. Important quasi-chemical reactions in PZT

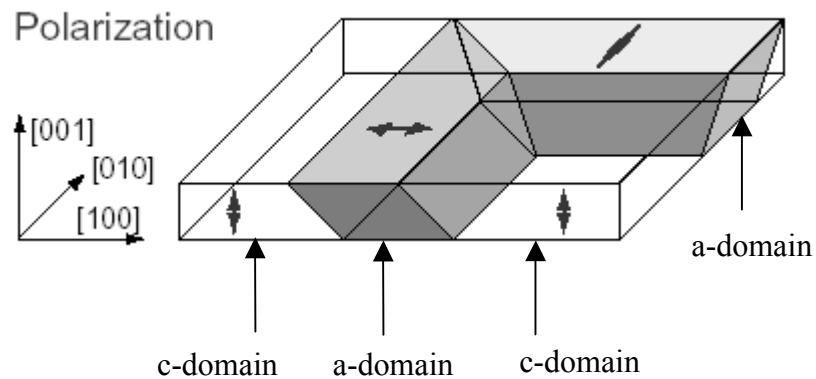
Creation of vacancies in PZT lattice due to lead volatility [146]:



Pb^{2+} ions can be oxidized to Pb^{3+} resulting in lead vacancy creation [146]:



E. Definition of domain types in films.



F. List of abbreviations.

AC	alternating current
AES	Auger electron spectroscopy
AOM	acousto-optic modulator
BSE	back-scattered electrons
BTO	bismuth titanium oxide
CN	coordination number
CTE	coefficient of thermal expansion
CVD	chemical vapour deposition
DC	direct current
DRAM	dynamic random access memory
DSC	differential scanning calorimetry

DUT	device under test
EDS	energy dispersion spectroscopy
ESCA	electron spectroscopy for chemical analysis
FE	ferroelectric
FM	frequency modulation
FT	fiber texture
FTP	fiber texture plot
GI	grazing incidence
HRTEM	high resolution transmission electron microscopy
HTSC	high temperature superconductor
IC	integrated circuit
IR	infrared
LIMM	laser intensity modulation method
Ln	element of lanthanide series
LSCO	lanthanum strontium cobalt oxide
MEMS	microelectromechanical system
MIBRSD	multi-ion-beam reactive sputter deposition
MOD	metalorganic decomposition
MFM	metal-ferroelectric-metal structure
MPB	morphotropic phase boundary
NVRAM	non-volatile random access memory
OMCVD	organometallic chemical vapour deposition
PLD	pulsed laser deposition
PLZT	lead lanthanum zirconate titanate
PFN	lead iron niobate
PMN	lead magnesium niobate
PT	lead titanate
PTC	positive temperature coefficient
PVDF	polyvinylidene fluoride
PZ	lead zirconate
PZFNT	$\text{Pb}_{1.1}\text{Zr}_{0.58}\text{Fe}_{0.2}\text{Nb}_{0.2}\text{Ti}_{0.02}\text{O}_3$
PZN	lead zinc niobate
PZT	lead zirconate titanate
RE	rare-earth elements

RMS	root mean square
SEM	scanning electron microscopy
SCLC	space charge limited current
SIMS	secondary-ion mass spectroscopy
SRO	strontium ruthenium oxide
TEM	transmission electron microscopy
TGS	triglycine sulphate
VGS	virtual ground system
XPS	X-ray photoelectron spectroscopy
XRD	X-ray diffractometry

Curriculum Vitae

Personal

Name: Sergey Yakovlev

Date of birth: 12 Jan 1976

Place of birth: Podolsk, Moscow Region, Russia

Nationality: Russian

Education

2001- date: PhD student, University of Applied Sciences of Kiel, Institute for Materials and Surface Technology (IMST), Germany. In collaboration with the Department of Engineering, Christian-Albrechts University of Kiel, Germany.

1993-1999: Dipl. Eng. Moscow State Institute of Electronics and Mathematics, Technical University (Moscow, Russia). Thesis: "Silicon single crystal production technology by Czochralsky with fixed oxygen content"

List of publications

1. A.L. Kholkin, S.O. Iakovlev, J.L. Baptista, Direct effect of illumination on ferroelectric properties of lead zirconate titanate thin films, *Appl. Phys. Lett.* **79**, 2055 (2001).
2. A.L. Kholkin, S. Iakovlev, E. Fortunato, R. Martins, I. Ferreira, V. Shvartsman, J.L. Baptista, optical and photoelectric properties of PZT films for microelectronic applications, *Key Eng. Mater.* **230-232**, 563 (2002).
3. A.L. Kholkin, S.O. Iakovlev, J.L. Baptista, Polarization control and domain manipulation in ferroelectric films with UV light, *Integr. Ferroelectr.* **37**, 525 (2001).
4. S. Iakovlev, C.-H. Solterbeck, A. Piorra, M. Es-Souni, Processing and characterization of solution deposited $\text{Pb}_{1.1}(\text{Zr}_{0.58}\text{Fe}_{0.2}\text{Nb}_{0.2}\text{Ti}_{0.02})\text{O}_3$ thin films, *Thin Solid Films*, **414**, 216 (2002).
5. S. Iakovlev, C.-H. Solterbeck, M. Es-Souni, Doping and thickness effects on dielectric properties and subswitching behavior of lead titanate thin films, *Appl. Phys. Lett.* **81**, 1854 (2002).

6. M. Es-Souni, A. Piorra, C.-H. Solterbeck, S. Iakovlev, M. Abed, Microstructure and properties of solution deposited, Nb-doped PZT thin films, *J. Electroceram.* **9**, 125 (2002).
7. S. Iakovlev, C.-H. Solterbeck, A. Piorra, V. Zaporojtchenko, M. Es-Souni, Dielectric and pyroelectric properties of PZFNT/PZT bimorph thin films, *J. Mater. Sci.: Mater. Electr.* **14**, 143 (2003).
8. S. Iakovlev, M. Avdeev, C.-H. Solterbeck and M. Es-Souni, Erbium doping effects on solution deposited PbTiO₃ thin films, *Phys. Stat. Solidi (a)* **198**, 121 (2003).
9. M. Es-Souni, N. Zhang, S. Iakovlev, C.-H. Solterbeck, A. Piorra, Thickness and erbium doping effects on the electrical properties of lead zirconate titanate thin films, *Thin Solid Films*, **440**, 26 (2003).
10. S. Iakovlev, C.-H. Solterbeck, M. Es-Souni, Structural and dielectric characterization of sol-gel fabricated PbTiO₃ thin films doped with lanthanide ions, *J. Electroceram.* **10**, 103 (2003).
11. S. Iakovlev, C.-H. Solterbeck, A. Piorra, N. Zhang, M. Es-Souni, M. Avdeev, Sol-gel preparation and characterization of Er doped PbTiO₃ thin films, *Ferroelectrics*, **293**, 161 (2003).
12. S. Iakovlev, C.-H. Solterbeck, V. Zaporojtchenko, M. Es-Souni, Rare-earth ions doping effects on the optical properties of sol-gel fabricated PbTiO₃ thin films, *Thin Solid Films*, **446**, 50 (2004).
13. M. Es-Souni, S. Iakovlev, C.-H. Solterbeck, Multilayer ferroelectric thin films for pyroelectric applications, *Sens. Act. A.* **109**, 114 (2004).
14. M. Es-Souni, S. Iakovlev, C.-H. Solterbeck, Processing and characterization of PZFNT and PZFNT/PET thin films for pyroelectric applications, *J. Eur. Ceram. Sos.* **24**, 985 (2004).
15. M. Es-Souni, S. Iakovlev, V. Zaporojtchenko, New thin film heterostructures for pyroelectric applications, Proceedings of the Conferences: 6th International Conference for Optical Technologies, Optical Sensors and Measuring Techniques; 8th International Conference for Infrared Sensors and Systems, 25-27 May 2004, pp. 249-253.

